

REPORT DOCUMENTATION PAGE			Form Approved OMB No. 0704-0188		
Public reporting burden for this collection of information is estimated to average 1 hour per response, including the time for reviewing instructions, searching existing data sources, gathering and maintaining the data needed, and completing and reviewing this collection of information. Send comments regarding this burden estimate or any other aspect of this collection of information, including suggestions for reducing this burden to Department of Defense, Washington Headquarters Services, Directorate for Information Operations and Reports (0704-0188), 1215 Jefferson Davis Highway, Suite 1204, Arlington, VA 22202-4302. Respondents should be aware that notwithstanding any other provision of law, no person shall be subject to any penalty for failing to comply with a collection of information if it does not display a currently valid OMB control number. PLEASE DO NOT RETURN YOUR FORM TO THE ABOVE ADDRESS.					
1. REPORT DATE (DD-MM-YYYY) 02/29/08		2. REPORT TYPE FINAL REPORT		3. DATES COVERED (From - To) 7/1/04 - 6/30/07	
4. TITLE AND SUBTITLE Innovative growth and defect analysis of group III- Nitrides for High Speed Electronics		5a. CONTRACT NUMBER FA9550-04-1-0408			
		5b. GRANT NUMBER			
		5c. PROGRAM ELEMENT NUMBER			
6. AUTHOR(S) Dr. Petra Specht, Assoc. Res. Eng. Dr. Eicke R. Weber, Professor		5d. PROJECT NUMBER			
		5e. TASK NUMBER			
		5f. WORK UNIT NUMBER			
7. PERFORMING ORGANIZATION NAME(S) AND ADDRESS(ES) University of California, Berkeley 253 Cory Hall, Berkeley, CA 94720		8. PERFORMING ORGANIZATION REPORT NUMBER			
9. SPONSORING / MONITORING AGENCY NAME(S) AND ADDRESS(ES) AFOSR/NE 875 North Randolph Street, Rm. 3112 Arlington, VA 22203 <i>Dr. Kurt Reinhardt/NE</i>		10. SPONSOR/MONITOR'S ACRONYM(S)			
		11. SPONSOR/MONITOR'S REPORT NUMBER(S)			
12. DISTRIBUTION / AVAILABILITY STATEMENT DISTRIBUTION STATEMENT A: UNLIMITED		AFRL-SR-AR-TR-08-0168			
13. SUPPLEMENTARY NOTES					
14. ABSTRACT The project focused on novel techniques in growth and characterization which may enhance group III – nitride applications. On the growth side nitride deposition on diamond templates was characterized as the most promising novel growth techniques. The continuing progress can be supported applying the novel characterization technique described below. Local inhomogeneities are a common feature in group III – nitrides. With standard characterization methods such materials cannot be properly evaluated. Multiple group III – nitride epilayers were investigated utilizing VEELS in combination with high resolution TEM in order to characterize the materials in high spatial and energy resolution. It was found that possible side effects such as sample damage due to electron irradiation or falsified results due to retardation effects can be avoided if proper sample treatment is applied. It is assumed that the occurrence of local electronic transitions in close vicinity to interfaces is due to the presence of local point or surface defects. For the first time it may become possible to investigate the impact of such defects on the performance of devices. For the InGaN alloy system nano-cluster formation which changes optical responses was investigated. It was found that the III-V compound InN exists as a composite InN:In material. InN commonly exhibits multiple optical responses including an interface and/or surface related effect, which triggered confusing scientific models in the past. The prospect of exploiting multiple energy transitions within ONE material offers completely new alternatives for novel device development.					
15. SUBJECT TERMS Group III – nitrides, local material characterization, novel growth techniques, defect analysis					
16. SECURITY CLASSIFICATION OF:			17. LIMITATION OF ABSTRACT	18. NUMBER OF PAGES	
unclassified					
a. REPORT	b. ABSTRACT	c. THIS PAGE	None	84	19a. NAME OF RESPONSIBLE PERSON Eicke R. Weber
					19b. TELEPHONE NUMBER (include area code) 510 642-0205

20080404109

Table of Contents

Abstract	03
1. Introduction	04
2. Strain Measurement and the Detection of Clustering in In_xGa_{1-x}N by HR-TEM	05
3. Phase Separation, Clustering and Ordering in In_xGa_{1-x}N	27
4. Clustering in InN and the Bandgap Question	40
5. Optical Characterization of InN	47
6. Alternative Growth Methods for GaN:diamond substrates	66
7. Summary	70
8. Personnel	71
9. References	72
10. Publications	82

Abstract

The project focused on novel techniques in growth and characterization which may enhance group III – nitride applications. On the growth side nitride deposition on diamond templates and a first high pressure MOCVD deposition were characterized as the most promising novel growth techniques. Both techniques were still in their initial stages, their continuing progress may be supported applying the novel characterization technique described below.

Local inhomogeneities are a common feature in group III – nitrides. With standard characterization methods such materials cannot be properly evaluated. Multiple group III – nitride epilayers were investigated utilizing Valence Electron Energy Loss Spectroscopy in combination with high resolution TEM in order to characterize the materials in high spatial and energy resolution. It was found that possible side effects such as sample damage due to electron irradiation or falsified results due to retardation effects can be avoided if proper sample treatment is applied. It is assumed that the occurrence of local electronic transitions in close vicinity to interfaces is due to the presence of local point or surface defects. For the first time it may become possible to investigate the impact of such defects on the performance of devices. For the $\text{In}_x\text{Ga}_{1-x}\text{N}$ alloy system nano-cluster formation which changes optical responses was investigated. It was found that the III-V compound InN exists as a composite $\text{InN}:\text{In}$ material. InN commonly exhibits multiple optical responses including an interface and/or surface related effect, which triggered confusing scientific models in the past. The prospect of exploiting multiple energy transitions within ONE material offers completely new alternatives for novel device development.

1. Introduction

In the 1990^{ies} progress in epitaxial techniques brought III-V compound materials to the forefront of semiconductor research which up to that time was exclusively dominated by silicon based materials. Devices were rapidly developed and include laser diodes and multicolored light emitting diodes. Group III - nitrides have optical transitions from the infrared into the ultra violet and are used for light generation with a luminous flux of approximately 100 lumen/watt which surpasses fluorescent lamps. Nitrides also present excellent electronic properties such as high electron mobility and breakdown field ideal for high power, high frequency electronics.

Despite their attractiveness, group III – nitrides had a relative slow start into broad applications, partly due to the fact that they are complex to grow. An illustration of this is the difficulty of growing chemically homogeneous $\text{In}_x\text{Ga}_{1-x}\text{N}$ across the entire composition range. Similarly, high p-doping remains a challenge for all group III – nitrides and the heat transfer of operating devices is yet to be optimized. The goal of this project was to investigate novel growth techniques and develop reliable characterization techniques which support future group III – nitride device applications.

Many of the novel applications in optoelectronics use quantum effects such as confinement in heterostructures to boost their efficiency. As a consequence, the material needs to be engineered at a near atomic level to form nanoscopic structures that will drive the devices properties. Such small structures can be realized by epitaxy or self organization, but to analyze materials on such a small scale requires new techniques. Quantitative high resolution electron microscopy (HRTEM) is being developed precisely for this purpose. This final report covers a thorough investigation on $\text{In}_x\text{Ga}_{1-x}\text{N}$ alloys and the binary compound InN . In addition, GaN growth on diamond substrates is discussed.

Besides some fundamental conclusions such as the question about the bandgap of InN and the origin of the photo-luminescence in $\text{In}_x\text{Ga}_{1-x}\text{N}$, opportunities and challenges of improved heat transfer in GaN -based devices were part of this investigation. For the material characterization epilayers grown in-house (Berkeley), St. Petersburg, Russia, Cornell, USA and two suppliers of GaN on diamond (sp3 Inc. / group4labs), both located in California, were used. The usefulness of local characterization is demonstrated.

2. Strain Measurement and the Detection of Clustering in $\text{In}_x\text{Ga}_{1-x}\text{N}$ by HRTEM

The measurement of local lattice parameters from HRTEM images is a widespread technique that has been used extensively to measure the chemical (in)homogeneity of $\text{In}_x\text{Ga}_{1-x}\text{N}$. In a mismatched heterostructure, the lattice displacement depends on the chemical composition and strain that may distort the crystalline unit cells. In the case of $\text{In}_x\text{Ga}_{1-x}\text{N}$, sample damage, unstable imaging conditions and an insufficient estimation of errors and detection limits have led to much confusion about whether indium clustering is present in this material. This discredited quantitative HRTEM as a reliable source of physical insight. However HRTEM, because of its high spatial resolution and sensitivity is a valuable tool in the analysis of nanomaterials and clusters. It is thus imperative to present an analysis of the conditions under which HRTEM, and strain analysis in particular, is able to provide reliable quantitative information about the sample.

First, the conditions under which quantitative HRTEM analysis can be conducted need to be established. The points to address comprise

- (a) adequate sample preparations techniques,
- (b) the control of electron beam damage, and
- (c) the effect of unstable imaging

conditions. Then, the precision and detection limits of the method need to be explored. This includes a separation of effects due to strain and to chemical composition. This chapter will demonstrate that strain mapping can be an appropriate tool to probe for an inhomogeneous distribution of atoms in an alloy, provided that strain fields are large enough and sources of error are carefully examined. Indeed, the high strain in $\text{GaN}/\text{In}_x\text{Ga}_{1-x}\text{N}$ heterostructures makes strain mapping the "tool of choice" for this material system.

2.1 The validity of strain measurements

As in any experiment, sources of error in quantitative HRTEM need to be carefully examined and have been discussed in recent literature. However, the discussion is centered on an often symptomatic description of beam damage and offers little insight on how to avoid it. This section differentiates three contributions that can restrain the validity of strain measurement.

First, the effects of damage to the sample, in particular related to beam damage is discussed in the light of publications on the subject. Second, microscope instabilities and their effect in current low voltage machines are studied. Finally the remaining sources of error need to be quantified to establish the detection limits for chemical inhomogeneity and clustering.

HRTEM images are susceptible to undesired contributions stemming from surface roughness due to sample preparation or damage induced by the imaging beam. This masks and falsifies information intrinsic to the sample. Surprisingly, the primary source of damage in TEM samples - mechanical abrasion or bombardment with high energy ions during sample preparation- attracted very little attention from the scientific community. Instead it concentrated on effects due to the electron beam. This section addresses

concerns over beam damage first, and then highlights the need for an adequate sample preparation procedure.

The discussion is centered on $\text{In}_x\text{Ga}_{1-x}\text{N}$ and the question over its chemical (in)homogeneity, but it will be shown that damage in this alloy is similar to other semiconductors. The $\text{In}_x\text{Ga}_{1-x}\text{N}$ system has been extensively studied by quantitative HRTEM and large lattice constant variations in $\text{In}_x\text{Ga}_{1-x}\text{N}$ quantum wells (QW) were interpreted as indium rich clusters [Seg04, Rut02]. These clusters were thought to be responsible for the excitonic localization as demonstrated by optical experiments [Kre02, Bar04].

Recently, it has been pointed out [O'N03, Sme03, Sme06, Li05b] how beam damage in $\text{In}_x\text{Ga}_{1-x}\text{N}$ heterostructures can lead to a false detection of clusters. Figure 2.1 shows a beam damage study on $\text{In}_x\text{Ga}_{1-x}\text{N}$ QWs performed by Smeeton et al.. The images were

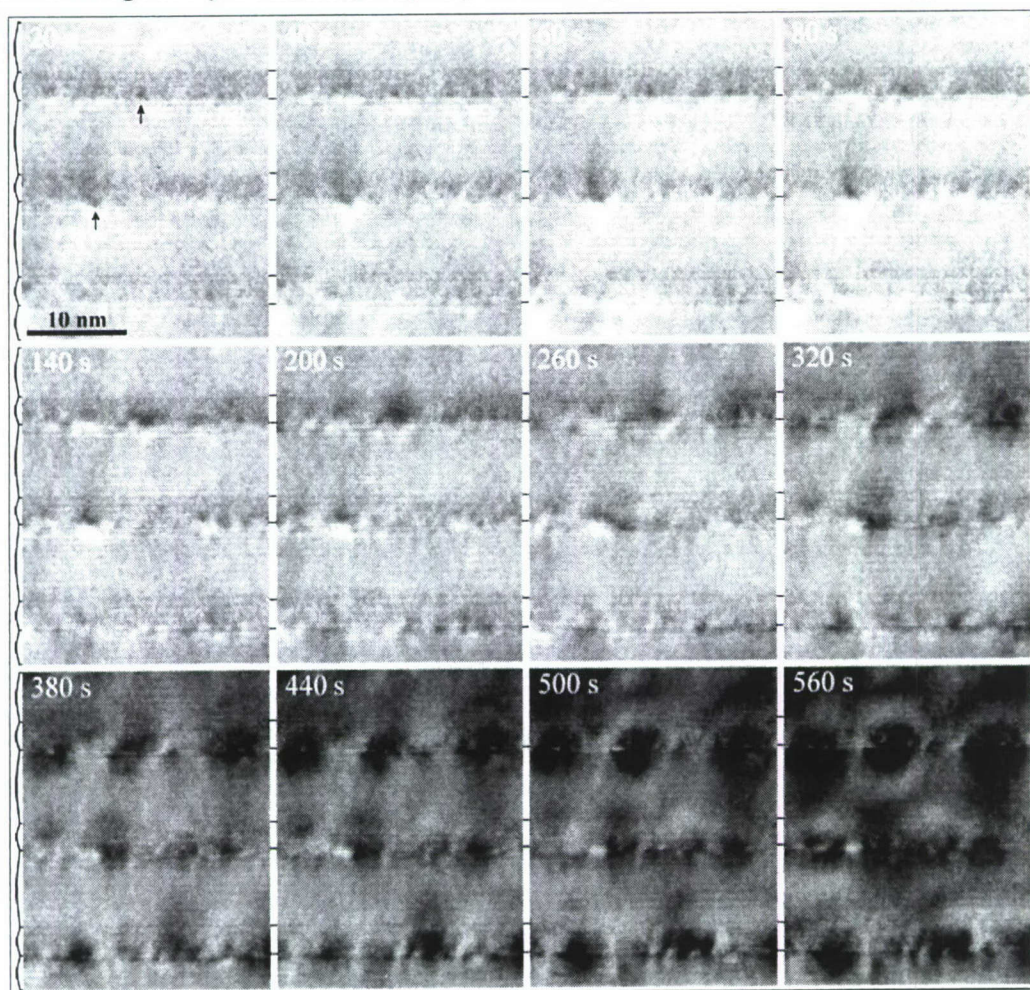


Figure 2.1: Beam damage studies on an $\text{In}_x\text{Ga}_{1-x}\text{N}$ heterostructure by Smeeton et al.. Note how damage is already present in the very first picture taken. The strain maps react sensitively to the damage [Sme06].

Recorded on Tecnai F20 G2 operated at 200 kV with beam currents of 35 A/cm². The QW seems to be more susceptible to the electron beam where damage was already present in the first image (spots of dark contrast). It was suggested that sample damage by the electron beam irradiation is the primary damage source and may be unavoidable [Hum07].

Indeed, beam induced damage has been a concern for many years, particularly during the development of early quantitative tools that extract element distributions or interface roughness from lattice images [Our89b, Our90, Kis95]. Debates about such radiation damage in GaAs/Al_xGa_{1-x}As/GaAs barrier structures can serve as an example [Dev90]. In fact, it is not surprising that GaN/ In_xGa_{1-x}N /GaN QW structures – as most other materials – become heavily distorted if they are irradiated for up to 1200 seconds [O’N03] with current densities up to 100 A/cm² [Sme03, Li05b] in electron microscopes operated between 200 kV and 400 kV.

In general, however, the electron beam can only be a secondary source of damage in TEM samples when compared to a sample preparation that uses mechanical abrasion and bombardment with high energy ions. Indeed, the sample preparation procedure is designed to be a damaging process. When discussing damage in TEM experiments it must thus be considered first since it is difficult to differentiate beam damage from damage that was present even before imaging took place. The micrographs of In_xGa_{1-x}N QWs in [Rut02] can serve as an example for such a case.

As an illustration, Figure 2.2 shows the effect of electron dose exposure with beam currents of 70-80 A/cm² to sapphire, GaN and InN. All materials are devoid of damage after a few seconds of exposure, but after prolonged irradiation beam damage in the form of contrast appears and the lattice is distorted and blurred. Changes in defocus could lead to a similar “appearance” of damage, but the sample was prepared by low energy ion milling and showed even contrast for different defoci when first imaged.

If displacement maps are applied to images taken from damaged samples, the extracted strain will be dominated by artifacts. These effects are demonstrated by Smeeton et al. in their beam damage studies [Sme03, Sme06]. It should be noted, that none of the studies published about In_xGa_{1-x}N used a wet etching technique that we recommend for this type of material. As a result, studies conducted by these groups have the problem of samples that are damaged even before irradiation. Indeed, Smeeton himself identifies damaged areas in the very first picture in Figure 2.1 after only a few seconds of irradiation that is certainly due to sample preparation. The damage naturally increases with time at exactly the same location.

Inadequate sample preparation is, unfortunately, widespread in the In_xGa_{1-x}N literature and is the cause for erroneous interpretation of strain measurements as clustering with high amplitude or even reports of pure InN clusters. As a result, quantitative interpretation of HRTEM image was henceforth seen with some isection [Sme06, Li05b, Gal07].

Naturally, it is appropriate to strive for avoiding beam damage entirely. Since long, there is general understanding that such concerns are addressed by minimizing recording times and current densities (e.g. [Our90, Dev90]). In fact, it is of essence and good practice to characterize images during early exposure stages ($t \leq 120$ sec), which provides enough

time to record the necessary images in many cases. This is possible in $\text{In}_x\text{Ga}_{1-x}\text{N}$ just as it is possible in many other radiation sensitive materials such as $\text{Al}_y\text{Ga}_{1-y}\text{N}$, $\text{Si}_z\text{Ge}_{1-z}$, or $\text{Al}_q\text{Ga}_{1-q}\text{As}$. On a time scale of up to two minutes, radiation damage can be avoided by minimizing the electron dose, as illustrated in the micrographs of Figure 2.3. The samples are prepared with a final surface cleaning step that involves either ion milling with low energy ions [Bar98] or chemical etching with KOH produces have surfaces that are smooth on an atomic scale [Jin06]. As a result such samples show contrast due to thickness and focus change, crystal tilt, or varying lens aberrations. Radiation damage can be promptly recognized as spots appearing in the lattice images with increasing exposure time.

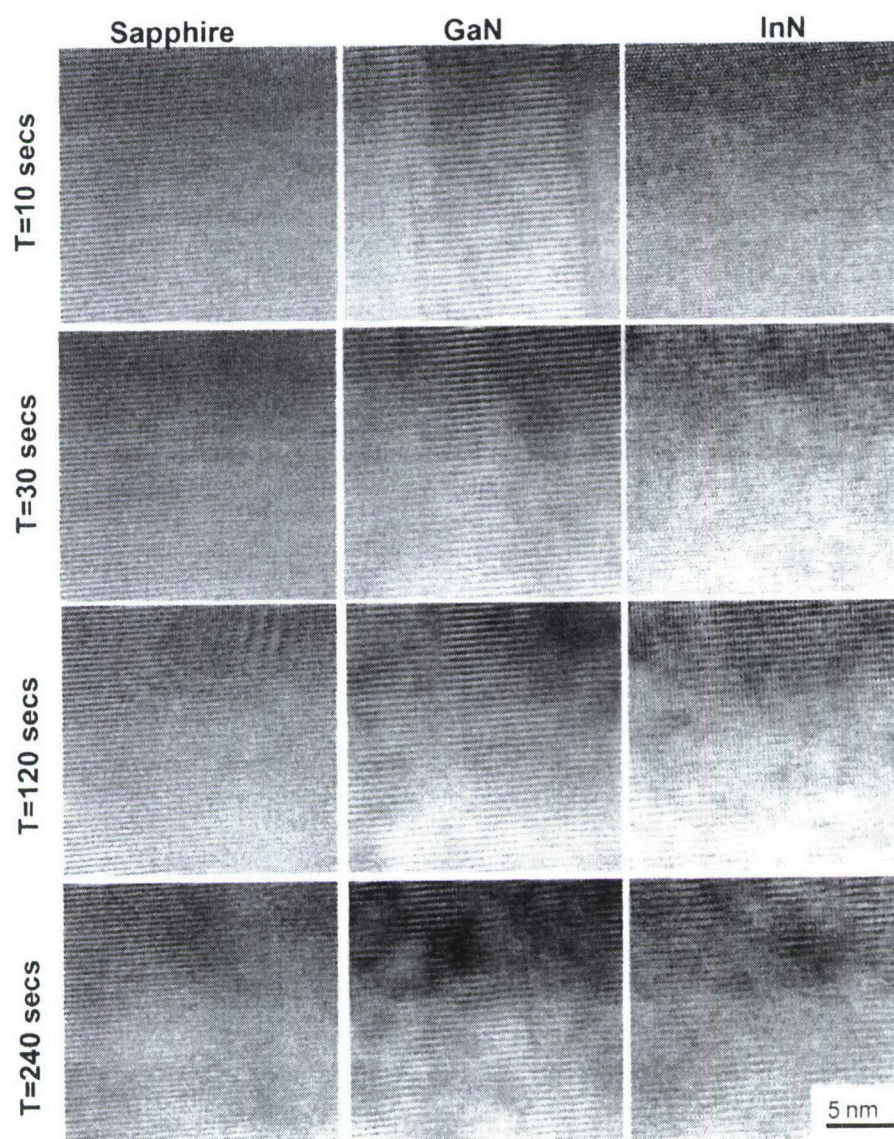


Figure 2.2: Irradiation series in sapphire, GaN and InN with beam currents of 70-80 A/cm^2 at 300 kV for the indicated times. At these irradiation intensities, it is seen that a blurring of the lattice is observable after 30 seconds in *all* material systems.

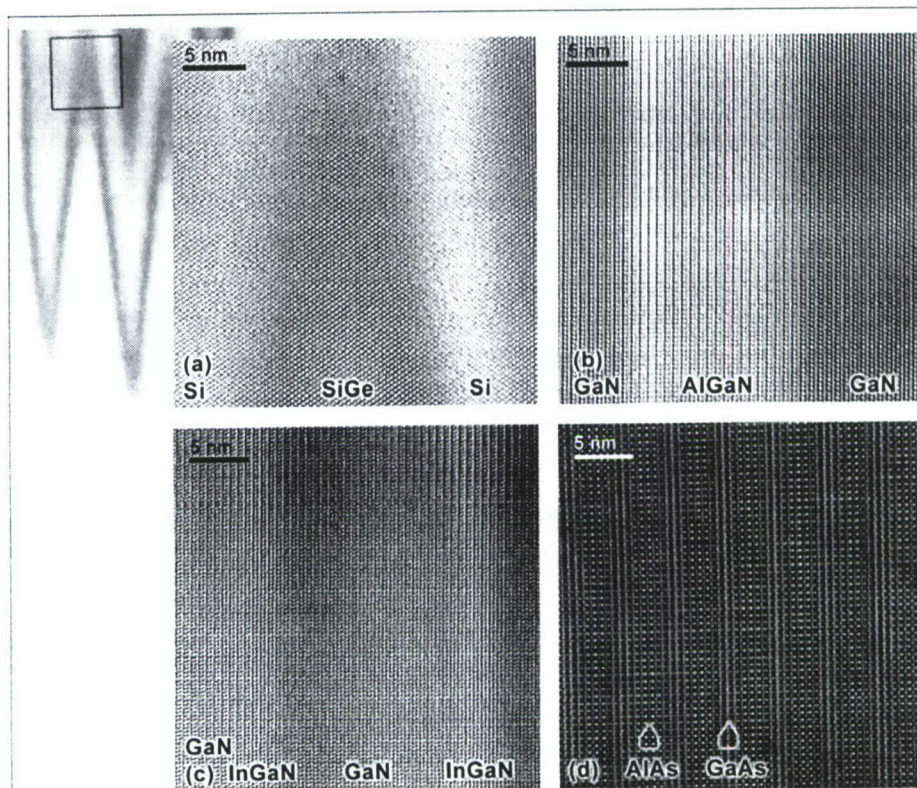


Figure 2.3: Micrographs for the indicated material systems show how wet etching or low energy ion milling produces extremely flat samples, with homogenous contrast. Beam damage, if present would be easily recognizable. For a detailed description see text.

A description of the images shown is given next:

- a) The $\{110\}$ lattice image shows a periodic Si/Si₇₅Ge₂₅/Si QW structure that was chemically etched with KOH. The sample was grown by Molecular Beam Epitaxy (MBE). Preferential etching of the Si₂Ge_{1-z} produces the comb-like shape of the sample. Extinction oscillations form a homogeneous alternation of bright and dark contrast with increasing sample thickness. The image was recorded with a JEOL 4000ex [Kis95].
- b) and c) show lattice fringe images of GaN/Al_xGa_{1-y}N/GaN and GaN/In_xGa_{1-x}N/GaN QW structures recorded in $\{11\ 20\}$ projection that were grown by Metal Organic Chemical Vapor Deposition (MOCVD) [Kis95, Per98]. The samples were thinned by milling with argon ions and chemically etched. Images were recorded with NCEM's Atomic Resolution Microscope operated at 800 kV.
- d) The depicted $\{100\}$ GaAs/AlAs superlattice was grown by MBE. The sample was prepared by milling with argon ions accelerated by 500V in a Linda ion mill. The image was recorded with the One Ångström Microscope (OÅM) at NCEM (Philips CM300 operated at 300keV).

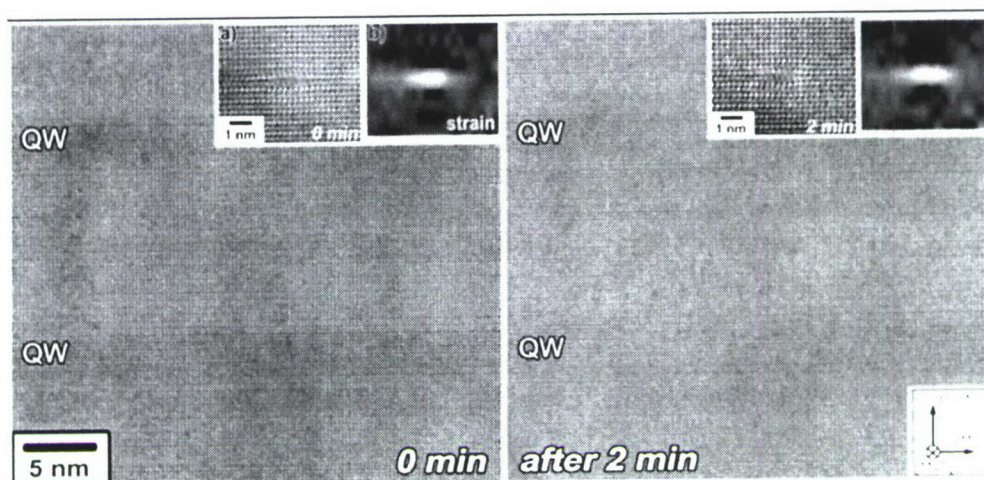


Figure 2.4: Two lattice images of a time series recorded at 800 kV with the ARM. The insets show intentionally generated defects grown into the QWs and the corresponding displacement maps [Jin06]. No radiation induced structural changes are observable.

In all cases, contrast is sensitive to radiation damage and its homogeneity ensures that no beam damage is present in the sample. It was recently reported that GaN/In_xGa_{1-x}N/GaN is stable under irradiation with 800 kV if exposure times are kept below 2 minutes [Jin06]. Figure 2.4 shows two lattice images of a time series without any recognizable sign of radiation damage. The insets depict a magnified view of a defect that was intentionally grown into the QW and its related displacement map: the displacement maps are reproducible.

In summary, a quantitative assessment of information from HRTEM images is often challenging since sample thinning to electron transparency (thickness < 20 nm for accelerating voltages > 400 kV) can be a damaging process if milling with ions accelerated to several kV are used. In fact residual damage from the sample preparation is often visible in lattice images and it is difficult if not impossible to distinguish between ion beam induced damage and electron beam damage. With an adequate sample preparation, damage free samples can be produced and beam damage in In_xGa_{1-x}N is comparable to other material systems. Indeed, such samples can be imaged for up to 2 minutes without the appearance of any further damage as will be demonstrated in the next section.

2.1.2 The significance of acceleration voltage and microscope stability

Most of the recently published HRTEM studies on In_xGa_{1-x}N were performed on microscopes with accelerating voltages of 150 – 300 kV. To test the apparent indium distribution in In_xGa_{1-x}N during electron irradiation, time series of high-resolution lattice images were examined. By comparison with theory it is reasoned that sample preparation and microscope stability will be essential factors that determine the reliability of the results.

Time series were recorded on the OAM operated at 150 kV. The left side of Figure 2.5 shows selected areas of four images from a series of 17 images recorded in time intervals

of 6 seconds. The sample surface is clean and shows no beam damage after exposure times of up to 2 minutes under moderate beam currents (20 A/cm^2). The right side of the figure displays the corresponding displacement maps that were generated by the DARIP program (available at NCEM, LBNL). Closer inspection of the lattice images reveals only minor variations of the image pattern. The displacement maps, however, appear unstable. If the displacements were interpreted in terms of an indium fluctuation, the images would very well reproduce results from the debated literature reports [O’N03, Sme03, Sme06, Li05b] even though other lens aberrations than defocus, such as astigmatism or coma, may be of importance there.

Image simulation is used to elucidate the effects that play a role when forming an image in HRTEM. In a simulation, the thickness and defocus of the sample can be varied arbitrarily. Indeed, the sample preparation can introduce surface roughness that alters the sample thickness locally and microscope instabilities result in uncontrollable focus changes.

Figure 2.6 shows a matrix of simulated HRTEM images as computed with the software package MacTempas [Kil07] for GaN in $[1\bar{1}00]$ zone axis calculated for three commonly used accelerating voltages of 800, 300 and 150 keV. The simulation demonstrates how the pattern in the image plane does not reflect the actual position of atom columns in the sample (as indicated by the atom overlay in the upper right frame). Further, it is seen from the simulations that both thickness variations and changes in defocus can introduce pattern changes that may falsify displacement field measurements [Bar06]. It becomes a matter of magnitudes of the changes if such effects can be neglected or not.

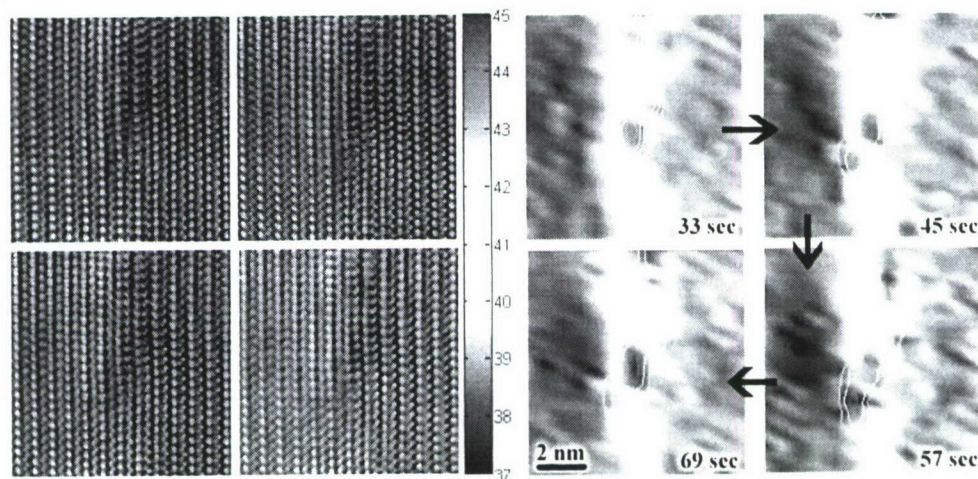


Figure 2.5: Left: Four lattice images of a time series of 17 images recorded at an accelerating voltage of 150 kV with a nominally constant defocus (beam current: 20 A/cm^2). Right: Corresponding displacement maps. Unit cell expansions are measured in pixels and color coded as indicated.

It is seen from Figure 2.6 that there are thickness-defocus windows where image patterns remain fairly constant. Their extension depends drastically on the acceleration voltage because electron scattering is voltage dependent. The window is widest for experiments

at 800 kV where it can span over tens of nanometer of focus and thickness. Measurements at this acceleration voltage are thus most uncritical. At 150 kV contrast inversion occurs from instabilities of a few nanometers only and it is experimentally challenging to acquire lattice images with stable patterns from such narrow windows. Additionally, one must expect that these windows are smaller if field emission technology is employed instead of thermal emitters because of an extended information limit that adds complexity to the image (e.g. [Rei89]). Thus, thickness changes across the field of view must lie below a few nanometers and focus must be stabilized on a similar scale to stay within the appropriate thickness/defocus windows.

Sample roughness can be controlled by appropriate preparation as described in Section 1.6. Only the focal stability of modern microscopes remains of concern. Figure 2.7 characterizes the mechanical and electrical stability of the OÅM at NCEM by measuring focus values in 6 second time intervals. It is seen that focus variations of up to 20 nm from a linear fit can be present. They are caused by common environmental noise such as personal walking and closing doors within the building that houses the OÅM. Even if absent during off hours operation ©, errors of up to 10 nm still cannot be avoided because of limited lens current stabilities. Considering that the OÅM is one of the world's highest resolution microscope it is clear that better stabilities can at present rarely be achieved. These instabilities explain the strain pattern variations observed in the image series shown in Figure 2.5.

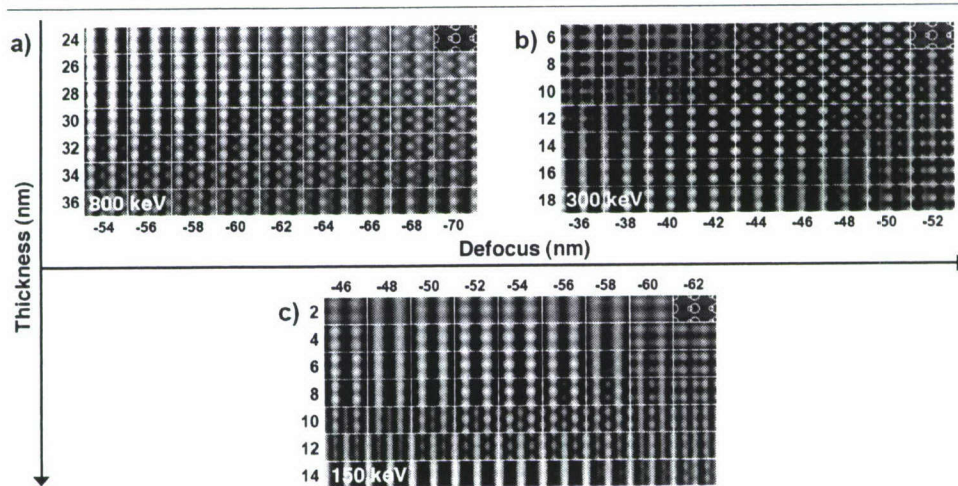


Figure 2.6: Simulated thickness-defocus maps of GaN $\{1 \bar{1}00\}$ for acceleration voltages of 800 kV (a), 300 kV (b), and 150 kV (c). Windows of constant pattern are largest at 800 kV and smallest at 150 kV where they are only 4-6 nm wide.

The approach followed here is different from the results discussed in Ref. [O'N03, Sme06, Li05b] since it makes use of established knowledge addressing radiation damage in materials by dose reduction and fast recording of successive images. Even so, at low voltages, microscope instabilities yield image distortions that can violate the application rules for strain mapping from lattice images. Resultantly, indium composition maps can appear unstable. The data extracted from such measurements must thus be compared in a

quantitative manner that must include an assessment of errors in the composition profiles. Noise analysis of the images reveal that the differences from image to image are random.

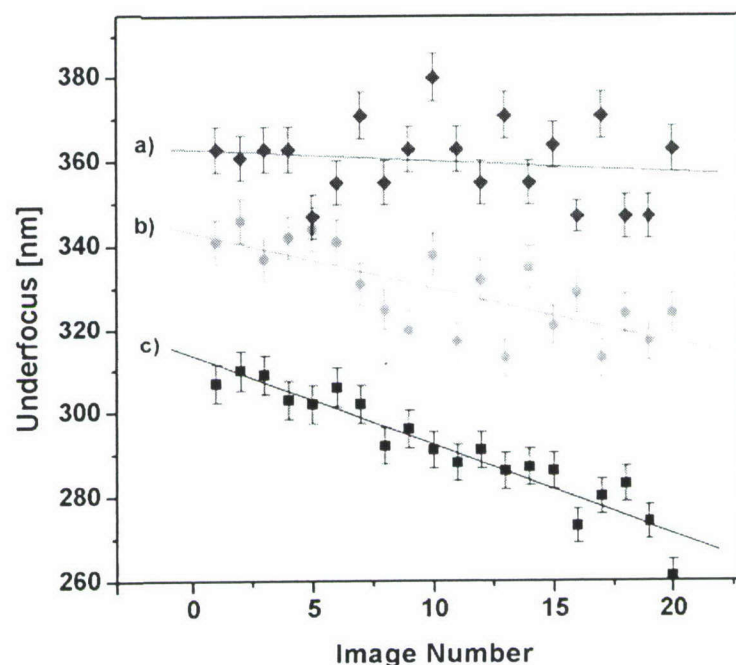


Figure 2.7: Time dependent defocus measurements. Subsequent images are recorded in 6 second intervals. Measurements a), b) are influenced by common environmental noise. In c), taken during off-hour operation, only microscope instabilities contribute to the data scatter. A) Microscope is set to “no defocus change” between successive images. B), c) Microscope is set to change defocus by $\Delta f = 1.5$ nm between successive images.

There is no systematic change such as indium redistribution or beam damage up to 2 minutes. This proves that the inhomogeneities were present in the initial material already. Resultantly, statistical analysis can be used to evaluate the precision and increase the confidence of the measurement.

2.1.3 Precision of strain measurements

In order to further quantify the data from the entire image series, grid cells in columns parallel to the QW were averaged to calculate mean displacements and their standard deviation. The mean and standard deviation are plotted as time dependent profiles in Figure 2.8. This process reduces statistical noise by the square root of the 45 cells that were used for averaging ($\sqrt{45} = 6.7$), which causes a better data reproducibility of profiles when compared to maps.

Still, the standard deviation varies from one image to the next. But, the variations are purely random and the profiles from all images can again be averaged into a single profile. Figure 2.9 plots the averaged displacement with the corresponding averaged standard deviations included as error bars. Since the standard deviation in regions of GaN

is never smaller than 2 pm it must be expected that in single unit cells of composition maps the noise can be almost as large as the signal itself, i.e. 14 pm. Indeed such an effect can be observed in Figure 2.5 where regions of high apparent strain appear and dissolve in the course of 30 seconds.

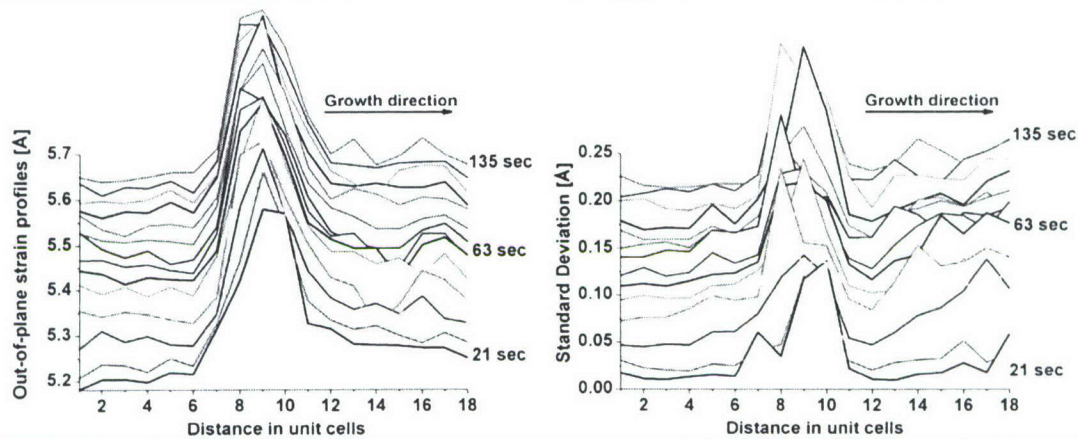


Figure 2.8: (a) Waterfall diagram of the averaged composition profiles of 17 images from the time series ($\Delta t = 6$ sec). (b) Standard deviation profiles. The presence of indium fluctuations is established by large values in the QW region only.

Further, the profile can be interpreted with some confidence. It is seen from the displacement in Figure 2.9 that the QW is asymmetrical with respect to the growth direction. The interface to the substrate is almost abrupt, whereas the interface with the caplayer is more diffuse. Indeed, there is a residual strain of 2% - 5% in the GaN layer on top of the QW indicating, that indium floated into the caplayer during growth.

At this point, it is essential to realize that unlike any concentration profile measurement in GaAs/ $\text{Al}_q\text{Ga}_{1-q}\text{As}/\text{GaAs}$ [Our90], the calculated standard deviations in $\text{In}_x\text{Ga}_{1-x}\text{N}$ QWs largely exceed the values of the surrounding GaN matrix. This suggests that there is an inhomogeneous element distribution in the GaN/ $\text{In}_x\text{Ga}_{1-x}\text{N}$ /GaN heterostructure. From the averaged profile of Figure 2.9 it is also seen that the indium fluctuations are composition dependent since the error bars increase with increasing strain (higher indium content).

In GaN a precision of 2 pm at unit cell resolution can be reached [Kis98b] and the increase of σ_{total} proves that random alloy fluctuations and/or cluster formation present in $\text{In}_x\text{Ga}_{1-x}\text{N}$ can be accessed by strain measurements.

The exact shape of the inhomogeneities cannot be extracted from maps since data averaging across the samples' thickness is needed. This is unfortunate since knowledge of the exact size and localization would be of interest to understand the mechanism behind the inhomogeneity of $\text{In}_x\text{Ga}_{1-x}\text{N}$ QWs.

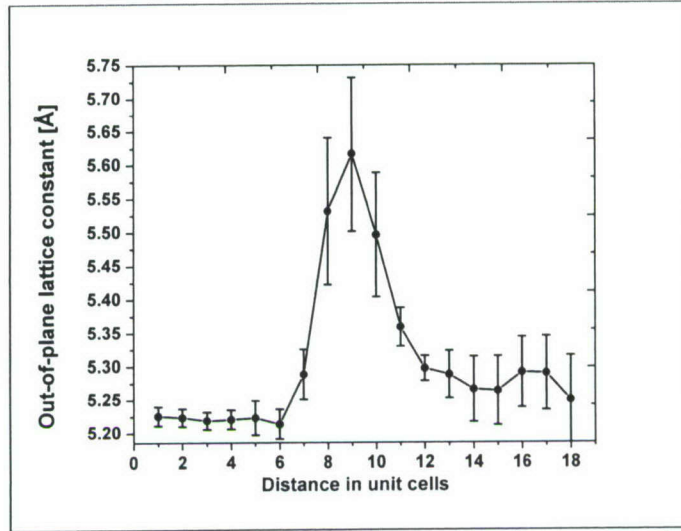


Figure 2.9: Composition profile of the of the entire image series. The standard deviation σ_{total} is plotted as error bars. In comparison to errors in Figure 2.5 the statistical noise is reduced by a factor of 7.

2.1.4 Differentiating random alloying and clustering

This section establishes detection limits that are required to distinguish between random alloy fluctuations and the formation of atom clusters. In thin TEM foils a precision of 2 pm relates to the detection of only a few atoms – and even single atoms if the lattice mismatch is large enough – since typical HRTEM samples are only 10 – 30 nm thick. For example in $\text{In}_{0.5}\text{Ga}_{0.5}\text{N}$ [11 $\bar{2}0$], an atom spacing of 0.27 nm along the beam direction translates into 40 atoms in one column that is 10 nm tall (sample thickness). In this case a substitution of two gallium atoms by two indium atoms corresponds to a concentration change $\Delta x = 0.05$ in the column and causes a lattice distortion of 2.5 pm according to Vegard's law.

In a random alloy A_xB_{1-x} the distribution of the atoms follows Poisson statistics. The standard deviation σ_{alloy} from the mean stoichiometry in a probed volume containing N atoms produces strain variations of

$$\sigma_{\text{alloy}} = \frac{\sqrt{Nx(1-x)}}{N} \alpha. \quad (2.1)$$

where α is a factor transforming a chemical composition into a displacement field. α depends on the strain state of the layer and will be determined in Section 2.2. In $\text{In}_{0.5}\text{Ga}_{0.5}\text{N}$, for example, the expected concentration variation of a binomially distributed alloy in an atomic column containing 100 nuclei amounts to $\sqrt{100/4}/100 = 5\%$. This translates into displacement fields between 2.5 and 6 pm depending on the strain state of the sample.

Consequently, even a random substitution of atoms will create local displacement fields that can be measurable. Ideally, one would test strain measurements with materials that are believed to be chemically homogenous to establish detection limits. If the probed

volume is sufficiently small and the precision high enough, the measurements on a miscible alloy should reveal the statistical fluctuations according to Equation 2.1, else ordering is present in the alloy. If, however, experimental noise exceeds such effects, it is pointless to speculate about the homogeneity of an impurity distribution.

The lines in Figure 2.10 estimate strain fluctuations that originate from a random substitution of atoms according to Equation 2.1. The sample thicknesses are expressed in numbers of atoms. For example, a unit cell of GaN in $[1\ \bar{1}00]$ projection (0.16/0.52 nm) that probes three atomic columns containing a total of 50, 100, 200, or 300 atoms is about 5, 9, 18, and 27 nm tall. These values are chosen such that typical sample thicknesses for lattice imaging are represented. A precision around 1 pm would be required to access σ_{alloy} in $\text{Al}_y\text{Ga}_{1-y}\text{N}$ or $\text{Si}_z\text{Ge}_{1-z}$ materials. This high precision requirement for displacement measurements is a direct consequence of the relatively small lattice mismatches in the Si/Ge (4 %) and GaN/AlN (-2 %) alloys. Random alloy fluctuations must cause larger displacements in materials systems such as InAs/GaAs or InN/GaN because of the larger lattice mismatch of 7% and 12%, respectively. However, it was shown that the distribution of indium in GaAs is not random [Zhe94], which excludes $\text{In}_w\text{Ga}_{1-w}\text{As}/\text{GaAs}$ as a test object.

Experimentally, the standard deviation of the chemically sensitive parameter (c-lattice parameter in $\text{In}_x\text{Ga}_{1-x}\text{N}$) is computed along the heterostructure and is used as a measure of all errors σ_{total} . In ordered materials such as Si, AlN, GaN or InN, $\sigma_{\text{total}} = \sigma_{\text{noise}}$ which defines the precision of the measurement. Alloying will add a contribution due to random alloying or clustering that can be significant if the experimental noise limits are small enough. For a random alloy, σ_{total} is given by

$$\sigma_{\text{total}} = \sqrt{\sigma_{\text{noise}}^2 + \sigma_{\text{alloy}}^2} \quad (2.2)$$

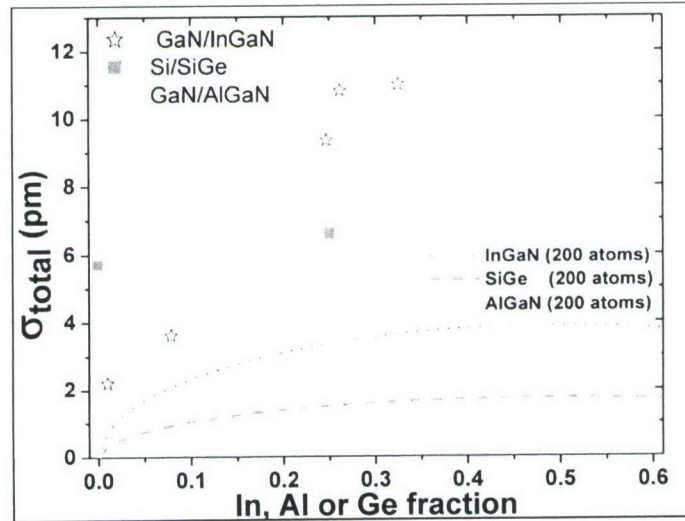


Figure 2.10: The standard deviation σ_{total} of the c-lattice constant is plotted over the average concentration for QWs of different alloys. σ_{noise} is given by measurement in the substrate ($x; y; z = 0$). $\text{In}_x\text{Ga}_{1-x}\text{N}$ exhibits a qualitatively different behavior from $\text{Al}_y\text{Ga}_{1-y}\text{N}$ and $\text{Si}_z\text{Ge}_{1-z}$. An upper limit to σ_{alloy} has been computed with Equation (2.1) for the relevant samples.

In the case where clustering is present in the material, σ_{alloy} no longer adequately describes the distribution as atoms do not follow Poisson statistics. Instead, it is replaced by a new contribution σ_{cluster} stemming from clustering

$$\sigma_{\text{total}} = \sqrt{\sigma_{\text{noise}}^2 + \sigma_{\text{cluster}}^2} \quad (2.3)$$

Figure 2.10 shows σ_{total} values from measurements of $\text{Al}_y\text{Ga}_{1-y}\text{N}$ (triangles) and $\text{Si}_z\text{Ge}_{1-z}$ (squares) heterostructures shown in Figure 2.3 and from the $\text{In}_x\text{Ga}_{1-x}\text{N}$ QW from Section 2.1.2 (stars). Σ_{noise} is given by measurements at $x,y,z = 0$. The precision in $\text{Al}_y\text{Ga}_{1-y}\text{N}$ (triangles) and $\text{Si}_z\text{Ge}_{1-z}$ is insufficient to resolve random alloy fluctuations, which is also due to the small strain involved. In $\text{In}_x\text{Ga}_{1-x}\text{N}$ $\sigma_{\text{noise}} = 2$ pm and this fluctuation would be accessible. However, the standard deviation cannot be explained by Equation 2.2 for $x > 0.2$ at a sample thickness of 200 atoms, which means that clustering is present at these concentrations.

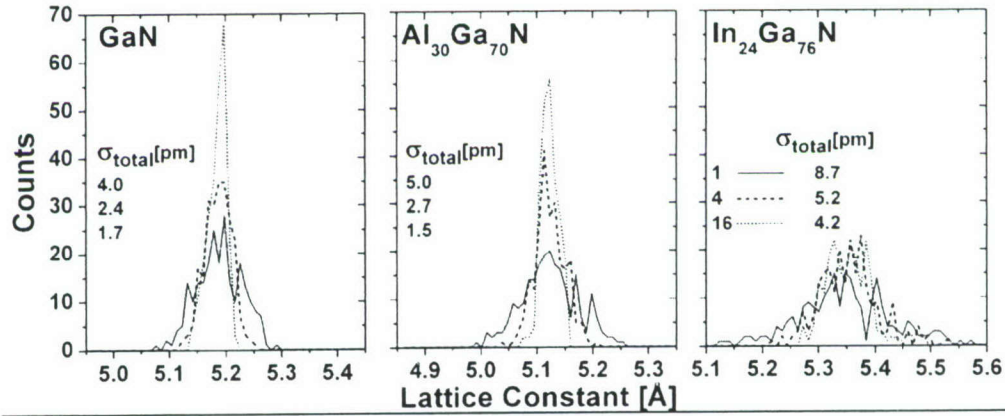


Figure 2.11: Histograms of the out-of-plane lattice constant recorded between 15 and 30 nm from the sample edge. Unit cells were averaged across 1 (full line), 4 (dash) and 16 (points) data points. Precision is gained as given by σ_{total} in GaN. The averaging has little effect in $\text{In}_x\text{Ga}_{1-x}\text{N}$ due the presence of clusters that produce a greater inhomogeneity than expected in a random alloy.

A way to increase the precision of strain measurements is to average over several measurements. Concurrently, the number N of atoms that are being probed in this way are also increasing, lowering the possible impact of σ_{alloy} . Figure 2.11 plots the histograms of strain measurements performed in a thick (non relaxed) sample area of the GaN/ $\text{In}_x\text{Ga}_{1-x}\text{N}$ / $\text{Al}_y\text{Ga}_{1-y}\text{N}$ heterostructure studied in the next section. The histograms are given for three different resolutions: at maximum resolution, i.e. one unit cell and averaged over 4 and 16 measurements. While histograms in GaN and $\text{Al}_y\text{Ga}_{1-y}\text{N}$ sharpen as would be expected from a random measurement (The standard deviation does not decrease as quickly as expected from a true random measurement, indicating that measurements are still correlated due to local changes in contrast), $\text{In}_x\text{Ga}_{1-x}\text{N}$ stays wide as a result of its clustering.

It is important to realize, that the precision of displacement measurements critically depends on the quality of the images. Results can differ from image to image and

sometimes even change across one field of view. It is thus important to measure σ_{noise} anew for every image. It is also necessary to estimate the thickness of the sample to discriminate apparent clustering due to random alloying and clustering due to phase separation. In the next section thickness effects in strain measurements are studied in depth.

2.2 Thickness effects and strain relaxation

Samples to be analyzed with HRTEM have to be thinned to electron transparency, usually well below 100 nm. In heterostructures of lattice mismatched materials the lattice strain can relax which will affect the measured strain. When using high accelerating voltage, it is possible to choose areas that are thick enough for relaxation effects to be negligible. The displacement measured is then a combination of strain and a change in chemical composition; Vegard's law can no longer be applied. For various reasons it is advantageous to analyze thin areas. In thin areas relaxation can be observed and isolated from chemical composition. Further, in the case of inhomogeneous material for instance, it is interesting to sample small volumes in order to minimize averaging through the thickness of the sample. This holds in particular if the inhomogeneities are on a nanometer scale. Finally, advanced techniques such as exit wave reconstructions or high resolution imaging with low electron energy need thin samples to be applicable.

In thick samples, the tetragonal distortion of strained heterostructures can easily be taken into account, as it is determined by the Poisson ratio under biaxial strain conditions. Treacy and Gibson showed how strain present in the original material can be relaxed in TEM foils [Gib84, Gib85, Tre86]. In the thin sample limit, the layer is expected to relax into a mono-axially strained state [Ros06]. Strain relaxation in TEM samples has been modeled in the literature using analytical approaches as well as finite element techniques [Tre86, Che89, Chr94, DC97, Til00, Ros06].

However, in all studies the sample is considered to be an infinite foil of constant thickness, i.e. the most relaxed state the heterostructure can reach is where only one of the lattice parameters in the growth plane is completely relaxed (monoaxially strained case). However, real samples are generally shaped like a steep wedge and it can be misleading to talk about a "thin foil". As a result suitably thin areas are often located very close to the sample edge. Here, buckling is present not only at the entrance and exit surface of the electron beam, but also towards the edge of the sample. Consequently the sample can bulge outward into the vacuum in a 3D buckle. This leads to a whole new range of effects, in particular because it can lead to an elastic expansion of the unit cell leading to states different from the ones expected in the model of tetragonal distortion. The relevance of these effects is not limited to TEM samples, but it is also expected that nanostructures such as nano-rods and nano-particles show similar relaxation behaviors.

Figure 2.12a shows the $\text{GaN}/\text{In}_x\text{Ga}_{1-x}\text{N}/\text{Al}_y\text{Ga}_{1-y}\text{N}$ heterostructure that will be studied in this section. It is grown by MOCVD on a sapphire substrate with a GaN buffer, a 3.2 nm $\text{In}_x\text{Ga}_{1-x}\text{N}$ QW and a 40 nm of $\text{Al}_y\text{Ga}_{1-y}\text{N}$ cap layer. Lattice images were recorded in 1998 with a JEOL Atomic Resolution Microscope (ARM) on plates by C. Kisielowski. The zone axis is $[11\bar{2}0]$. The high accelerating voltage (800keV) yields wide defocus and thickness windows with a homogenous image pattern as shown in Section 2.1.2. It can be seen from the homogeneous contrast across the micrograph that beam damage is not

detectable in our sample. Under such conditions the $\text{In}_x\text{Ga}_{1-x}\text{N}$ QW appears at least as unstructured as recently reported [Hum07]. The lattice image in Figure 2.12a shows extinction oscillations indicating that the sample is wedge shaped from left to right. The oscillations are perpendicular to the $\text{In}_x\text{Ga}_{1-x}\text{N}$ QW, such that the sample thickness can be considered constant across the heterostructure. The local thickness of the sample is determined by fitting the underlying gray level oscillations to extinction oscillations with solutions of the Pendellösung for the (0000) beam in GaN [11 $\bar{2}0$] (Figure 2.12b) as calculated with the software package MacTempas [Kil07].

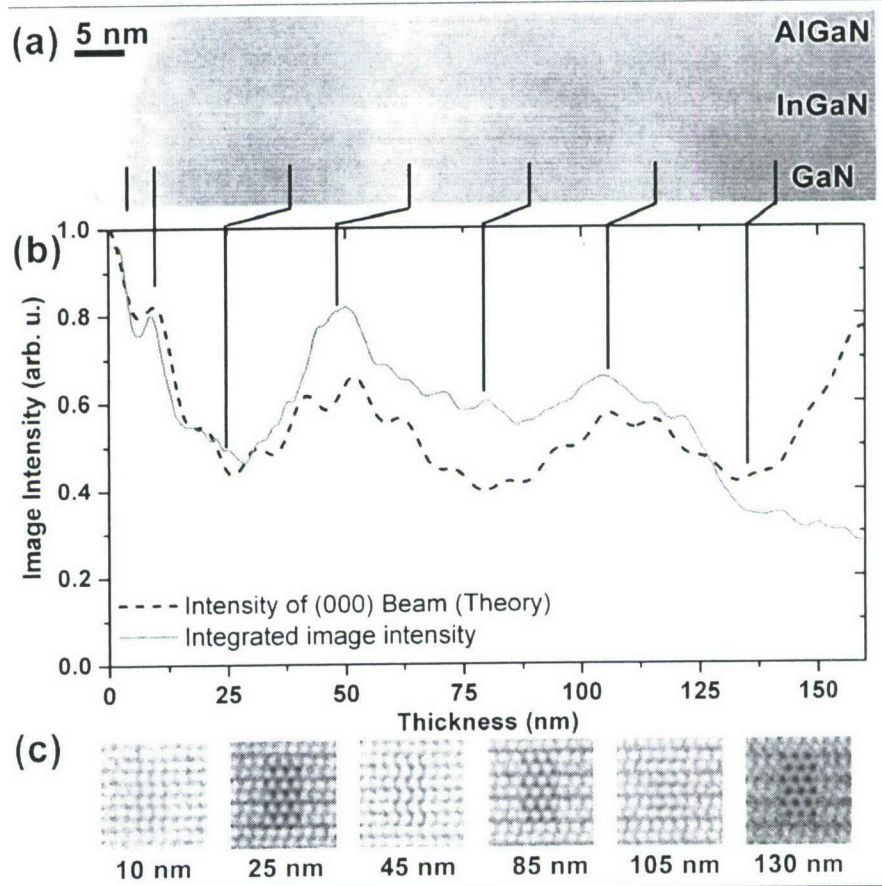


Figure 2.12: (a) Lattice image of the $\text{In}_x\text{Ga}_{1-x}\text{N}$ QW. (b) The averaged image intensity taken in the GaN substrate parallel to the QW was fitted to the calculated intensity of the (0000) beam (c) Overlay of image simulations (contrast was adjusted to the experiment).

The correct determination of the thickness is confirmed by comparing image simulations with the HRTEM image (Figure 2.12c). There is a discrepancy between experimental and simulated intensities, which is of unknown origin and commonly attributed to the Stobbs factor [Hyt94, Boo98, How04]. Further, the recording on a plate can add a non-linearity that is disregarded here.

At Scherzer focus in a high voltage microscope, the interference pattern of the micrograph is easily interpretable in terms of the crystallographic sample structure and the displacement field can be directly measured. Strain was measured both in the $\langle 0001 \rangle$

(out-of-plane) and $\langle 1\ \bar{1}00 \rangle$ (in-plane) directions across the QW over a distance of 70 nm. This corresponds to a thickness difference of 150 nm. The resulting out-of-plane strain map is shown in Figure 2.13c. The particular sample geometry and the wide field of view make it possible to observe the fully strained QW and strain relaxation in one single image.

Relaxation in thinner areas of the sample (left part of the image) is directly visible in the strain map as a widening of the strain profile. In the thicker parts of the sample (right part of image) a limit for reliable extraction of quantitative information is reached above a distance of 60 nm from the vacuum because the signal to noise ratio degenerates rapidly and contrast reversal occurs.

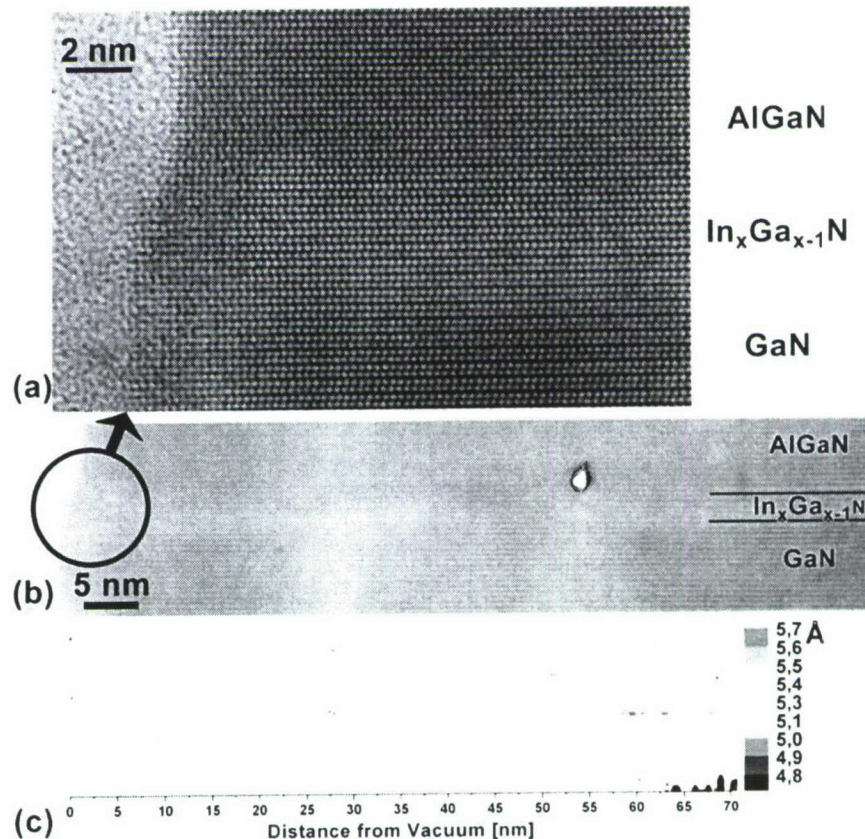


Figure 2.13: (a) shows a magnified view of the lattice image (b) illustrating that the contrast is homogenous across the In_xGa_{1-x}N QW and no beam damage is detectable. This allows for (c) strain mapping across 70 nm along the sample wedge (the out-of-plane lattice, 0001 is shown). Relaxation induced broadening of the QW is visible in thin areas.

The measurements access compositional changes with the chemically sensitive out-of-plane lattice parameter $\langle 0001 \rangle$ and strain relaxation effects by the in-plane lattice parameter $\langle 1\ \bar{1}00 \rangle$. Relaxation effects are studied first. Figure 2.14 shows the in-plane strain profiles obtained from the strain map of Figure 2.13c. Unit cells were averaged parallel to the QW, resulting in stripes with a resolution of $0.5 \times 5\ \text{nm}^2$. This reduces noise contributions to below 0.5 pm. Since the sample thickness changes across the wedge, this average includes a thickness change of roughly 10 nm. It is seen that relaxation occurs

below 30 nm of sample thickness through the increase of the in-plane lattice parameter in the QW.

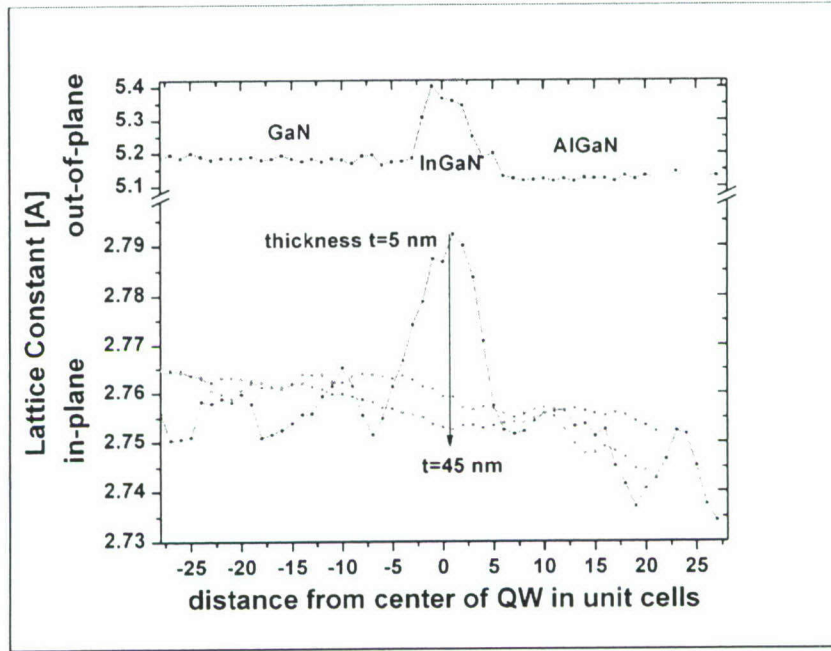


Figure 2.14: The in-plane (1 $\bar{1}00$) lattice parameter profiles are averaged over a thickness range of approximately 10 nm. Relaxation is present in the QW for $t < 30$ nm. The plot includes and averaged out-of-plane (0001) profile for reference. Gray squares identify areas used in Figure 2.16.

The extraction of the chemical composition profiles is easiest where relaxation is negligible. Previous theoretical studies derived that in a modulated structure of period L relaxation has to be taken into account at a thickness t when [Tre86, Che89, Chr94]

$$\frac{t}{10L} < 1. \quad (2.4)$$

In the studied sample $L = 3$ nm and indeed relaxation is observable for $t < 30$ nm. The relaxation criterion from Equation 2.4 can thus be used to avoid any relaxation effects. As mentioned, however, it is desirable to analyze thin samples and it is of importance to understand strain relaxation in wedge shaped samples quantitatively. Further, it is of essence to calibrate strain measurements and chemical composition and compare the result with computational predictions.

Because of the non-periodic structure of the sample, strain relaxation cannot be described analytically and finite element analysis (FEA) was chosen to model the sample. A mesh with nodes spaced according to $\langle 0001 \rangle$, $\langle 1 \bar{1}00 \rangle$ and $\langle 11 \bar{2}0 \rangle$ distances in GaN was generated using the freeware FEA program Mefisto [Per07]. Different thermal expansion coefficients corresponding to the normalized difference in lattice parameter of the alloys were defined for $\text{In}_x\text{Ga}_{1-x}\text{N}$ and $\text{Al}_y\text{Ga}_{1-y}\text{N}$ as done by Tillmann et al. [Til00]. To simulate rigid surroundings the displacements along the (0001) axis at the bottom of the GaN substrate and along the (1 $\bar{1}00$) axis on one side of the mesh were fixed at zero. Elastic

constants of the alloys were extrapolated from literature values for InN [She76], GaN [Pol96] and AlN [McN93] using Vegard's law. It should be noted that literature on elastic properties of nitrides is relatively scarce and that values scatter [Wri97b]. However the simulation did not change dramatically when varying the constants within 10% of the literature data.

In the next step, the mesh was heated from 0 K to 1 K and allowed to relax. To extract strain from the FEA simulations, the distances between the nodes corresponding to (0001) and (1 $\bar{1}$ 00) were calculated from the displacement data, and averaged in the same way as the experimental data. This is possible because in a high voltage microscope at Scherzer focus the lattice fringe image directly reflects the structure of the sample over a wide range of thicknesses. Differences due to bending of lattice planes or thickness effects can be neglected in such areas of strong contrast [Hyt01]. Even though nitrides are generally non-centro-symmetric, the wedge in the studied sample is vertical to the chemically sensitive out-of-plane lattice constant such that no measurement artifacts are expected here.

Figure 2.15a shows a three-dimensional FEA grid of $30 \times 30 \times 15$ unit cells modeling the studied GaN/In_{0.25}Ga_{0.75}N/Al_{0.3}Ga_{0.7}N heterostructure after relaxation. Taking advantage of the symmetry along the thickness of the sample this corresponds to a simulated sample area of $15.5 \times 8.3 \text{ nm}^2$ with a thickness of 5 nm. This slab does not reflect the true geometry of our sample since it severely underestimates the thickness of the sample. Additionally, the experimental data in Figure 2.14 shows how relaxation effects are present up to 15 unit cells from the QW center such that the grid should be enlarged. Figure 2.15b shows a computationally more feasible two-dimensional simulation of an extended area (125×70 unit cells) that is more representative of the strain mapped areas with the limitation that no relaxation in beam direction is possible. To a first approximation, this two dimensional grid can be thought of as the base of the 3D simulation (\square section of the sample).

The strain extracted from 2D and 3D simulations is compared in Figure 2.16a. There is a qualitative agreement between the two simulations. However the out-of-plane lattice constants are lower in the 3D simulation due to the added relaxation along the thickness of the sample. Additionally the parameters for Al_{0.3}Ga_{0.7}N show discrepancies, due to the limited size of the 3D slab. However, in In_{0.25}Ga_{0.75}N none of the discrepancies exceed 1 pm, which corresponds to the measurement precision. Thus, 2D simulations will be used to explain the experimental data. The simulations predict a relaxation behavior that is unexpected in the frame work of tetragonal distortion. In fact in thin areas located close to the sample edge all lattice constants in the QW increase. The result is a three dimensional buckle as pictured in Figure 2.15a. This effect has not been taken into account in previous studies that assumed the sample geometry to be infinite and of even thickness.

The experimental measurement was averaged over a 5×5 unit cell area of the strain map to reach an out-of-plane precision of about 1 pm. This corresponds to an area of $1.4 \times 2.6 \text{ nm}^2$ in a [11 $\bar{2}$ 0] zone axis of GaN. Figure 2.16b shows thickness profiles of the lattice constants measured parallel to and on the QW and at a distance of 20 unit cells (grey squares in Figure 2.14 indicate the areas data was averaged over). The results of the 2D simulations at the same location have been included as straight lines. Overall, the

simulation describes the experimental findings well if an indium concentrations of $x = 0.25$ and an aluminum concentration of $y = 0.3$ are chosen. Note that these simulations do not represent an absolute determination of the indium concentration at this point as the sample geometry is not accurately described. This issue will be addressed later. There is a discrepancy for the out-of-plane lattice at low thicknesses that is due to an indium cluster located at the very edge of the sample. Indeed, for a measurement at another location of the sample from a different micrograph, the behavior in $\text{In}_x\text{Ga}_{1-x}\text{N}$ is well described (the out-of-plane lattice of this measurement is included in Figure 2.16b).

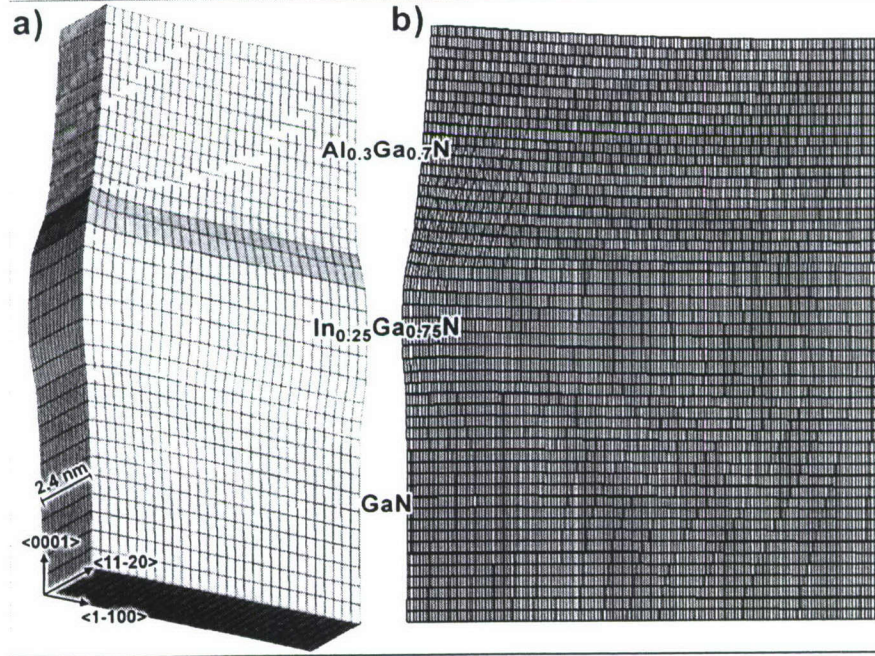


Figure 2.15: The FEA grid after relaxation in (a) 3D and (b) 2D showing buckling into the vacuum. For illustration purpose, displacements are exaggerated by a factor of five.

The in-plane lattice parameters start relaxing at thicknesses below 30 nm in accordance to the relaxation criteria (eq. 2.4). However, due to the 3D buckling, two competing effects influence the out-of-plane lattice constant: a reduced tetragonal distortion tends to shorten it, while a tensile component due to cap and buffer layer stretches it. Fortunately, these two effects cancel each other for distances from the sample edge that are greater than 5 nm. This is good news for strain measurement in HRTEM samples: the out-of-plane parameter, which carries the chemical information, remains constant for much longer than would be expected from tetragonal relaxation only. FEA analysis with QWs of different thicknesses yields the relaxation criterion for out-of-plane lattice constants in a wedged sample with the heterostructure parallel to the thickness gradient as

$$d < \frac{2}{3}L \quad (2.5)$$

where d is the distance from vacuum and L the thickness of the heterostructure. For typical QW thicknesses of $L = 2\text{-}4\text{ nm}$ out-of-plane relaxation occurs up to 3-6 nm from the sample edge. Further in, the out-of-plane lattice constant equals the value of biaxially

strained material of the thick sample limit. It is of particular interest to relate this strain state with the indium concentration x in the QW.

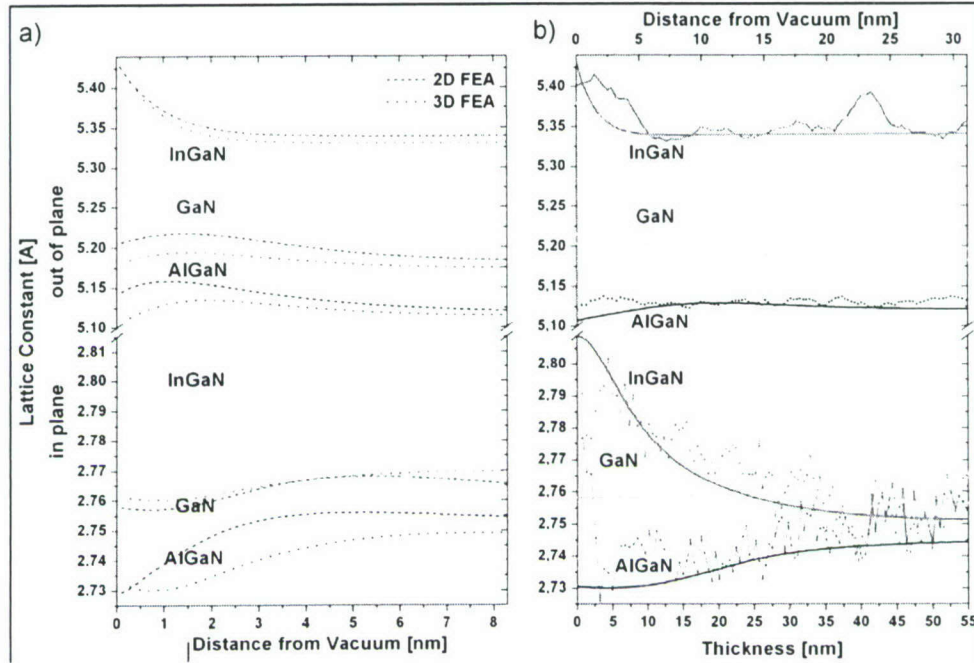


Figure 2.16: (a) Relaxation behavior as calculated from the 2D and 3D meshes in Figure 2.15. Agreement is particularly good in the $\text{In}_{0.25}\text{Ga}_{0.75}\text{N}$ layer. (b) The lattice parameters for the $\text{GaN}/\text{In}_x\text{Ga}_{1-x}\text{N}/\text{Al}_y\text{Ga}_{1-y}\text{N}$ structure are shown and compared to simulations extracted from the 2D mesh. An additional measurement for out-of-plane $\text{In}_x\text{Ga}_{1-x}\text{N}$ is included to demonstrate the effect of clustering in this material.

Figure 2.17 shows the concentration dependence of lattice constants measured in an $\text{In}_x\text{Ga}_{1-x}\text{N}$ multi QW structure with $0 < x < 0.25$. The chemical composition was established independently from Secondary Ion Mass Spectroscopy (SIMS) measurements as published in [Kis98a].

Additionally, FEA simulations for $\text{In}_x\text{Ga}_{1-x}\text{N}$ across the entire composition range were performed with confinement on two or four sides perpendicular to the [0001] plane to compute the strain in monoaxially and biaxially strained material. The results are included in Figure 2.17. For $x < 0.2$ the experimental data agrees well with the simulations of a biaxially strained layer. A linear fit across the data points with an ordinate crossing at 5.185 \AA (out-of-plane lattice parameter in GaN) yields the relationship for the out-of-plane lattice constant $c(x)$ in strained $\text{In}_x\text{Ga}_{1-x}\text{N}$

$$c(x) = 5.185 \text{ \AA} + \alpha * x \quad (2.6)$$

with $\alpha = 1.11 \text{ \AA}$. This formula is similar to Vegard's law but it calibrates the indium concentration in samples strained according to Equation 2.5.

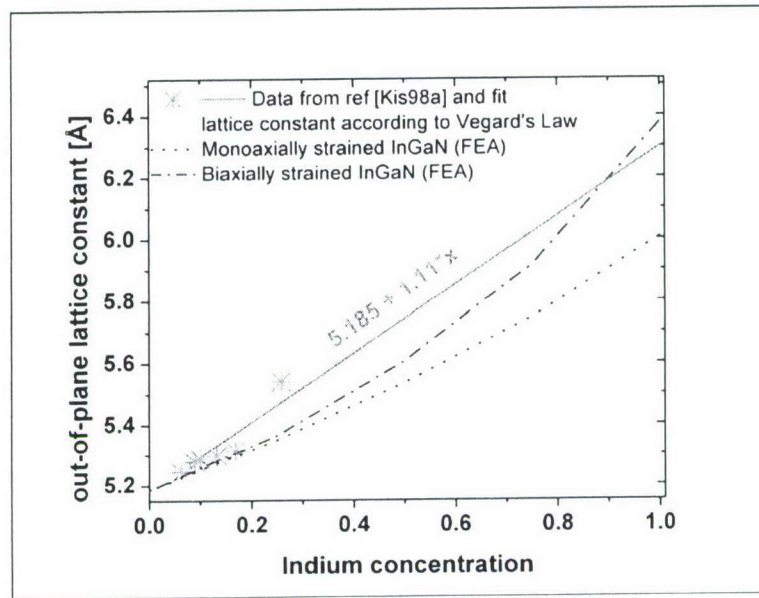


Figure 2.17: Experimental data is compared to the lattice constants calculated from FEA simulations. A linear fit gives the relationship of indium concentration against lattice constant in a QW satisfying Equation 2.4 or 2.5.

The accuracy with which strain relaxation can be modeled allows for a subtraction of relaxation effects from the experimental data and opens the possibility to compute the standard deviation in even the thinnest areas of the sample. Figure 2.18 shows the result of this operation for four adjacent measurements inside the QW and 28 unit cells away from it. The experimental standard deviation σ_{total} was calculated over 10 unit cells (2.6 nm) along the QW and is compared to σ_{alloy} computed for the given thicknesses. A dashed line through the three graphs signals noise as given in GaN.

It is seen that σ_{alloy} plotted in grey shade is not accessible with the present precision in $\text{Al}_{0.3}\text{Ga}_{0.7}\text{N}$. In $\text{In}_{0.24}\text{Ga}_{0.76}\text{N}$ however, the precision of the measurement is high enough to detect random alloy fluctuations for thicknesses below 20 nm, but contributions from clustering dominate σ_{total} in this alloy.

It is very challenging to discriminate the effects of random alloying against clustering, in particular for low indium concentrations $x < 0.2$. Only an analysis of detection levels and knowledge of the sample thickness allows reaching a conclusion. Even so, it cannot be excluded that the electron beam damages samples even if there is no visual trace of damage. However, the presence of spinodal decomposition has been demonstrated for larger x (Section 3.1) and it is expected that inhomogeneous indium distributions even occur for $x < 0.2$ as it is the case for indium in GaAs [Zhe94].

Novel experimental techniques will have to be developed to capture an element distribution in an early stage of precipitation in 3D that are currently being developed [Hum07, TEA]. In this context a statistical distribution of indium was suggested by atom probe measurements [Gal07] but even in this case detection limits will be of concern [Kis07a].

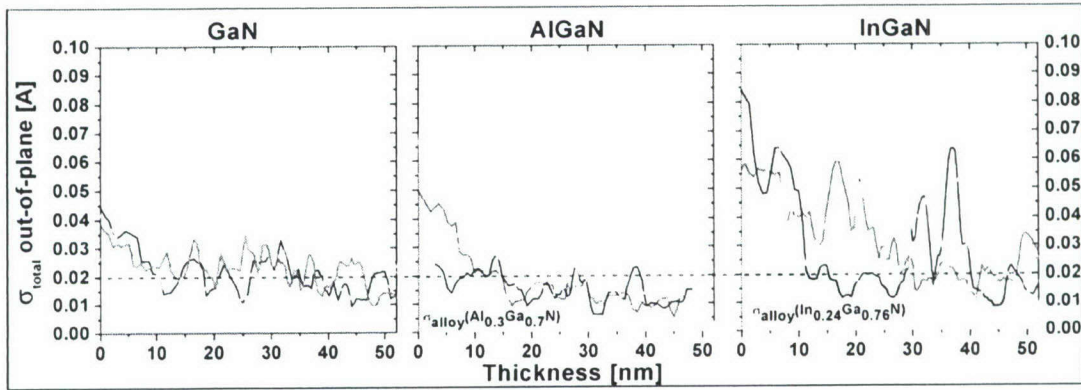


Figure 2.18: σ_{total} is plotted for the three materials after correction of relaxation by subtraction of the finite element simulations. The strain was averaged over 10 measurements. Σ_{alloy} was computed for the corresponding thicknesses and alloy concentrations.

The good agreement of strain measurements with the simulation of strain relaxation demonstrate how accurate quantitative HRTEM is. From this point, the question of the detection of clustering in $\text{In}_x\text{Ga}_{1-x}\text{N}$ and other materials becomes a matter of detection limits. It is thus of prime importance to evaluate sources of error and the precision before a conclusion about alloy (in)homogeneity is given.

2.3 Conclusion

This chapter addressed the challenges and opportunities that the measurement of displacement fields by HRTEM. Indeed HRTEM offers both the spatial resolution and sensitivity needed to analyze chemical (in)homogeneity in nanostructured samples. But its applicability was subject to doubt due to sample damage occurring during preparation and imaging.

The general conditions for reliable quantitative HRTEM can be summarized in three steps:

- Quantitative HRTEM places stringent conditions on the sample preparation: samples must be free of milling damage and have atomically flat surfaces. In the case of $\text{GaN}/\text{In}_x\text{Ga}_{1-x}\text{N}$ this can be realized by using the wet etching technique described in Section 1.6.
- A quantitative assessment of the limitations imposed by microscope instabilities such as focal change or other aberrations is necessary to establish confidence in the measurements. It is shown, that measurements in high voltage machines (acceleration voltage ≥ 800 kV) are most uncritical due to wide thickness/defocus windows with a stable image pattern. At lower voltages additional analysis is necessary to take machine instabilities into account. These include averaging over series of images or performing exit wave reconstruction.
- In all cases it is of prime importance to avoid beam damage. This can be avoided in adequately prepared samples if exposure times are kept below two minutes and beam current density is low (< 30 A/cm²).

Because of the small volumes sampled in HRTEM, random alloy fluctuations may be measured. It is thus important to differentiate them from true clustering by estimating the sample thickness and evaluating the fluctuation that would be expected in a random alloy. For $\text{In}_x\text{Ga}_{1-x}\text{N}$ quantum wells a precision of about 2 pm was reached at unit cell resolution and compared to the expected random alloy fluctuations. It is demonstrated, that quantitative HRTEM can be used to detect clustering in undamaged samples. Furthermore, the comparison with finite element simulations allows to empirically define a calibration relationship between the chemical concentration and displacement fields in $\text{In}_x\text{Ga}_{1-x}\text{N}$ quantum wells.

Now that the framework has been established in which quantitative HRTEM can be used as a reliable tool for the detection of clustering, this technique is applied to understand decomposition behavior of $\text{In}_x\text{Ga}_{1-x}\text{N}$.

3. Phase Separation, Clustering and Ordering in $\text{In}_x\text{Ga}_{1-x}\text{N}$

Indium gallium nitride (InGaN) has many device applications in opto-electronics thanks to its excellent optical performance. As a consequence, $\text{In}_x\text{Ga}_{1-x}\text{N}$ has been the subject of numerous investigations focusing on its optical and structural properties. Photoluminescence experiments proved most of the luminescence originates from bound exciton complexes [Kre02]. Early HRTEM investigations by Kisielowski et al. [Kis97] established, that indium could segregate locally to create indium rich clusters. These clusters were thought to be responsible for the localization of excitons in $\text{In}_x\text{Ga}_{1-x}\text{N}$ [Rut02, Seg04].

However, these investigations had to be revised as it became clear, that images of damaged samples could lead to the false detection of clustering [Sme03, Li05b, Sme06]. Very recently up to the existence of clustering in $\text{In}_x\text{Ga}_{1-x}\text{N}$ has been questioned [Gal07] and the localization was related to monolayer steps in the quantum well (QW) thickness. Decoration of V-defects was proposed as an explanation for the high radiant efficiency of $\text{In}_x\text{Ga}_{1-x}\text{N}$ despite high defect densities. QW thickness variations and screening of defects could explain some of the optical properties of $\text{In}_x\text{Ga}_{1-x}\text{N}$, but they could only be observed in a very limited selection of samples.

It is the goal of this chapter, to establish in a quantitative manner to what extent phase separation is present in $\text{In}_x\text{Ga}_{1-x}\text{N}$. In the first section, a short introduction about the theoretical prediction and experimental detection of phase separation and ordering in $\text{In}_x\text{Ga}_{1-x}\text{N}$ is given. Sections 3.2 and 3.3 present quantitative HRTEM measurements of clustering in QWs and bulk $\text{In}_x\text{Ga}_{1-x}\text{N}$. Finally the results are discussed and a conclusion with a recommendation for the growth of $\text{In}_x\text{Ga}_{1-x}\text{N}$ is given.

3.1 Phase Separation and Ordering

InN and GaN are difficult to alloy due to their large lattice mismatch of 11% ($a(\text{GaN})=3.19 \text{ \AA}$ and $a(\text{InN})=3.54 \text{ \AA}$ [Pic78, Shu97]). As a consequence $\text{In}_x\text{Ga}_{1-x}\text{N}$ layers grown on sapphire or GaN are highly strained. Additionally, the ideal growth temperatures for GaN and InN are very different: GaN is usually grown at temperatures of 800 - 1000°C while InN has to be grown at much lower temperatures ($\leq 500^\circ\text{C}$) to incorporate enough nitrogen to avoid the formation of metallic indium. It is thus difficult

to find a compromise between these two growth conditions and still produce high quality and chemically homogenous material.

Decomposition is sometimes observed in $\text{In}_x\text{Ga}_{1-x}\text{N}$ QWs for anything but low indium concentrations ($x < 0.1$). This decomposition is certainly due to the high strains in this alloy, but it is not quite settled, when this decomposition takes place and what is its principal mechanism. Three mechanisms can produce inhomogenous layers: island growth during epitaxial deposition, spinodal decomposition, or ordering into alternating layers of GaN and InN.

Island growth is a well known phenomenon in mismatched materials. In the so-called Stranski-Krastanov growth mode, the system tries to minimize both strain energy of the epilayer and its surface tension [Dar97]. This leads to the three dimensional growth of pyramid like structures. Indeed, such structures were observed in uncapped $\text{In}_x\text{Ga}_{1-x}\text{N}$ layers by atomic force microscopy [Dam99, Ade00]. However, the structures are not preserved in the finished heterostructure due to the high temperatures used to grow the GaN cap layer.

Under these circumstances the system could then undergo spinodal decomposition to minimize its free internal energy. This decomposition is mainly driven by the high lattice mismatch of InN and GaN. According to calculation by Stringfellow et al. the $\text{In}_x\text{Ga}_{1-x}\text{N}$ alloy is thermodynamically unstable for a wide range of concentrations for temperatures up to 1500K [Ho96]. Figure 3.1 shows the phase diagram for relaxed and strained $\text{In}_x\text{Ga}_{1-x}\text{N}$ as computed by Karpov [Kar98]. According to these calculations, strain should inhibit the decomposition of strained layers such as QWs of a few monolayers thickness and homogeneous layers should be thermodynamically stable for $x < 0.35$ at room temperature. The miscibility gap, in which spinodal decomposition is expected, is shifted to higher indium concentrations.

A system that finds itself in the miscibility gap is thermodynamically unstable and will undergo spinodal decomposition by forming two phases with alloy concentrations that lie on the spinodal line. According to the theory of spinodal decomposition developed by Cahn and Hilliard this leads to composition gradients causing sinusoidal concentration modulation of a characteristic wavelength to dominate [Cah58, Cah61]. Spinodal decomposition thus forms periodic zebra-stripe like structures.

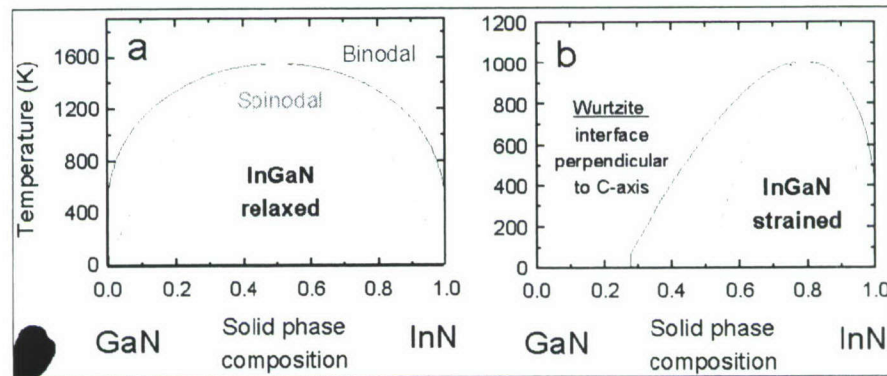


Figure 3.1: Phase diagram for (a) relaxed $\text{In}_x\text{Ga}_{1-x}\text{N}$ (b) strained $\text{In}_x\text{Ga}_{1-x}\text{N}$ according to Karpov [Kar98]

Such periodical structures of wavelength from 20 to 3 nm for concentration of $x = 0.12$ to $x = 0.34$ were reported in over 100 nm thick $\text{In}_x\text{Ga}_{1-x}\text{N}$ layers [Rao04, LW05, Wes01]. Ordering on the length scale of a few monolayers was also observed [Rut98, Beh99, Tel03]. This ordering was interpreted as alternating layers of GaN and InN. Overall, no concise image of decomposition in $\text{In}_x\text{Ga}_{1-x}\text{N}$ has emerged. The dependence on the indium fraction on the decomposition behavior of thick layers was studied by a few groups [Rob00, Nao06], but the mechanisms of decomposition could not be specified as no microscopic study was performed.

3.2 Decomposition in Quantum Wells

Early HRTEM investigations by Kisielowski et al. [Kis97] on $\text{In}_x\text{Ga}_{1-x}\text{N}$ QWs established that indium could be found to segregate locally and create indium rich clusters. Since then, and particularly in the framework of this work, a multitude of samples have been studied according to the guidelines outlined in Chapter 2.

In Figure 3.2 the $\text{In}_x\text{Ga}_{1-x}\text{N}$ data from Chapter 2 are processed such that the experimental noise σ_{noise} measured in regions of GaN is subtracted from the total standard deviation to obtain alloy related effects (open stars). The data set is complemented with quantitative analysis performed on MOCVD grown samples and commercial LEDs. The measurements were all performed at NCEM using a high voltage microscope operated at 800 kV and the OAM operated at 150 kV and 300 kV. For the OAM exit wave reconstruction or the averaging method described in Section 2.1.2 was used.

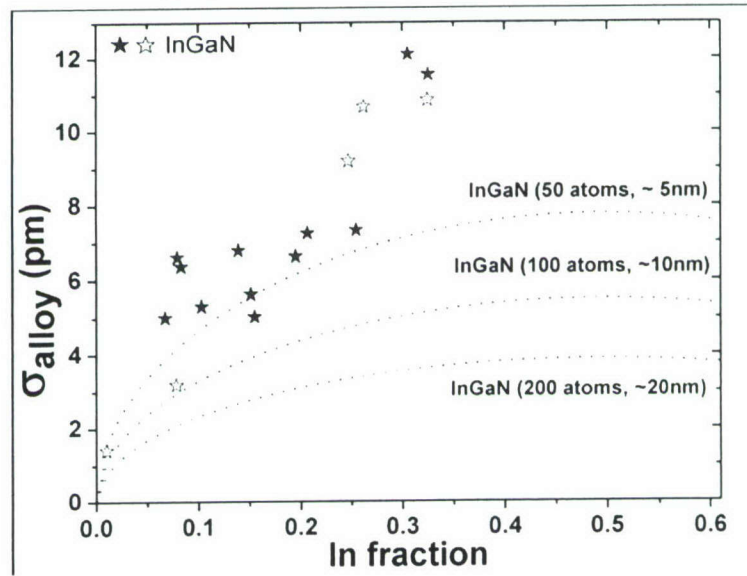


Figure 3.2: $\sigma_{\text{alloy}} = \sqrt{(\sigma_{\text{total}})^2 - (\sigma_{\text{noise}})^2}$ for $\text{In}_x\text{Ga}_{1-x}\text{N}$ was computed and complemented with more data points.

The experimental results scatter as expected because of uncertain sample thicknesses and different growth conditions. Overall, however, it is clear, that all methods produce comparable and repeatable results. This confirms that reliable quantification of clustering can be performed from lattice images recorded with electron energies between 150 and 800 kV. The expected effect of σ_{alloy} is plotted for different hypothetical sample

thicknesses in Figure 3.2. To describe the concentration dependence by random alloy fluctuations an average sample thickness of only 5 nm is required. Such a value is unreasonably small since the majority of the data is such that the samples are thick (20-30 nm) compared with the QW width (2-4 nm) in order to limit strain relaxation effects (see Section 2.2). If one assumes an average sample thickness of only 10 nm one would already find that cluster formation occurs for $x > 0.15$. For a reasonable sample thickness of 20 nm one finds that clusters are formed for $x > 0.1$ and that detection limits do not allow for statements concerning samples with $x < 0.1$. This establishes the existence of clusters in $\text{In}_x\text{Ga}_{1-x}\text{N}$ material for indium concentrations greater than 10%.

Now that the existence of clusters in $\text{In}_x\text{Ga}_{1-x}\text{N}$ has been established, the next step revolves around the question how those clusters are formed. Again, quantitative HRTEM can help to solve this question. However, while it was showed in this section how the decomposition depended quantitatively on the average indium concentration, the study of QWs in cross section geometry still suffers from two problems related to the measurement method: due to the finite sample thickness the signal is averaged a first time and the data has to be averaged a second time along the heterostructure such, that no meaningful determination about the size and shape of the clusters is possible.

Due to the averaging procedures no conclusive evidence for the presence of a spinodal decomposition can be given. Periodic indium fluctuations in QW structures would be indicative of this type of decomposition, but are only recorded occasionally and with little statistical confidence. Therefore, the quantitative analysis is extended to include thick $\text{In}_x\text{Ga}_{1-x}\text{N}$ layers where the detection of periodic structures is simplified.

3.3 Decomposition in Bulk Material

As decomposition is more pronounced for high indium concentrations, two indium rich samples were chosen. The samples were grown at Cornell University in a Varian GEN-II gas-source MBE equipped with a rf plasma source for generation of nitrogen radicals. A 150 nm, respectively 120 nm thick $\text{In}_x\text{Ga}_{1-x}\text{N}$ layer was grown on sapphire with a GaN buffer at a substrate temperature of 550°C [Lu00]. Sample A (GS1936), has a nominal indium content of 70%. Sample B (GS1582), was grown with an indium concentration of nominally 60%. Both samples were ion milled and wet etched with KOH according to the sample preparation techniques discussed in Section 1.6.

High Angle Annular Dark Field (HAADF) Z-contrast images from Sample A and B are shown in Figure 3.3. They were recorded with a TECNAI F20 and a TITAN microscope. The images show periodic contrast variations confirming that chemical decomposition is present in both samples. In sample A the composition fluctuations oscillate with a wavelength of about 2 nm, in sample B the wavelength is about 4 nm and the contrast is more pronounced. The fluctuations are oriented between the $\{0002\}$ and $\{1\bar{1}02\}$ lattice planes in a $[11\bar{2}0]$ projection of the sample. Similar composition fluctuations in $\text{In}_x\text{Ga}_{1-x}\text{N}$ samples grown on an AlN buffer were observed by Lilienthal-Weber et al. [LW05].

Figure 3.4 a and b show Scherzer images of sample A and B respectively. Through focus series were recorded on various locations of both samples and used for exit wave reconstruction (c and d). Figures 3.4 e and f show maps of the c-lattice strain in these layers extracted from the phase of the reconstructed exit waves. The periodic contrast oscillations that are seen in the lattice and HAADF images as strips are reflected in the

displacement maps. They mark areas of varying c-lattice parameters revealing the presence of compositional changes. Even within a particular stripe there are significant lattice parameter changes creating an indium rich island structure that is modulated by the wavelength of the stripes.

In thick layers, the conversion of displacement field into chemical composition is not given by Equation 2.6 because of its different strain state. It differs from heterostructures of the same average chemical composition because the straining GaN matrix is replaced by alloyed material. The decomposed layers now strain each other. Therefore, a tetragonal distortion that oscillates around a mean determined by the average indium content in the layer is expected. Possible residual strain is evaluated by counting dislocations at the GaN-buffer/ $\text{In}_x\text{Ga}_{1-x}\text{N}$ -layer interface and measuring the in-plane a-lattice parameter directly. Both methods show that the $\text{In}_x\text{Ga}_{1-x}\text{N}$ layers relax at a distance of a few monolayers from the interface to reach a steady state with an a-lattice parameter that corresponds to an indium concentration of $\sim 60\%$ as computed by Vegard's law, which is close to the expected nominal concentration.

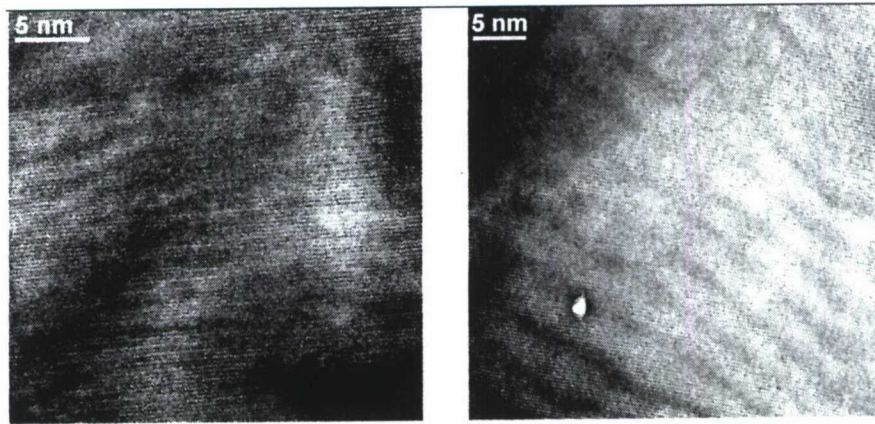


Figure 3.3: HAADF STEM Z-contrast micrographs of (left) sample A and (right) sample B. The contrast is chemically sensitive and shows stripes of indium rich material.

As thick $\text{In}_x\text{Ga}_{1-x}\text{N}$ layers are relaxed with respect to the substrate and all images were taken in thin (<20 nm) sample areas tetragonal distortion is thus reduced. It is assumed that stress is completely relaxed in such conditions and that c-lattice parameter variations can be directly interpreted as compositional changes using Vegard's law.

A composition profile was generated by averaging the indium concentration along a straight line that traces the strain maxima over a distance of 10 nm to 20 nm as indicated by the squares in Figures 3.4 e and f. Figure 3.5 shows the result of the averaging process for three different sample locations (offset for clarity). To extract the amplitude and fluctuations, the data were fitted with a sinusoid that nicely approximates the data. Results of the fitting process are listed in Table 3.1.

The decomposition wavelength in the samples varies between 2 and 4.5 nm, which is a distance that is well comparable with typical width of GaN/InGaN/GaN QWs [Wes01, Rao04, LW05]. Similarly, amplitudes of $\Delta x = 0.1$ and $\Delta x = 0.15$ compare well with the standard deviation σ_{alloy} of the c-lattice constant measured in QWs with an average concentration $x = 0.3$.

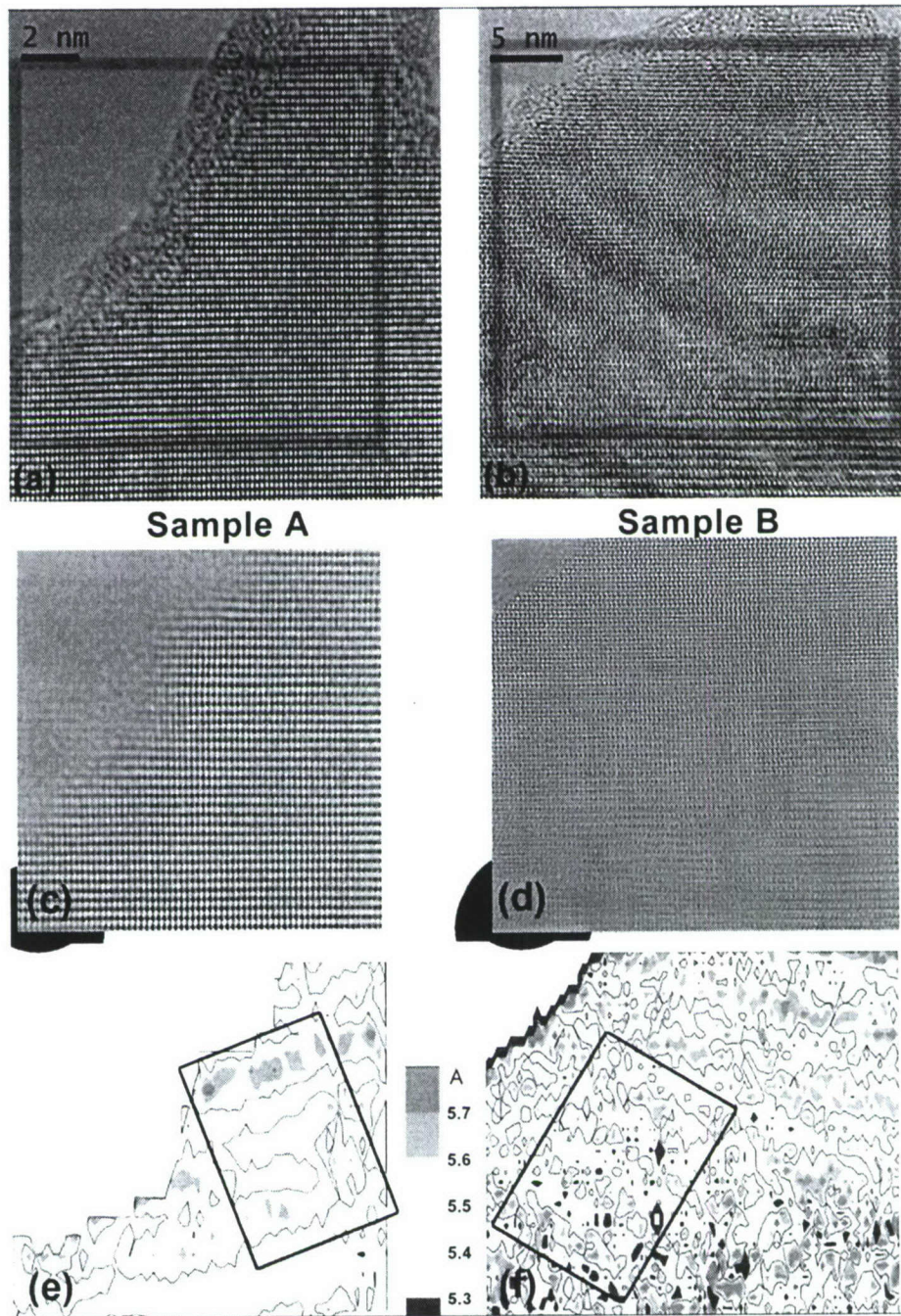


Figure 3.4: (a) and (b) HRTEM micrographs Scherzer defocus of sample A and B respectively and (c) and (d) the corresponding reconstructed exit wave. (e) and (f) are maps of lattice parameters measured on reconstructed exit waves of the areas shown. Squares indicate the areas where a composition profile was formed. Note the different length scale of the pictures.

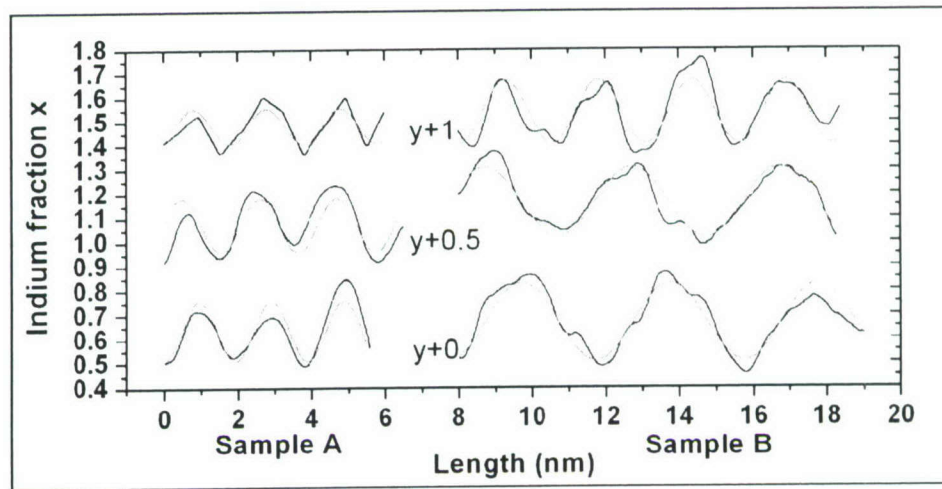


Figure 3.5: Concentration profile averaged along fluctuations on different areas in sample A and sample B. Concentrations are offset for clarity and fit with a sinusoid (red line).

Table 3.1: Wavelength, amplitude and average indium fraction extracted from the composition profiles in Figure 3.5. Errors describe the interval that includes all data points.

	Wavelength (nm)	Amplitude (Δx)	Average (\bar{x})
Sample A	2.02 \pm 0.1	0.1 \pm 0.03	0.56 \pm 0.08
Sample B	3.52 \pm 1	0.15 \pm 0.01	0.62 \pm 0.09

The stripes form a varying angle with respect to the growth direction $\langle 0001 \rangle$, ruling out their formation by a kinetic process during deposition of the epilayer. Moreover, the concentration profiles are symmetric, which emphasizes that a thermodynamical process is responsible for the decomposition of $\text{In}_x\text{Ga}_{1-x}\text{N}$. Indeed, heterostructures show an abrupt GaN/ $\text{In}_x\text{Ga}_{1-x}\text{N}$ interface as opposed to a smoother $\text{In}_x\text{Ga}_{1-x}\text{N}$ /GaN interface due to the tendency of indium atoms to float on GaN during growth (see Figure 2.9).

Following Cahn, a thermodynamically unstable system undergoing spinodal decomposition will amplify a sinusoidal fluctuation with a preferred wavelength [Cah58, Cah61]. Accordingly, $\text{In}_x\text{Ga}_{1-x}\text{N}$ samples grown deeper inside the miscibility gap should decompose with a shorter wavelength. Rao et al. observed this effect for indium concentrations of 12% through 34% by analyzing shoulders to diffraction spots in TEM diffraction patterns. They measured a decrease of wavelength from 20 nm to 3 nm [Rao04] in this concentration range, which agrees with the present findings.

At a given growth temperature the final decomposition amplitude is given by the two points at the spinodal. However, decomposition with nanometer wavelength is incompatible with a large amplitude because surface tension prohibits the formation of arbitrarily sharp interfaces. The thermodynamically stable state of systems with wavelengths that approach atomic dimensions might therefore differ significantly from those of macroscopic solids. Hyde et al. suggest that the continuity approximation in the Cahn-Hilliard model breaks down for nanometer scale fluctuations [Hyd96]. Further,

current models do not take into account kinetic diffusion barriers although experimental data show that the low mobility of indium atoms is a serious barrier to decomposition [Chu01]. Iliopoulos et al. [Ili06] demonstrated how low temperature growth of $\text{In}_x\text{Ga}_{1-x}\text{N}$ can suppress decomposition over a wide range of compositions. On the other hand, the formation of stripe like structures indicating decomposition was reported in thick MBE grown layers with low indium concentration ($x < 0.2$) [Li05a].

In summary, the decomposition behavior of thick $\text{In}_x\text{Ga}_{1-x}\text{N}$ layers strongly resembles that of a spinodal decomposed material. In $\text{In}_x\text{Ga}_{1-x}\text{N}$ spinodal decomposition produces structures on a nanoscopic length scale. However, the question remains whether the decomposition in bulk $\text{In}_x\text{Ga}_{1-x}\text{N}$ is due to the same process as in $\text{In}_x\text{Ga}_{1-x}\text{N}$ QWs.

3.4 The Decomposition Behavior of $\text{In}_x\text{Ga}_{1-x}\text{N}$ QWs and Thick Layers

In this section, the spinodal decomposition in thick $\text{In}_x\text{Ga}_{1-x}\text{N}$ layers is compared to the formation of indium rich clusters in $\text{In}_x\text{Ga}_{1-x}\text{N}$ QWs. The narrow width of QWs (2 nm – 4 nm) excludes the observation of periodic stripe patterns, which is the primary characteristic of the decomposition process in thick layers. However, it was described earlier in this report that the stripes shown in Figure 3.4 e and f themselves are inhomogeneous. They appear to be composed of aligned agglomerations of indium rich islands. In fact, these indium rich islands are strikingly similar to the dot-like structures observed in $\text{In}_x\text{Ga}_{1-x}\text{N}$ QWs.

Additionally, the decomposition amplitude in thick $\text{In}_x\text{Ga}_{1-x}\text{N}$ layers as recorded by XRD and luminescence by Robbins et al. [Rob00] shows similarity to Figure 3.2; in both cases the fluctuation amplitude increases with increasing x . However, data obtained from local strain measurements of QWs and from XRD experiments of thick layers are not directly comparable since different approximations are made while interpreting data. For example it is common to describe a broadening of XRD peaks with a Gaussian distribution, while our microscopic measurements reveal a fundamentally different element distribution. A comparative study is needed to establish proper relationships, which is beyond the scope of this work. In the framework of the presented results, the full width at half maximum (FWHM, in units of indium fraction) of the $\langle 0002 \rangle$ peak in the Θ - 2Θ XRD scan of sample A was compared with the amplitude of the sinusoid fit of the strain map. A resulting quotient $\text{SineAmp}/\text{FWHM} = 0.5$ was used to recalibrate the XRD data from literature. This scaling factor cannot be directly interpreted, as it represents a relationship between two different statistical distributions. Figure 3.6 plots the resulting fluctuation amplitudes against the average indium concentration. The data for the thick layers studied in the previous section adds decomposition results from material with $x = 0.6$ and $x = 0.7$ and narrows the location of center of the miscibility gap at indium concentrations around $x = 0.5$ to 0.6 in accordance with earlier experimental findings [Wu02b].

The data points for fluctuations in thick layers and QWs on the gallium rich side (squares and stars) agree remarkably well. As a guide to the eye, they were fitted with parabolas centered at the ordinate. The offset between the two datasets can be explained by data averaging during the profile creation, which does not take into account the existence of dots in the indium rich stripes. This would slightly increase the decomposition amplitude in thick $\text{In}_x\text{Ga}_{1-x}\text{N}$ layers and thus diminish the offset to fluctuation amplitudes in QWs.

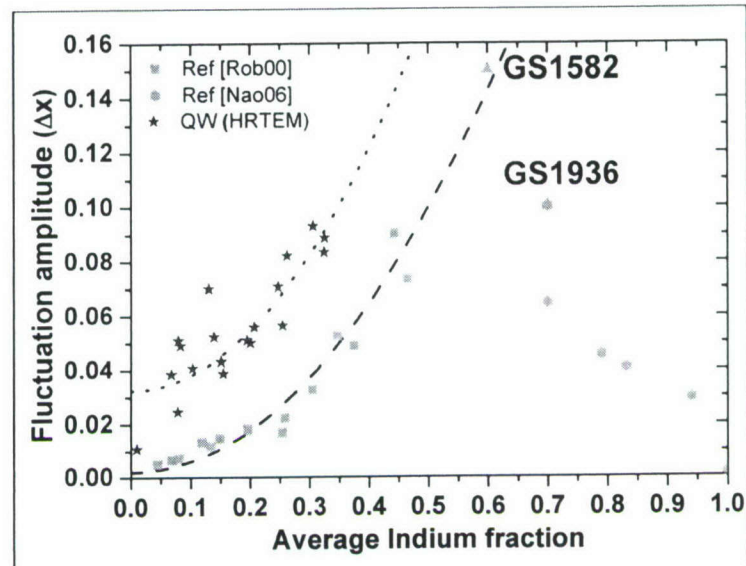


Figure 3.6: Chemical inhomogeneity of $\text{In}_x\text{Ga}_{1-x}\text{N}$ as a function of average indium concentration. Squares and hexagons represent bulk data from the literature to be compared to the values in QWs (stars). The dashed lines are parabolic fits to both data sets for $x < 0.5$.

It is argued that the formation of clusters in $\text{In}_x\text{Ga}_{1-x}\text{N}$ thick films and QWs is the result of a thermodynamic process, which may be modified by growth kinetics. This interpretation is corroborated by theoretical studies by Kenzler et al. which describes how spinodal decomposition in confined geometries results in structures very similar to the dots in $\text{In}_x\text{Ga}_{1-x}\text{N}$ QWs [Ken01] even though strain is not taken into account in his simulations. Figure 3.7 illustrates these points in a qualitative manner by comparing chemical decomposition fluctuations in a thick $\text{In}_x\text{Ga}_{1-x}\text{N}$ layer (Sample B, the map was rotated to align the stripes horizontally), an $\text{In}_x\text{Ga}_{1-x}\text{N}$ QW and the results from above mentioned simulations. Clearly the periodicity of the stripes in the thick layers is in the order of the typical QW thickness and the appearance of clusters in the stripes is optically very similar to clustering in QW. Finally, the fluctuations resemble those found by Kenzler et al. in an incomplete spinodal decomposition. Strain, which was predicted to suppress decomposition [Kar98], does not seem to have decisive influence.

Under these premises, indium clusters in $\text{In}_x\text{Ga}_{1-x}\text{N}$ QWs should show a periodicity similar to the one of the modulations in the bulk material. In cross section, this has not yet been observed due to a limited well width and the projection problem. The indium distribution at low $x < 0.1$ as well as the three dimensional atom distribution remain undetermined because of noise limitations and the lack of electron tomography with atomic resolution. Current developments address these limitations [TEA].

In this section it was demonstrated, that strain mapping can be a powerful tool to quantitatively determine the decomposition in thick $\text{In}_x\text{Ga}_{1-x}\text{N}$ layers. This allowed to compare the decomposition amplitude measured on a microscopic level with XRD measurements. Further, it allows the direct comparison of decomposition amplitude in $\text{In}_x\text{Ga}_{1-x}\text{N}$ thick layers and QWs. In both cases, the decomposition amplitudes follow a similar functional trend with increasing indium content. The periodicity of the decomposition in thick layers

is typical of spinodal decomposition and it is argued, that it is also such a thermodynamical process that governs decomposition in QWs.

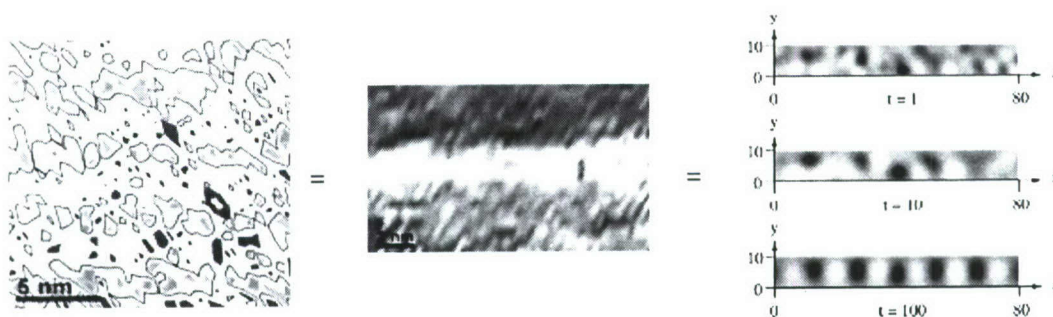


Figure 3.7: The strain map from sample B is juxtaposed to the strain map of an $\text{In}_x\text{Ga}_{1-x}\text{N}$ QW and a theoretical prediction of spinodal decomposition in a confined geometry for three different time steps (arbitrary time scale t) [Ken01].

3.5 Outlook and Consequences for Growth

In this section, the possibilities of future experiments as well as consequences of the results presented in this chapter for the growth of $\text{In}_x\text{Ga}_{1-x}\text{N}$ structures are explored.

3.5.1 Further Measurements

Due to the preparation in cross section geometry, the strain data recorded by HRTEM is always averaged along the thickness of the sample. Thus no meaningful assessment of the shape or periodicity of clustering in QWs can be given. However, this is of prime importance to model the decomposition and understand its effect on optical recombinations.

The averaging can be avoided by preparing the sample in plane view geometry, where the QW is perpendicular to the electron beam. The only averaging present then is through the QW thickness which can be neglected for typical thicknesses of a few nanometers. Sample preparation in this geometry is challenging because the sample should have a thin cap layer, ideally not more than 10 nm thick to ensure that the QW is indeed present in thin areas when thinning from the substrate side. As a consequence, the cap layer has to be protected against unwanted etching. The sample is thus thinned with conventional means (dimpling and ion milling) from the substrate side only. For wet etching, the sample is fixed in a plastic hose of 3 mm diameter (the size of the sample grid) with the cap layer facing into the hose. The hose is then filled with water to protect the cap layer from the etchants. Because of the high strain of the heterostructure, thin areas of the sample will bend as seen in Figure 3.8. Reaching a low index zone axis then becomes difficult.

Strain fields do not yield any chemical information as the heterostructure is homomorph to the substrate. Therefore, the in-plane lattice distance remains constant across the heterostructure while in plane view the c-lattice constant is not accessible to measurement since it is parallel to the electron beam. For this reason a different measurement technique has to be used to image chemical inhomogeneity. A VG HB501 dedicated STEM was

used to record HAADF images sensitive to changes in chemical composition. However, since the QW is only a few monolayers thick, the effect of a few indium atoms replacing gallium atoms is very small. It is thus challenging to differentiate chemical inhomogeneity from etch pits created during sample preparation.

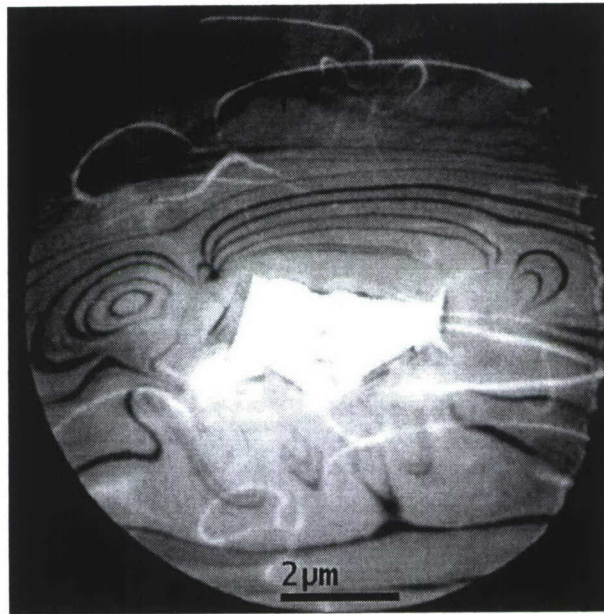


Figure 3.8: Ronchigram of the plane view $\text{In}_x\text{Ga}_{1-x}\text{N}$ SQW sample. The hole is in the center. The sample foil is bending over and is even torn in at the edges. Lines of contrast are caused by diffraction.

Figure 3.9 shows such an HAADF image with areas of contrast which could correspond to indium rich clusters. However this could also be the effect of changing sample thickness. Spectroscopic analysis of the energy losses encountered by the electron beam on spots of strong contrast and aside it did not show a significant difference. Acquisition of spectral data in a STEM is complicated by the high electron dose that rapidly burns holes into thin samples. Beam damage is thus a serious issue at this point. Spectroscopic STEM imaging or energy filtered TEM might lead to success here.

The ultimate goal of the microscopist is to determine the exact position of single atoms in a sample structure. To reach this goal, one needs to count atoms in a column and at the same time discriminate their chemical nature. The electron wave experiences a phase shift proportional to the total atomic weight in a column. In a pure material, this shift amounts to a multiple of the shift induced by one single atom of the column. The phase shift is discrete. In alloyed materials, a phase that does not correspond to this criteria is caused by an impurity atom and its chemical nature can be retrieved by analyzing its effect on the phase. Taking advantage of this discreteness of measurement values and of the discreteness of the crystalline grid (atoms are not randomly distributed in space) allows for unique tomographic reconstruction using only very few projected images [Jin04, Bat06].

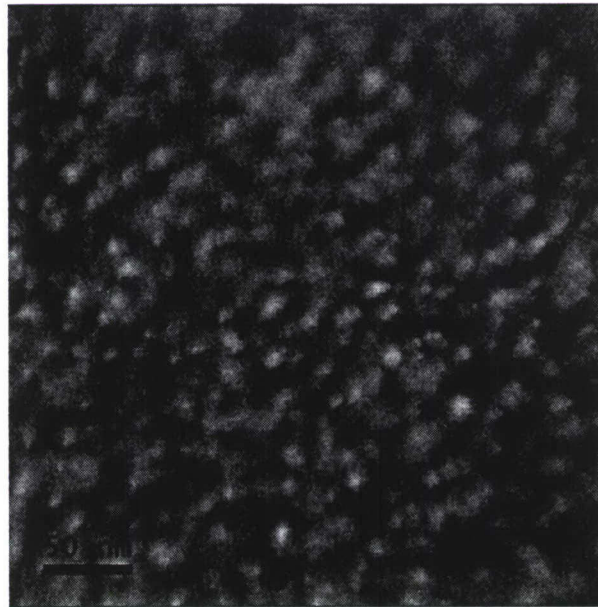


Figure 3.9: HAADF image of plane view In_xGa_{1-x}N QW sample. Scattering is Z number dependent, i.e. white blobs could be caused by indium rich clusters.

NCEM's TEAM project aims at realizing this vision by allowing sub-Ångström resolution at accelerating voltages as low as 80 kV. The low voltage allows the exposure of the sample to higher electron doses before the onset of beam damage. Correction of spherical and chromatic aberrations will enable imaging and exit wave reconstruction at unprecedented signal to noise ratio. It is a stated goal of the TEAM project to enable the study of nano-clusters and their formation. Exciting developments can thus be expected in the field of High Resolution TEM and STEM over the next few years.

3.5.2 Consequences for the Growth of In_xGa_{1-x}N

It was shown in this chapter, how indium clustering is detectable for indium concentrations above 10%. This is a direct consequence of the large lattice mismatch of GaN and InN that creates a miscibility gap for usual growth temperatures. An obvious solution for a controlled growth of In_xGa_{1-x}N with higher indium concentration would be to go to higher growth temperatures (~1000°C) where the miscibility gap narrows. To reach sufficient indium incorporation at these temperatures a high pressure (up to 100 bar) is needed. It is questionable whether decomposition can be suppressed during cooldown, but preliminary results seem promising [Ale06, Woo06].

In light of the presented results, another path that might lead to the realization of high indium concentration In_xGa_{1-x}N with a quality acceptable for technological applications is proposed. Instead of trying to suppress decomposition in In_xGa_{1-x}N QWs which promises little success in conventional low pressure reactors for concentrations above 10%, the approach is to seed decomposition fluctuation in the active layer during the growth process.

This seeding might provide a way of controlling and manipulating the decomposition in $\text{In}_x\text{Ga}_{1-x}\text{N}$ in a useful manner. In its experimental realization this signifies, that concentration modulations corresponding to the wavelength and amplitude of the naturally appearing phase separation should be grown into the active layer during epitaxy. This seeding will produce a layer that is already close to its thermodynamical optimum and should result in material of high quality. Conveniently, the decomposition wavelength is of the order of a few nanometers, which corresponds to the thickness of current QWs.

This approach has the additional advantage that strain in the layers is relaxed at the substrate interface and piezoelectric fields will thus be reduced. The active layer should be thick enough to decompose in a similar manner as the samples studied in this work but could probably be as thin as a dozen nanometers.

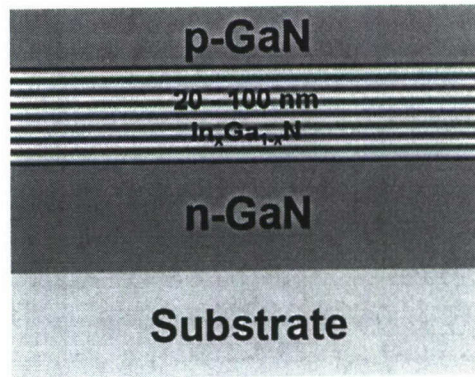


Figure 3.10: Proposed sample structure. The active region consists of a relatively thick $\text{In}_x\text{Ga}_{1-x}\text{N}$ layer with a high average indium concentration ($x \sim 0.5$). Engineered decomposition allows for high quality, high indium concentration heterostructures.

3.6 Conclusion

In this chapter, quantitative high-resolution transmission electron microscopy was used to study the distribution and clustering of indium atoms in $\text{In}_x\text{Ga}_{1-x}\text{N}$ alloys. In fully strained $\text{In}_x\text{Ga}_{1-x}\text{N}$ quantum wells, random alloy fluctuation could become measurable for indium concentrations $x > 0.1$ if samples are thin enough. However, it is found, that the formation of indium rich clusters dominates at these concentrations while noise limits measurements for $x < 0.1$.

A quantitative study of decomposition of $\text{In}_x\text{Ga}_{1-x}\text{N}$ thick layers was also presented. The measurement of displacement fields allows to analyze for the first time how the $\text{In}_x\text{Ga}_{1-x}\text{N}$ layers decompose to form a stripe like structure with 2 - 4 nm periodicity characteristic for spinodal decomposition. The stripes are oriented agglomerations of indium rich islands with striking similarity to the "dot-like" features observed in $\text{In}_x\text{Ga}_{1-x}\text{N}$ quantum wells.

Literature values for thick $\text{In}_x\text{Ga}_{1-x}\text{N}$ films and $\text{In}_x\text{Ga}_{1-x}\text{N}$ quantum wells could be directly compared and show identical functional dependencies of the decomposition amplitude. This provides strong evidence, that cluster formation in $\text{In}_x\text{Ga}_{1-x}\text{N}$ quantum wells can be explained by a thermodynamic process similar to spinodal decomposition in bulk $\text{In}_x\text{Ga}_{1-x}\text{N}$.

x N. Strain does not noticeably suppress decomposition. The center of the miscibility gap is placed around $x = 0.5$ to 0.6 .

4. Clustering in InN and the Bandgap Question

III-nitrides are generally considered as wide bandgap materials with applications in ultraviolet as well as visible-range optical devices and high power electronics. It is only recently, that measurements suggested a bandgap of InN below 1 eV [Wu02a, Wu02b, Dav02b, Dav02a] as opposed to 1.9 eV previously accepted in the literature. However, the structural imperfections and high background doping of InN can result in variation of the apparent bandgap through the Burstein-Moss shift, defect bands and plasmonic resonances. Publications of the last years placed the bandgap somewhere between 0.6 and 1.9 eV, depending on the employed measurement methods and the analyzed material [But05]. The reason for this wide range of estimates could be explained by defect bands and resonances inside a wide fundamental bandgap. Indeed, InN has to be grown at relatively low temperatures (around 500°C), which eases the formation of metal precipitates. In general, it is believed that metal clusters can be avoided in an optimized growth process, but nanoscopic inclusions might still exist below the detection limit of X-Ray Diffraction (XRD). It has been shown, that metal clusters could cause resonance in the infrared and effect the Photoluminescence (PL) behavior of InN [Shu04b, Shu06]. In this chapter, HRTEM studies of InN are presented. It is shown that inclusions of 5-40 nm can indeed be present in samples of apparent high quality as determined from XRD. These inclusions have a strong influence on the luminescence of the studied material.

4.1 Indium Clustering

Two hexagonal InN epilayers were studied by XRD, PL and HRTEM. The samples were grown by plasma-assisted molecular beam epitaxy on sapphire as described in [Iva04], at the Ioffe Institute, St. Petersburg, Russia, using the Compact 21T setup (France, Riber) equipped by a plasma source HD-25 from Oxford Applied Research. Sample rotation was suppressed leading to an inhomogeneous deposition. In particular, with an average substrate temperature of 480°C, there was a $\sim 20^\circ\text{C}$ positive temperature gradient from the center to the periphery of the wafer. This should result in an increasing size of metallic inclusions towards the border. Indeed, scanning electron microscopy revealed surface indium droplets at the periphery only. These droplets were etched with KOH before the TEM and PL investigation, sample A was taken from the center of the wafer, sample B from its edge.

The samples were prepared for TEM in cross-section geometry in $[110]$ and $[1\bar{1}0]$ zone axis by mechanical thinning and argon ion milling using a Fishione ion mill operated at 6 kV for milling and 2 kV for polishing. To further reduce surface roughness, the samples were polished in a Linda ion mill on a liquid nitrogen cooled stage using a 500 eV beam. HRTEM images of the samples were recorded on the OÅM operated at 300 kV and set to Scherzer defocus. After low energy ion milling both samples show uniform contrast over wide areas indicating a clean and flat surface. Only the hexagonal phase is detectable. However, nanometer size areas of contrast were seen as shown in Figure 4.1. This contrast is not due to electron beam damage, as the inclusions have been found in areas exposed to the beam less than 10 seconds at only 1 A/cm^2 .

On the contrary, contrast alteration appears only after a few minutes of beam exposure causing contrast of the inclusion to disappear (see the next section for a description of beam damage in InN). The inclusions have an extension of about 5-10 nm in sample A and 20-40 nm in sample B (Figure 4.1). The size increase is in accordance with the growth mode and the samples were prepared in an identical manner. Contrast imaged in the first seconds of illumination is thus due to inclusions that are already present inside the original material. The inclusions found are much smaller than any of the inclusions reported to date in InN [Shu06].

Figure 4.2 shows a high resolution image of an inclusion together with power spectra from the indicated areas. No additional spots can be seen in the power spectrum of the inclusion. However, the spots are broadened by strain, which indicates that the inclusion is contained in the matrix as opposed to sitting on the sample surface. According to the lattice parameters given in the Pearson Handbook [Vil91], the lattice of hexagonal InN and tetragonal indium have similar diffraction pattern if

$$\langle 001 \rangle \parallel \langle 01 \bar{1} \rangle \text{ and } \langle 2 \bar{1} 0 \rangle \parallel \langle 200 \rangle$$

resulting in a 5% and 9% lattice mismatch respectively. (Note that indium also appears in a cubic phase for nano-particles; see e.g. [Osh01]).

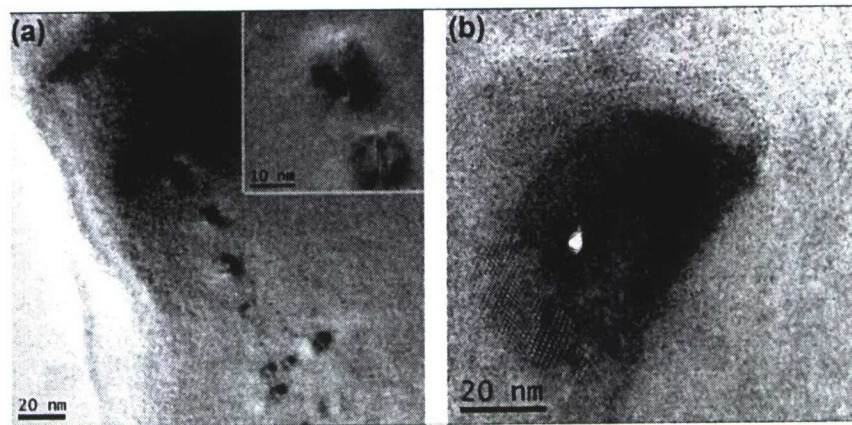


Figure 4.1: HRTEM images of (a) sample A showing inclusions of 5-10 nm in size. The inset shows a magnified image of an inclusion. (b) sample B showing inclusions of about 20 nm in size. Moiré pattern visible on the lower left side of the cluster are compatible with tetragonal metallic indium.

Figure 4.3 shows a calculated image at Scherzer defocus of an extended unit cell of InN [110] of 10 nm thickness containing a $4 \times 4 \times 4 \text{ nm}^3$ inclusion of tetragonal indium simulated with the program MacTempas [Kil07]. A darker contrast at the center corresponds to the indium inclusion. Fourier transforms were taken in a similar manner to Figure 4.2 showing that no additional diffraction spots may be observed if the inclusion is oriented along the matrix material. Simulations in $[1 \bar{1} 0]$ zone axis give identical results. However, the effects of lattice mismatch become noticeable in the larger inclusions through interference with the host lattice. Figure 4.1b shows such a Moiré pattern in the lower left corner. Simulations of superimposed layers of hexagonal InN and tetragonal indium with the mentioned orientation relationship do indeed predict Moiré pattern with a period of about 8 nm along the c-axis and down to a few nanometers when rotated. Metallic indium inclusions under strained conditions can explain the Moiré pattern. Their

period is too large to be observed in the small inclusions of sample A. Indeed, spectroscopic TEM studies of the samples confirmed the existence of indium in sample B [Kis07b] and placed the bandgap of defect free InN around 1.7 eV [Spe05].

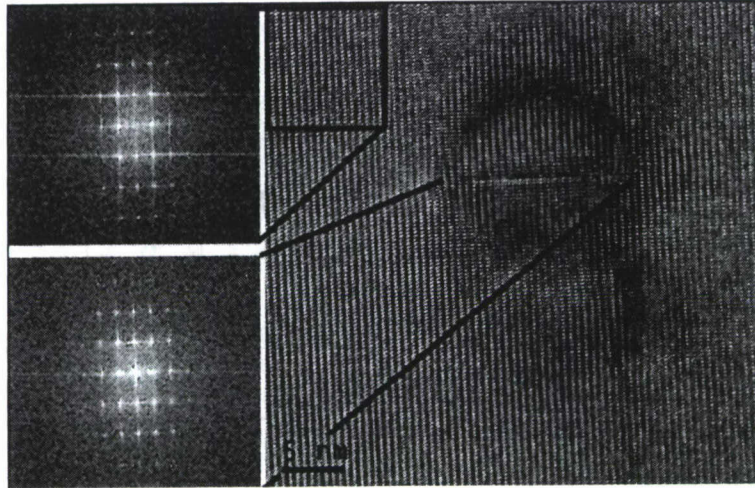


Figure 4.2: A high resolution lattice image of an inclusion in sample A. The power spectra of selected areas as indicated show no additional spots, but a widening caused by strain in the inclusion is observed.

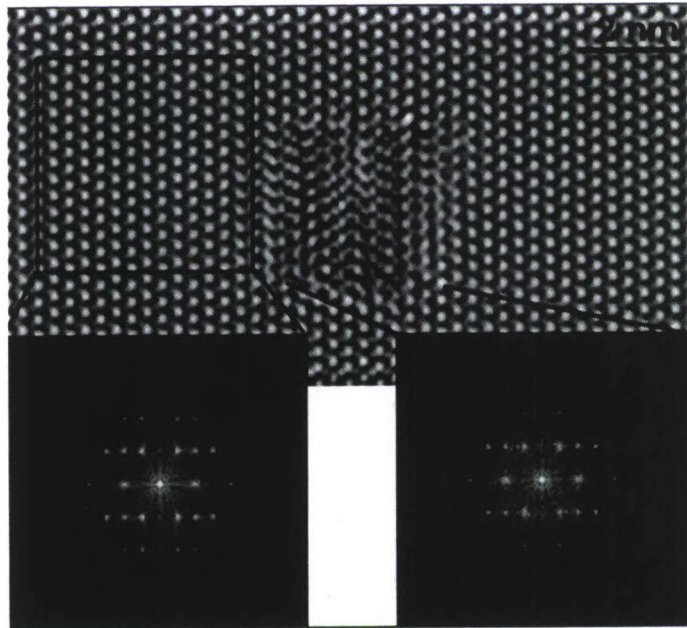


Figure 4.3: Simulated InN lattice image with a thickness of 10 nm containing an indium inclusion of $4 \times 4 \times 4 \text{ nm}^3$ in the center. The Fourier transforms do not show additional diffraction spots due to the inclusion.

Figure 4.4 shows the PL spectra of the two studied samples. The PL emission in sample A with its small clusters is centered at 0.6 eV and is about one order of magnitude weaker than in sample B centered at 0.68 eV. The spectra are similar to those observed before

cleaving the wafer holding sample A and B; a uniform Fermi level thus excludes a different Moss-Burstein shift. The modification of the PL spectra demonstrates a drastic effect of inclusions on the optical properties of InN. It can be understood when two basic phenomena which are possible in metallic indium inclusions are considered; the plasmonic (Mie) resonances and the specific interband absorption between the parallel bands in metallic indium [Har66]; the latter starts from 0.6-0.7 eV, reaching a maximum at 0.9 eV to 1.5 eV [Gol63]. The Mie resonance depends strongly on the aspect ratio of the inclusions. A high aspect ratio can shift the resonance into the infrared. However the HRTEM images do not indicate high aspect ratios. If the inclusions are presumed to be spherical, they would produce Mie resonances near 2.8-3 eV. Additionally, in small clusters (5 nm) the damping of the resonances by boundaries should be significant.

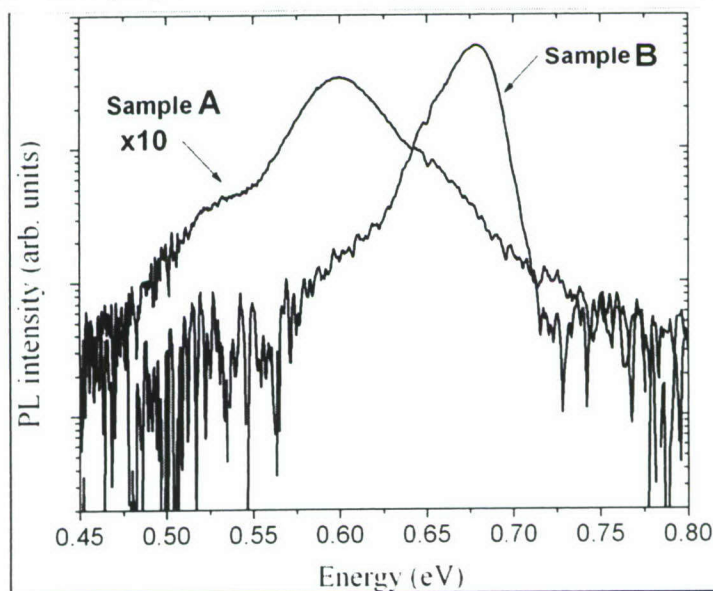


Figure 4.4: PL spectra measured in the samples A and B with indium clusters sizes of 5 and 20 nm, respectively. Excitation is done by a 809 nm line of a InGaAs laser, detection by a combination of InGaAs Hamamatsu and PbS detectors [Shu07].

Thus, it is assumed that the basic optical effect in the small clusters is the parallel band absorption. It has been previously demonstrated that such absorption can quench the infrared PL near 0.7 eV, while in the larger clusters some plasmon-induced enhancement of the emission is possible [Shu04b, Shu04a]. Even in almost spherical clusters, it can be due to the local increase of the electromagnetic field at sharp corners. Due to similar crystal parameters, it may be argued that the inclusions could contain a cubic phase InN. However, the contrast change stemming from these inclusions is weaker than from pure indium. More importantly, cubic InN is expected to have a lower bandgap than the hexagonal phase [Amb98]. Cubic InN clusters would thus act as localization centers for charge carriers. Sample A with smaller inclusions is then expected to have a higher energy shift of PL due to possible confinement; sample B should have a lower energy shift. This is in direct contradiction with the luminescence spectra shown in Figure 4.4. Another common precipitate in InN is In_2O_3 [Xu05] however, the oxide has been related to high bandgap transition in InN [But05] and cannot explain the different PL observed in the studied samples.

In conclusion, it was demonstrated nanometer-scale inclusions can be present in InN samples. Careful sample preparation produced damage free, flat surfaces where changes in contrast and Moiré pattern are explained by metallic indium clusters. Due to an increase in growth temperature, the size of the inclusions is about 5 nm in sample A and about 20 nm in sample B. Further, it is established that the variation in the cluster sizes is consistent with modification in infrared luminescence, induced mostly by specific interband absorption within the metallic indium. In summary, nanoscopic metallic indium inclusions cause significant changes in the optical properties of InN.

4.2 Electron Beam Damage in InN

Damage caused by the imaging electrons is always of concern in HRTEM imaging, in particular when probing for chemical inhomogeneity or clustering. In this section, the effect of electron exposure on InN and indium inclusions is presented. The effects of electron beam irradiation – of prime importance to differentiate inclusions present in the original material and those formed during sample preparations and imaging – are discussed.

It can indeed be challenging to prepare and image a sample in such a way, that no damage is present. Figure 4.5 shows the phase of the reconstructed exit wave of an interface between GaN and InN. The pattern in InN is disturbed and it is challenging to resolve the In-N dumbbells in this material. This indicates that InN is a material sensitive to beam irradiation that will be altered by the electron beam after only 2 minutes of irradiation.

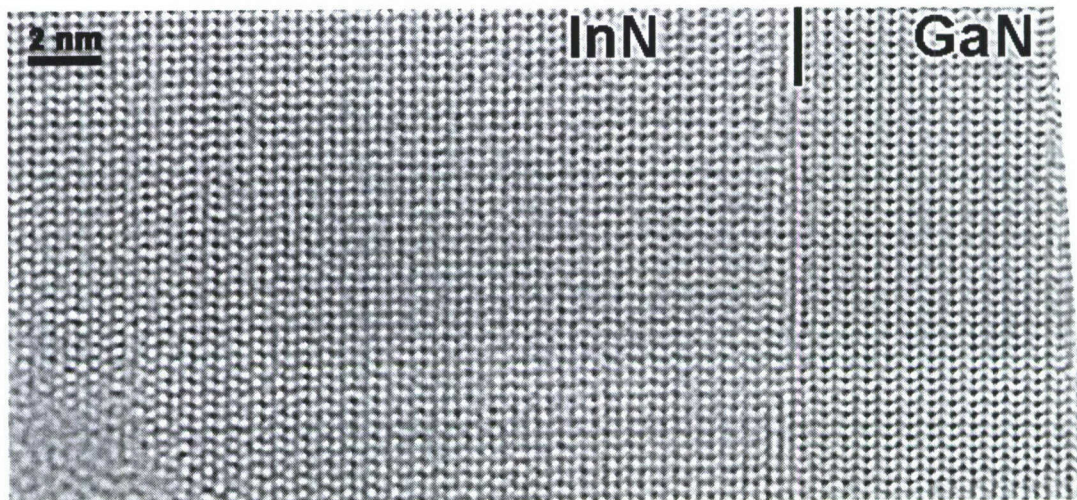


Figure 4.5: The reconstructed phase of a GaN/InN interface is shown. While the phase is constant in the GaN substrate, damage is visible in the InN.

Low energy ion milling of the samples produces uniform contrast over wide areas indicating a clean and smooth surface after short exposure times. Nanometer size areas of strong contrast were seen and could be attributed to metallic indium inclusion in the previous section.

Beam damage typically induces spots of contrast where material is amorphized or sputtered away (see for example Figure 2.1). In the studied samples however, such

damage was not observed even after exposure times above 5 minutes (Figure 4.6). Instead, the inclusions are first dissolved before longer time exposure leads to the formation of a pattern of stripes aligned along the c-plane.

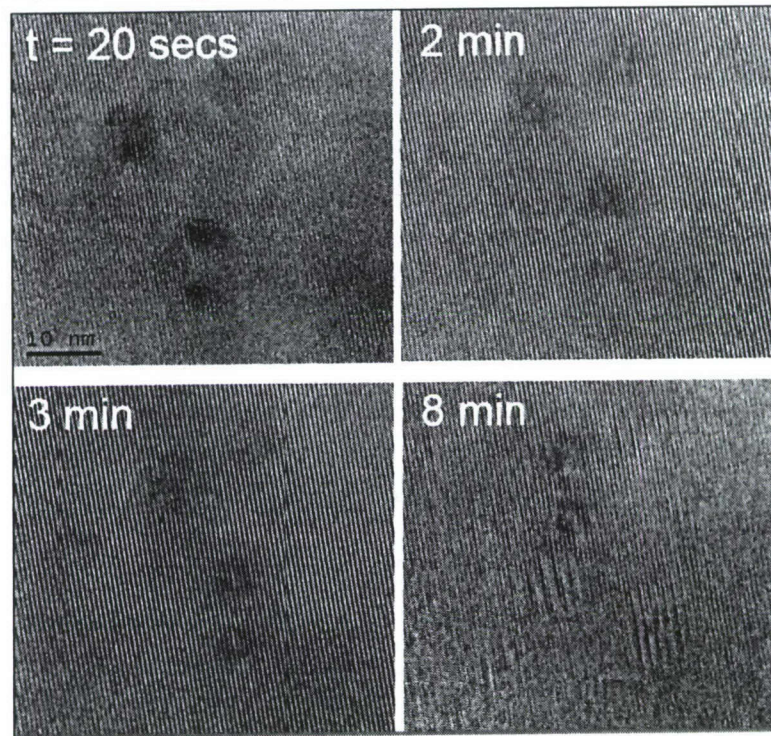


Figure 4.6: Time series of sample A showing inclusions that disappear after 3 min of low dose irradiation (1 A/cm^2). After 8 minutes of irradiation, the formation of a superlattice structure is observed.

Figure 4.8 shows the temporal evolution of a thin area of sample A taken at Scherzer defocus under relatively high beam currents (30 A/cm^2) to observe beam effects on a shortened time scale. The material is initially clean and homogenous over the field of view with an amorphous layer visible at the sample edge. After 5 minutes of irradiation, the amorphous layer shows signs of ordering and after 10 minutes a crystalline pattern corresponding to the $[110]$ zone axis of cubic or tetragonal phase is formed. Its hexagonal $\langle 111 \rangle$ axis is almost parallel to the $\langle 0002 \rangle$ direction of the hexagonal InN. The time series shows how electron beam irradiation of InN changes the crystal structure and actually “repairs” amorphized material into a different phase by recrystallization.

In thicker parts of the sample, such as the upper right corner in Figure 4.8, one can again observe the apparition of the periodic stripes. Figure 4.7 shows a reconstructed exit wave of such an irradiated sample area. As sketched, an A-B-A stacking pattern from the initial hexagonal phase is still present, but it alternates with an A-B-C pattern as expected for a cubic phase. The cubic phase can also be interpreted as stacking faults created during electron irradiation.

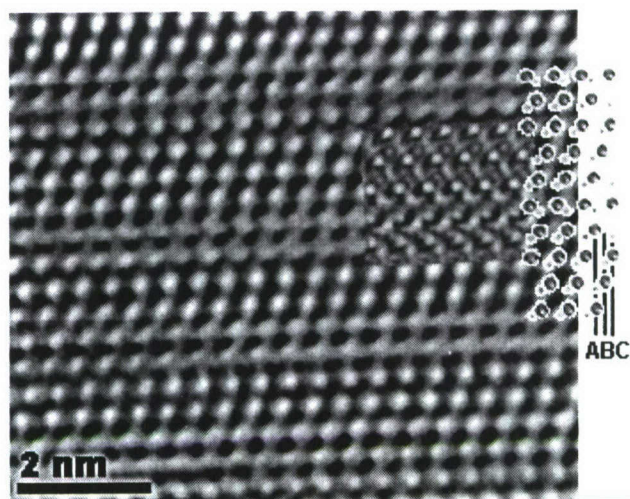


Figure 4.7: Phase of a reconstructed exit wave of irradiated InN. It shows the formation of a cubic phase alternating with the hexagonal phase.

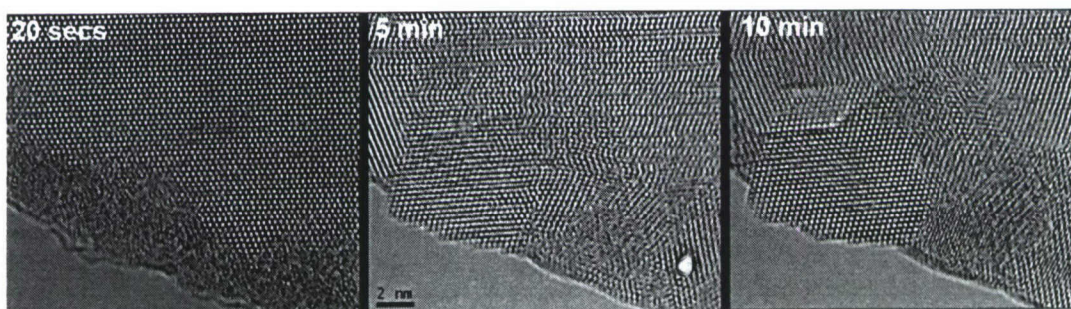


Figure 4.8: Time resolved Scherzer series of sample A showing the formation of c-InN. Beam current is 30 A/cm^2 and the times are taken from the moment of first irradiation.

Indeed, the pattern in Figure 4.7 could be explained with an extrinsic stacking fault introducing three “zinc blende layers”. However, the formation energy of an extrinsic stacking-fault is also about three times greater than for a type I stacking fault which were not observed [Wri97a, Sta98]. Additionally, the formation energy in InN is almost double that found in GaN, where no structural transformation was observed.

The formation of this pattern is fairly reproducible both in the apparition of the structure and in its periodicity. A very similar structure has been observed in the ternary alloy $\text{In}_x\text{Ga}_{1-x}\text{N}$. While $\text{In}_x\text{Ga}_{1-x}\text{N}$ shows phase separation dependent on the average indium concentration in the alloy as presented earlier in this work (Chapter 3), ordering with a wavelength around 1 nm lying in the (0002) planes was observed by TEM and interpreted as an ordered phase of high gallium or indium concentration [Beh99, Rut98]. As shown in the present samples, such structures could be beam induced and may not represent chemical ordering in the original material.

The beam sensitivity of the inclusions upon beam exposure and the crystallographic changes in InN are quite peculiar. Beam damage generally appears in the form of knock-on damage or through ionization. In nitrides, high energetic rays can ionize nitrogen atoms which then diffuse through the host crystal until they find another nitrogen radical

and combine to N_2 to leave the crystal. If there is no nitrogen radical in the vicinity, the atom is caught by the host crystal in its initial site or on an interstitial [Mkh03, Shr05].

In the present case, the nitrogen radicals can also be trapped inside the indium clusters and eventually the inclusions will contain as much nitrogen as the matrix, attenuating the contrast. Further damage is expected to lead to nitrogen desorption first, resulting in an indium rich phase. Two situations can result from this process: if nitrogen is completely desorbed, metallic indium would remain. Else, a cubic InN phase could be synthesized.

Indeed, the lattice constants of the cubic phase correspond to what is expected for cubic InN. InN is also known to preferentially crystallize into a cubic phase under indium rich conditions [Iwa06] like GaN [Okt99]. The dissolution of the indium inclusions shown in Figure 4.6 could be explained by a diffusion process into the matrix which would lead to an indium rich phase similar to the material at the sample edge in Figure 4.8. As a consequence, a cubic indium rich phase also forms in thick material. The high pressure rocksalt phase which would increase the density of InN by almost 20% [Uen94] could not be detected in the present samples. As the hexagonal symmetry is the energetically most favorable structure [Yeh92], it is quite improbable that the electron beam would eventually anneal the sample into a pure cubic phase.

The reason for the two phases to coexist in such close vicinity is inferred to be that their combination allows for inclusion of excess indium and is energetically favorable under strain. In conclusion, HRTEM imaging of InN was performed. The effect of electron beam damage was also discussed in particular because it causes both a phase transformation and a nano-structuration of InN. It creates a structure alternating between the original hexagonal phase and a newly created cubic phase. The cubic phase is believed to accommodate excess indium from the inclusions.

4.3 Conclusion

In conclusion, HRTEM imaging provided evidence for nanometer-scale inclusions in two InN samples. Careful sample preparation produced damage free, flat surfaces where changes in contrast and Moiré pattern are explained by metallic indium clusters. Due to an increase in growth temperature, the size of the inclusions is about 5 nm in sample A and about 20 nm in sample B. It is established that the variation in the cluster sizes is consistent with a modification in infrared luminescence, induced mostly by specific interband absorption within the metallic indium. In summary, nanoscopic metallic indium inclusions can be present in InN and cause a significant change in optical properties.

5. Optical characterization of InN

The development of monochromator technology for transmission electron microscopes now allows for a series of new experiments with semiconductor materials including locally measuring bandgap energies and defect bands with valence electron energy loss spectroscopy (VEELS). For the InGaN alloy system the technique was tested, local composition fluctuations were examined, different crystallographic phases were measured and defect bands were found located along an InN / GaN interface. InN epilayers from various suppliers were compared and optical energies from photoluminescence and optical absorption measurements were taken to complete the material

characterization and distinguish results from local (VEELS) and spatially averaged (PL, opt. absorption) techniques. The results for InN are described in this chapter.

5.1 Polymorphy in InN and the first VEELS bandgap measurements

The choice of experiment for the determination of band transitions in InN epilayers is scanning transmission electron microscopy (STEM). Epilayers were imaged in a 200 keV FEI TECNAI G² microscope with a monochromated nanoprobe beam which allows for a local investigation with an electron beam of 2 nm diameter and an energy resolution better than 200 meV (measured in vacuum). This microscope is located at the National Center for Electron Microscopy at the Lawrence Berkeley National Laboratory, CA. Band transitions in InN were measured by valence electron energy loss spectroscopy (VEELS) and compared to band transitions in hexagonal GaN, that is used as a standard for comparison.

The InN epilayers were deposited onto a (0001) GaN buffer, grown by Metal-Organic Chemical Vapor Deposition on (0001) sapphire. A typical InN epilayer thickness is 800 nm to 1000 nm, and the deposition was done under In-rich flux conditions. Further details of the epilayer growth are published in ref. [Spe04]. The epilayers' oxygen concentration is high, about 10²⁰/cm³. Any oxide phases can clearly be distinguished from the InN matrix in the TEM analysis and are not included in this study. The oxygen distribution in the InN epilayers is published in ref. [Xu05].

X-ray diffraction analysis was performed in a Siemens diffractometer with a 4-Ge-crystal monochromator. Lattice constants were determined from interplanar distances. Those crystallographic plane distances were extrapolated from [0002], [0004], [0006] and [10-12], [20-24] normal coupled scans utilizing the following equation [Har01]:

$$c_h = c_{\text{real}} \times (1 - D/L \times p_h) \quad (1)$$

with: $p_h = \cos^2(\Theta) / \sin(\Theta)$
 $c_h = h \lambda / (2 \sin(\Theta))$

D: sample deviation from eucentric height, L: sample distance to radiation source, h = 2,4,6 for [00h] reflections, c_{real}: extrapolated interplanar distance

TEM samples were prepared in cross-sectional geometry by Ar ion milling and – in some cases – a final etching step to minimize surface roughness [Kis97]. The VEELS measurements were performed with a monochromated FEI Tecnai G² STEM/TEM as described above. GaN buffer layers were investigated to provide a reference signal that was extensively studied before (see for example [Laz03, Kea02]). VEELS measurements were accompanied by high resolution transmission electron microscopy to determine the crystal structure of the epilayers and to identify other phases if present. VEELS spectra were only taken from areas identified as wurtzite InN, zincblende InN or wurtzite GaN, with no other crystal phases, especially no oxides or indium metal clusters, present.

A large deviation of the c lattice constant was observed earlier in InN epilayers grown on MOCVD GaN buffers [Spe04]. The corresponding strain in the epilayer was mainly attributed to a uniaxial stress as it occurs when defects are incorporated site specifically along (0001) crystallographic planes. Figure 5.1 shows the high-resolution x-ray diffraction of (0002) and (0004) reflections of InN (rocking curves) which clearly show a second peak appearing in the overall asymmetric diffraction peak. The second peak was

found to correlate with (111)-type crystallographic planes of the zincblende phase of InN. The corresponding lattice parameters from the complete x-ray diffraction analysis are given in Table 5.1. For details on the lattice parameter evaluation see ref. [Spe04]. It shall be noted that the presence of polytypes of InN does not explain the observed uniaxial stress response in the epilayer. Preferential incorporation of point defects along (0001) or (111) planes may have caused the strain in both crystallographic phases, wurtzite and zincblende InN, respectively, preferentially incorporated oxide platelets were not found.

Table 5.1: Lattice constant evaluation for wurtzite InN with zincblende phase inclusions

	theoretical [8]	single peak	double peak	mismatch [%]
a_wurtzite [nm]	0.3545	0.3534	0.3535	0.31 / 0.28
c_wurtzite [nm]	0.5703	0.5804	0.5799	1.77 / 1.68
a_zincblende [nm]	0.498		0.5035	1.10

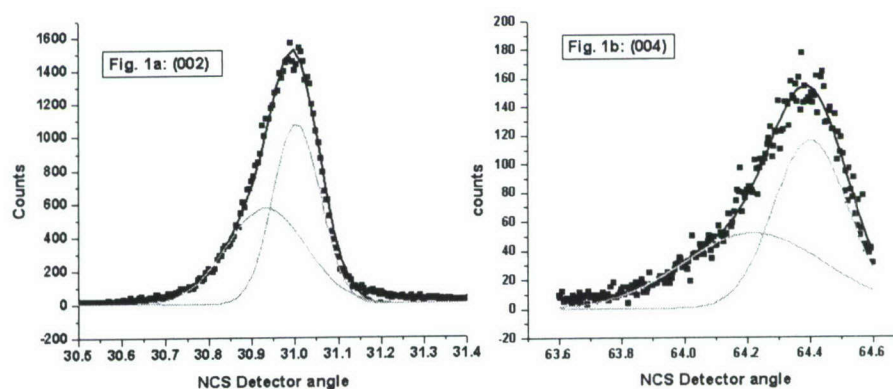


Fig. 5.1 X-ray normal coupled scan of InN epilayer deposited on MOCVD GaN buffer, the solid lines are fitted Gaussian functions (gray: single peaks, black: superposition of two peaks)

In a transmission electron microscope the polytypes of InN were confirmed. In thin TEM sample areas those phases can be investigated separately. Figure 5.2 shows such an area with wurtzite and zincblende InN. Power spectra taken from local image areas allow for their identification as shown by the insets. The local VEELS measurements were performed after identification of the respective phase of the investigated grains.

Valence electron energy loss spectroscopy, also called “low-loss EELS”, is an established method to measure band transitions in a variety of materials. First, high band gap materials such as BN, MgO or diamond were subject of VEELS investigations but also the band transitions of semiconductors such as GaAs were measured [Raf98]. Recently, the development of monochromated electron beams, which narrow the zero loss, became available. This advanced technology provides an energy resolution smaller than 200 meV and therefore gives access to measuring narrow gap semiconductors as well. For wurtzite

phase InGaN alloys, including InN various VEELS measurements were published recently [Laz03, Kea02, Bro02, Spe05, Jin05].

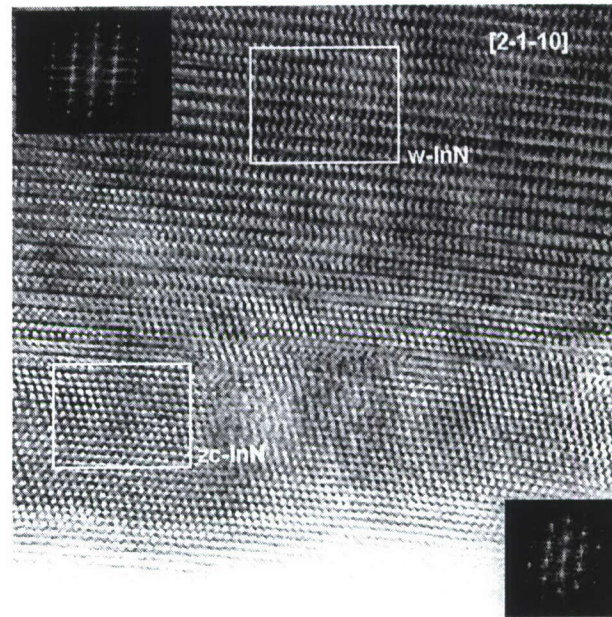


Fig. 5.2 High resolution transmission electron microscopy image of an InN epilayer with zincblende and wurtzite type areas, insets show the corresponding diffraction patterns of wurtzite and zincblende InN.



Fig. 5.3 Typical VEELS spectra of wurtzite GaN (dotted line), wurtzite InN (dashed line) and zincblende InN (solid line), the background is removed, (a) onset of first observed energy loss shows the bandgap of the respective materials, (b) plasmon peaks are observed at 19.5 eV for GaN, 15.7 eV for InN, the latter peak energy is identical for wurtzite and zincblende phases.

Figure 5.3 shows typical VEELS spectra of a GaN buffer layer (dotted line), a wurtzite InN area (dashed line) and a zincblende InN area (solid line). The VEELS spectra are shown with the background removed (no zero loss). At higher energies of the spectra (Fig. 5.3b) the plasmon peak can be observed which is characteristic for the host material, at (19.5 ± 0.1) eV for GaN and (15.7 ± 0.1) eV for InN, and at the same position for wurtzite and zincblende InN. The plasmon peak position also confirms that InN is measured and not another crystallographic phase such as indium-oxide. As can be clearly seen (Fig. 5.3a) no significant energy loss is observed below 1eV; the first band transition in GaN is found at about 3.3 eV while the first band transition in wurtzite InN is observed at about 1.8 eV. In zincblende InN the first band transition is found at about 1.5 eV (all figure 5.3a). The observation of a slightly lower bandgap for zincblende InN than for wurtzite InN is consistent with bandgap measurements of the polytypes in GaN and AlN (see for example ref. [Vur03]). The bandgap energy determined by VEELS is a room temperature value due to a slight local temperature increase in the TEM specimen (see also ref.s [Spe05, Jin05]). The bandgap value for GaN agrees well with literature data (see for example ref. [Vur03]).

The band transitions in zincblende InN were investigated at several areas of the TEM samples. Figure 5.4 shows the first derivative of typical VEELS spectra for zincblende InN, the original spectra are given in the inset of Fig. 5.4. The first derivative of the processed signal can be described by a superposition of Lorentz functions (smooth curves in Fig. 5.4) within the experimental noise. This fitting procedure was utilized to characterize the various band transitions by their inflection points as suggested previously by Lazar et al [Laz03]. We prefer this description over the commonly used bandgap determination by a power law $(E - E_g)^{0.5}$, see for example ref. [Kea02], that is more suitable if no signal overlap occurs. Using the FWHM of the respective peaks in the derivative plot one can link both methods, inflection point (IP) and power law (PL), and determine the bandgap E_g to [Spe05]:

$$E_g = E_{PL} \approx E_{IP} - 0.5 \times \text{FWHM} \quad (2)$$

Band transition values given in this chapter include this correction or refer directly to E_{PL} .

In figure 5.4 it is clearly visible that the first strong peak in the derivative energy spectra ($\Delta I/\Delta E$ versus E) is located at an energy of about 1.6 eV. All recorded VEELS spectra for zincblende InN have similar features than the two shown in figures 5.3 and 5.4. This corresponds to a corrected (room temperature) bandgap energy of (1.4 ± 0.2) eV. Also, a multitude of different spectra were taken from various areas of different InN epilayers, for wurtzite InN the bandgap energy was always similar to the one shown in Fig. 5.3 and was determined to (1.7 ± 0.2) eV [Spe05]. A variation of the bandgap energy was never observed, neither for epilayers with vastly different conductivity – absorption edge energies vary in those epilayers from 0.8 eV to 1.5 eV – nor for TEM specimen areas with different thicknesses as would be expected if the VEELS measurements were dominated by the epilayer's surface conditions. In zincblende InN higher energy band transitions are still to be determined, only a rather broad second peak around (4.2 ± 0.8) eV was found, which is likely composed of various band transitions. Those transitions will have to be investigated in more detail in future when epilayers of higher crystalline quality are available (less noise in the VEELS spectra).

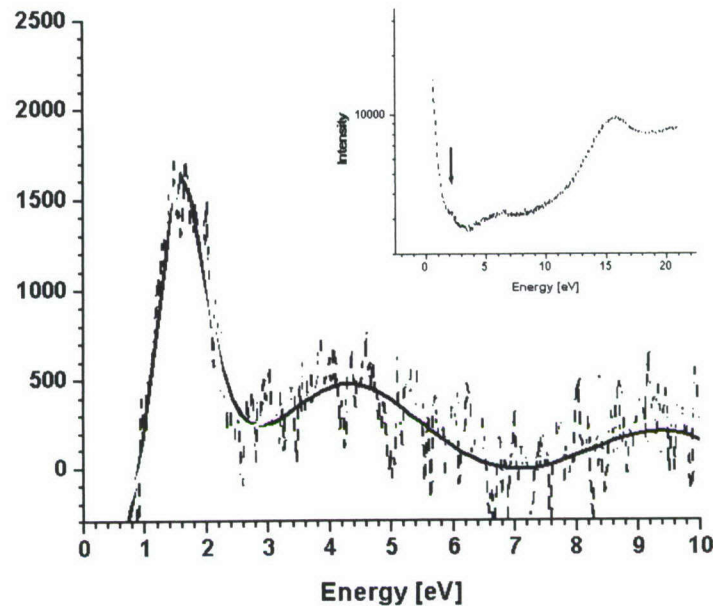


Fig. 5.4: First derivatives of the electron energy loss spectra of zincblende InN, the inset shows the original spectra.

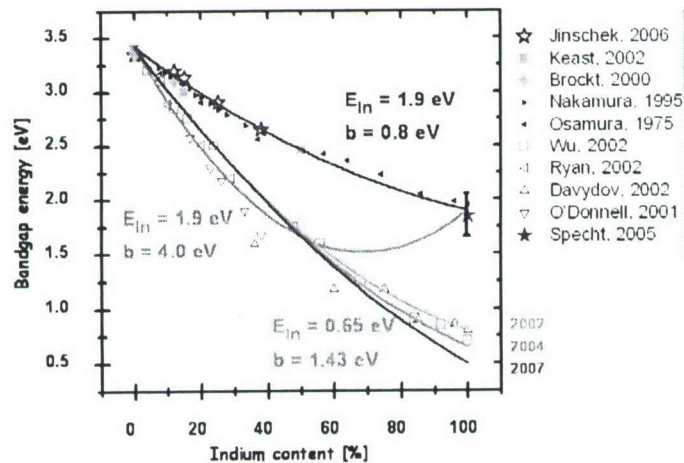


Fig. 5.5: Selected bandgap energy measurements for the InGaN alloy system (see also ref. [Jin05]). Recent VEELS results are marked in blue or filled grey symbols. Band bowing parameters are also given, the green curve shows how newer results for Ga-rich $\text{In}_x\text{Ga}_{1-x}\text{N}$ were combined with data from older InN experiments. Since 2002 the fundamental bandgap of InN was frequently changed to always lower values (pink, red, purple curves).

The currently available obtained VEELS bandgap energies for $\text{In}_x\text{Ga}_{1-x}\text{N}$, $x > 0$, are all in clear discrepancy to the recently published data obtained by photo-luminescence and optical absorption [Dav02a, Wu02a, Rya02, Odo01]. However, earlier publications [Nak95, Osa75] correlate well with the VEELS results. Figure 5.5 gives a summary of various prior published bandgap data, VEELS data are given in blue or filled grey

symbols, all other symbols reflect PL and optical absorption energies. It is found that the bandgap energies as measured by VEELS depend roughly linear on the indium concentration x in $\text{In}_x\text{Ga}_{1-x}\text{N}$ alloys, the band bowing parameter plus calculated curve is given in blue. The systematic deviation of PL and absorption edge energies from the bandgap as measured by VEELS is not restricted to InN but extends to the whole InGaN alloy system. It is interesting that InGaN epilayers produced approximately 10 years ago show no significant deviation between the bandgap energies determined by the different methods. Also, the “fundamental bandgap” for InN as described by the Moss-Burstein theory constantly shifts to always lower values since 2002 (0.8 eV: pink curve) and is currently set to 0.5 eV (purple curve).

It is assumed that the progressing development of $\text{In}_x\text{Ga}_{1-x}\text{N}$ alloys resulted in the formation of local inhomogeneities such as indium-rich clusters as were found in ref. [Jin05]. This is also consistent with our own results, described in earlier chapters. Consequently, if those clusters are the dominant sources for optical transitions, the bandgap of their composition will be measured by PL. As those clusters have a higher concentration of indium than the average indium content in the epilayers (usually measured by x-ray diffraction) lower “effective” bandgap energies are recently measured for those materials while local composition variations are detected in a VEELS analysis which facilitates a correct bandgap determination. Although this does describe the energy variation in InGaN alloys with In concentrations lower than 40%, the origin of the 0.8 eV to 0.5 eV photo-luminescence energy in InN needs to be described as plasmonic resonance of pure indium clusters with different aspect ratios (see chapter 4).

In conclusion, band transitions in wurtzite and zincblende InN grown by molecular beam epitaxy were observed utilizing valence electron energy loss spectroscopy. The respective polytypes of indium-nitride were identified utilizing the energy position of the plasmon peak and the power spectra of the investigated areas. A dominant energy transition is observed for wurtzite InN at approx. (1.7 ± 0.2) eV and (1.4 ± 0.2) eV for zincblende InN which are ascribed to the fundamental bandgaps of the respective InN phases at approximately room temperature. The measured bandgap energy for wurtzite InN correlates well with recently published VEELS data of wurtzite InGaN with indium concentrations lower than 40% and an almost linear bandgap energy function is observed.

5.2 Local Defect Analysis across a GaN / InN interface

This study focuses on the determination of VEELS transitions across an InN / GaN interface. The investigated material is a 1 μm thick InN epilayer deposited by molecular beam epitaxy (MBE) onto a 2 μm thick GaN buffer layer that was grown by metal-organic chemical vapor deposition (MOCVD) onto a c-sapphire substrate. Growth details, structural, optical and electronic properties of the epilayer are given in ref. [Spe04]. The epilayer structure was 4 hours annealed in nitrogen ambient at 600°C. VEELS spectra of transparent samples [Kis97] were investigated with a TECNAI G^2 instrument equipped with an electron beam monochromator, which allows for an energy resolution of 180 meV at a beam size of 1 nm. Prior to the investigation, energy dispersive spectra (EDS) of a 80 nm wide InN/GaN interdiffusion zone were recorded with less spatial resolution with a CM200. VEELS

spectra were recorded along the same EDS scanning line as shown in figure 5.6 in a dark field image. The inset gives the gallium concentration profile (EDS). The interdiffusion zone is indicated as a solid line across the interface. Three scans were taken with identical results at different areas of the epilayer.

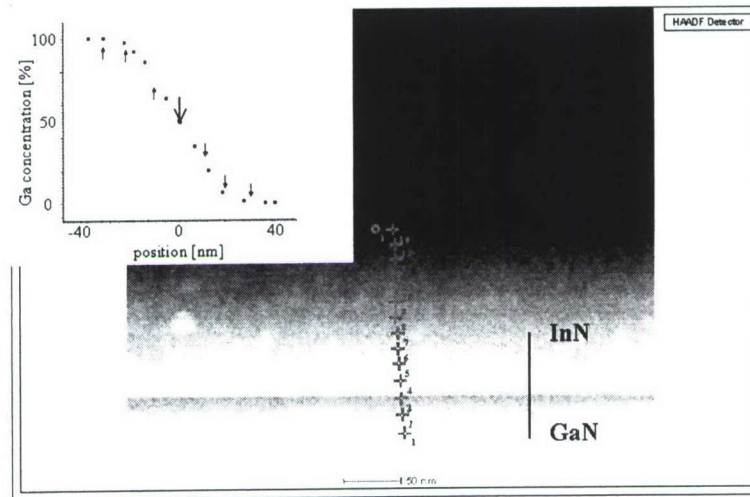


Fig. 5.6: Dark field image of the InN / GaN interface area investigated by VEELS. The markers indicate where the VEELS spectra were taken. The line across the interface gives approximately the area where interdiffusion was measured by EDS. The inset shows the EDS results, given is the gallium concentration in percent for each position (interface at zero).

Figure 5.7a shows three background corrected VEELS spectra recorded directly at the interface. The composition sensitive plasmon peak which is located at (19.5 ± 0.2) eV for GaN and (15.7 ± 0.2) eV for InN [Spe05] was found to change directly at the interface from the GaN energy position to the InN energy position. No gradual plasmon energy peak shift was found that is known from the $\text{In}_x\text{Ga}_{1-x}\text{N}$ alloy system. Therefore we conclude that the investigated grains consist of either GaN or InN rather than an alloy with homogeneous composition. Small compositional changes of $< 8\%$ cannot be monitored, the respective shift of the plasmon peaks would be still within the experimental error. Additionally, both bandgap energies of InN and GaN were found in the VEELS spectra with only small energy variations (0.3 eV). It is possible that small clusters of $\text{In}_x\text{Ga}_{1-x}\text{N}$ do form within the interdiffusion area. However, as the noise signal is relatively high in this defective area (see below) occasionally found small transition onsets at energies around 2.4 eV and 2.9 eV cannot clearly be identified. The presence of InGaN clusters with indium concentrations between 10% and 50% can neither be confirmed nor excluded. Dominant signals, however, are only InN or GaN related which is also confirmed by the plasmon peak positions.

In addition to band transitions, Figure 5.7b shows that transitions within the band gap region of both InN and GaN can occur if VEELS spectra are recorded close to the defect rich interface, which are absent in the more perfect material (Fig. 5.8). Defect related transitions were found before in GaN in the vicinity of an interface [Spe05] but never before in InN as clearly as in Fig. 5.7b. Onset energies between 0.6 eV and

1.0 eV (± 0.2 eV) were found that obviously coincide with energies that are attributed to a low band gap of InN. VEELS spectra were before taken from six different samples with optical absorption edge energies between 0.8 eV and 1.5 eV. In over 100 spectra which were obtained while avoiding extremely thin sample areas and the vicinity to grain boundaries or interfaces, transitions at those low energies were not seen before. It is concluded that those defects are accumulated at the interface. The origin of the defects is currently investigated. It is possible that some of the energies observed are vacancy related which would also explain the large interdiffusion area.

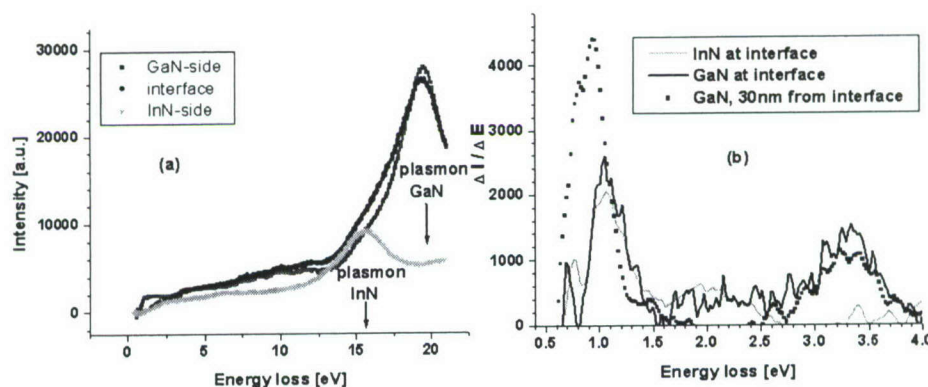


Fig. 5.7: VEELS spectra of interdiffusion area, (a): background removed spectra directly at interface, (b): first derivative of background removed spectra shows the inflection points of various defect and band transitions

It shall be noted that the absence of alloying at the InN / GaN interface is of no consequence to the alloys with high gallium concentration as those are commonly deposited at higher temperatures than the applied annealing temperature (600°C). InGaN alloys with up to 40% indium concentration are already identified by VEELS [Jin05]. For the InGaN epilayers with high indium concentration, however, 600°C is already a high deposition temperature due to the high decomposition rate of these alloys. The high resolution TEM investigation of InGaN epilayers with up to 30% gallium confirms spinodal decomposition which is already described in Chapter 3.

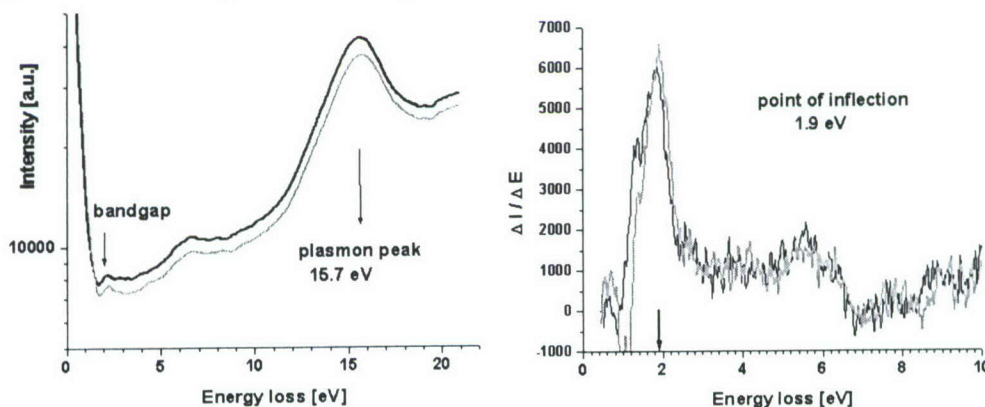


Fig. 5.8: VEELS spectra of InN in less defective areas (not at interface): left: original spectra showing the bandgap onset, right: first derivative of VEELS intensity.

In conclusion, the InN / GaN interface area of an annealed heterostructure was investigated by VEELS and phase separation was observed instead of alloy formation. Within the interdiffusion zone VEELS spectra with energy levels between 0.6 eV and 1.0 eV are present in addition to the band transitions in InN and GaN of (1.7 ± 0.2) eV and (3.3 ± 0.2) eV, respectively that are dominant in defect free regions of the crystals. With those findings it is now also possible to locally obtain high defect concentrations at other critical device areas such as at the AlGaIn / GaN interface in a HEMT structure or under a metal contact in any type of device. The next task logically has to be the quantification of the observed VEELS defect band signals.

5.3 Analysis of InN from Different Sources

InGaIn is a valuable material alloy for electronic devices. The different mechanisms which result in its electrical and optical responses, however, are only partly known and much is yet to discover. The correct mechanisms, however, are essential to control the materials properties beyond a trial and error approach. Significant device parameters, aging effects, yield and reliability are still insufficient so that this material group cannot yet be trusted in critical commercial and military applications such as reconnaissance satellite control, electronics in health care or on a battleship. It is essential to understand a materials behavior in order to reproduce the electronic components. The methods used here to investigate various InGaIn materials are universally applicable to all group III-V compounds and alloys and may assist materials researchers in future in their efforts to develop a variety of different devices including solar cells, detectors and high power electronics. This characterization method is also the ideal tool for integrated materials devices as it is independent on the various materials' components. A proof of principle for an "integrated material system" was demonstrated within a recent STTR project: a GaN epilayer deposited on CVD diamond was successfully prepared into a TEM sample utilizing FIB lift-out technique.

InN is the most complicated compound among the nitrides. Its high defect density and low grain size which is typical for a low temperature deposition [Spe02] makes it difficult to compare epilayers from different sources. This is a known issue in low-temperature GaAs and it took years until the parameters for low temperature growth were finally reproducibly established (see for example [Spe02], [Spe99]). In this study all materials compared are deposited by molecular beam epitaxy in various locations, all known for state of the art MBE growth: at Cornell University (W. Schaff's lab), at the IOFFE Institute in St. Petersburg (T. Shubina's lab) and at UC Berkeley (E.R. Weber's lab). The layers investigated were all grown on sapphire with low temperature AlN and/or GaN buffer layers. The Cornell TEM sample was approx. 5 μm thick while St. Petersburg and UC Berkeley samples were about 1 μm thick. All materials are of high crystalline quality, as determined by x-ray diffraction and their lattice parameters are close to the theoretical value ($a=3.545$ Å, $c=5.703$ Å) [Wri97b]. For a general optical and electrical characterization, a 1 μm thick Cornell epilayer and additional St. Petersburg and UC Berkeley epilayers were also included in this study.

Figure 5.9 shows the optical absorption of the above three sample types (using the 1 μm thick Cornell sample, red curve) together with some literature results [Mon05], [Shu04b], [Wu04], the absorption coefficients are shown as α^2 . The various graphs highlight

different data ranges of the same plots which show how different authors could come to very different theoretical modeling for the “same” material. Figure 5.9a shows the basis for the Moss-Burstein theory of InN: If absorption coefficients up to a final α value around $1\text{E}4$ are evaluated many materials show a dependence of the optical absorption to the averaged free electron concentration in the epilayers (measured by Hall effect, the carrier accumulation at the surface is included in this averaged measurement). In Fig. 5.9a one of the new UC Berkeley samples (blue curve) does not follow this trend, the Monemar, Cornell and other UC Berkeley samples do (the free electron concentration of the St. Petersburg samples is unknown). Figure 5.9b shows a larger absorption range which acknowledges the high absorbance of InN. In this plot it is clearly seen that the various materials are not comparable: the Cornell samples show abrupt total absorption at specific energies, here 1.1 eV and 1.6 eV (which is dependent on the sample thickness), the absorption of the Monemar samples exhibit a slight increase in absorption to energy values around 2.0 eV [Mon05], the old UC Berkeley sample shows a very late absorption onset, possibly due to incomplete coalescence of the InN grains (artificial onset). The St. Petersburg and new UC Berkeley samples show distinct absorption peaks, but at different energies. The absorption peaks are shown more clearly in Fig. 5.9c. While in both sample sets two peaks are distinguishable, the peak energies are only the same for samples of the same origin: 1.1 eV and 1.65 eV for St. Petersburg, 1.35 eV and 2.0 eV for UC Berkeley. The new UC Berkeley samples show a strong band-type absorption increase at 2.1 eV for both epilayers ($[n] = 4 \times 10^{18}/\text{cm}^3$ and $2 \times 10^{19}/\text{cm}^3$, respectively).

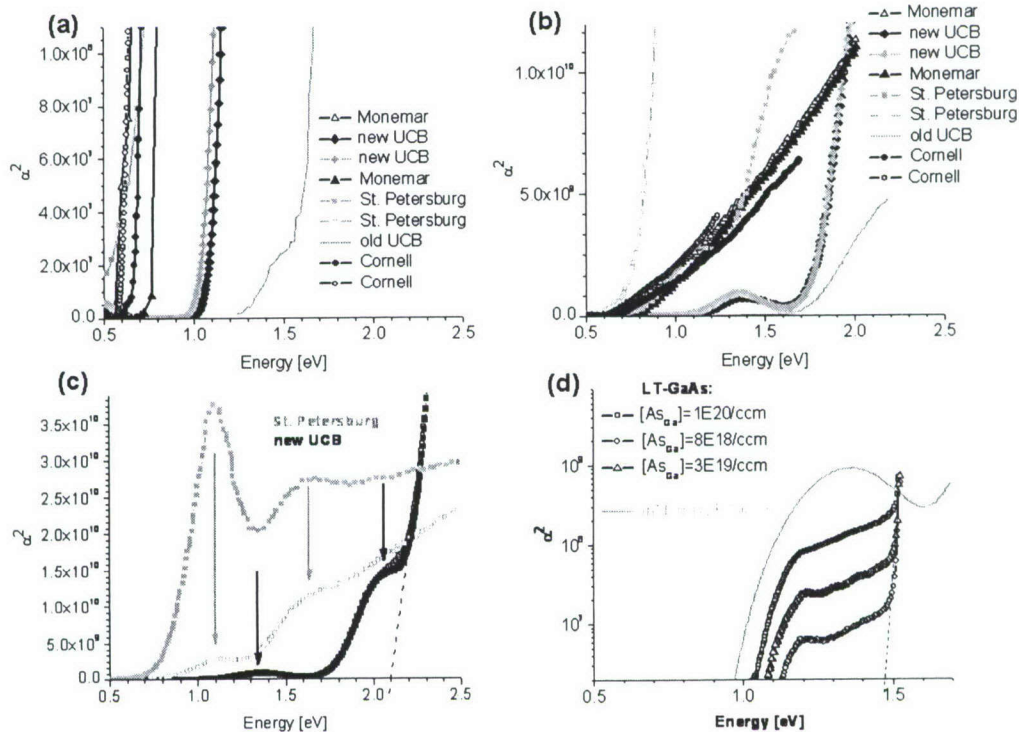


Fig. 5.9: Optical absorption for various MBE grown InN epilayers: (a): $\alpha^2_{\text{max}} = 1.1\text{E}8$ / (b): $\alpha^2_{\text{max}} = 1.2\text{E}10$ / (c): $\alpha^2_{\text{max}} = 3.9\text{E}10$ / (d): $\alpha^2_{\text{max}} = 9\text{E}9$, LT-GaAs absorption curves for comparison

Figure 5.9d shows the effect of a known defect-rich low-temperature III-V compound on the optical absorption. In LT-GaAs the neutral arsenic antisite defects produce a significant additional absorption when they are present in a single-crystalline material. In InN the situation is far more complicated with structural defects, grain boundaries, sometimes even residual contaminants and a highly conductive surface all possibly contributing to enhanced absorption. For opto-electronic applications, however, the absorption of InN has to be reproducible. It is therefore imperative that the origin of the different absorption mechanisms is determined. At the various growth laboratories those mechanisms are obviously reproducible but technology transfer to industrial processes will have a higher success rate when those mechanisms are understood so that defect engineering and not the choice of the specific grower will determine the materials overall properties.

Comparing VEEL Spectra of InN

Valence EELS is a fast growing experimental technique that probes material properties locally. In principle VEELS results are of large benefit to the materials science community since dielectric materials properties including optical absorption are locally probed. However, there is room for improving our theoretical understanding of VEEL spectra and generally acceptable quantification methods must yet be developed. Nevertheless, there is a principle disconnect between such *microscopic* measurements, which are available in a few microscopy laboratories, and similar *macroscopic* measurements, which are widely spread across the materials science community. If macroscopically homogeneous materials are considered, there is obviously limited need to apply both tools. In today's emerging new materials, however, the degree of inhomogeneity can be high with indium-nitride as a prominent representative for a rather inhomogeneous material system. In this case macroscopic measurements are bound to provide debatable averaged properties that must be understood as a sum of locally varying properties as shown in figure 5.10 for local and global absorption measurements in InN.

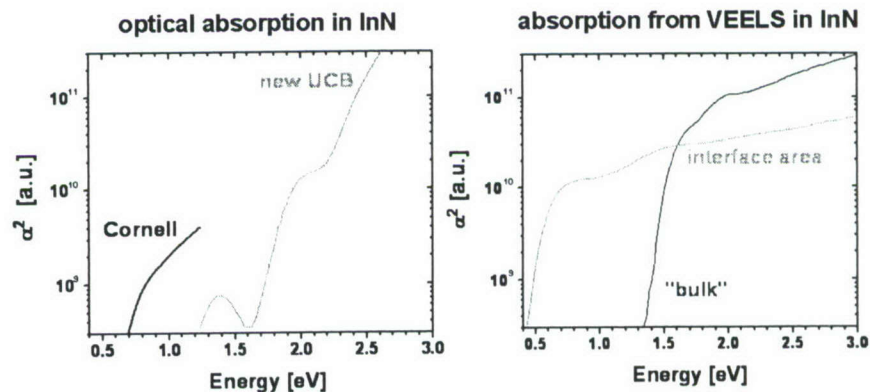


Fig. 5.10: Optical absorption, measured for different samples (Cornell University / UC Berkeley at left) and as calculated from VEEL spectra taken at different TEM sample areas (right)

The low-loss or valence region of an electron energy-loss spectrum (< 50 eV) provides similar information to that provided by optical spectroscopy, containing valuable

information about the band structure, in particular about the absorbance and the dielectric function of a material. The realization of VEELS as a viable characterization technique in transmission electron microscopy (TEM) has mainly been hampered by the limited energy resolution of conventional instruments. Recent developments of electron optical devices have led to the availability of (scanning) TEMs equipped with electron monochromators [Ter99], [Tie99], [Ben04] and high-resolution electron energy loss spectrometers [Bri03]. The fine structure of core-loss edges can now be recorded with high precision, allowing for a direct comparison with electronic structure calculations [Ars03]. In addition, the narrow tail of the zero-loss spectra can be analyzed down to an energy loss of approx. 0.5 eV. This resolution mainly depends on the symmetry of the zero loss peak and its temporal stability. For VEELS measurements at high spatial resolution, the microscope is operated in the scanning transmission mode as sketched in figure 5.11 (left). A typical GaN VEELS spectra and the first derivative of the background removed spectra (zero loss subtracted) which displays different electronic transitions as peaks are also shown. The here used TECNAI instrument currently provides an energy resolution of 200 meV under best alignment conditions and an electron probe diameter of 1 to 2 nm. The operation conditions for the scanning TEM mode require a lowered overall electron beam intensity which is approximately two orders of magnitude lower than for TEM mode. Additionally, the monochromator transmits only a few percent of the incoming electron beam which results in roughly four orders of magnitude lowered beam intensity for a VEELS analysis. This can be compensated by a 2 orders of magnitude smaller diameter of the illuminated area in VEELS which results in a 4 orders of magnitude larger electron flux. In summary, electron beam damage due to high-resolution TEM and VEELS analysis should therefore be in first order comparable. As VEELS data are recorded on a few seconds time scale electron beam damage is negligible.

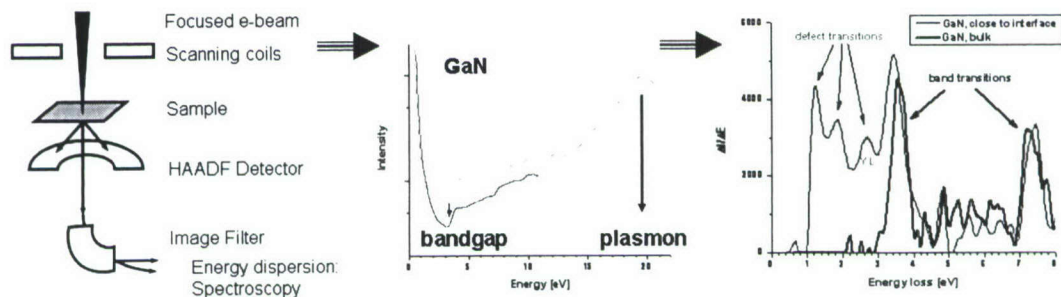


Fig. 5.11: Sketch of scanning TEM (STEM) mode for local spectroscopy (EELS) (left), typical VEELS of GaN sample (middle) and first derivative of the background subtracted spectra (right). The latter shows band (black and blue) and defect transitions (blue only) dependent on the area where the scan was taken.

A typical VEEL spectrum recorded at the Berkeley TECNAI provides reproducible data for electron loss energies of 1 eV and higher. The reproducibility of transitions in the energy range below 1.0 eV is still investigated. Fig. 5.12 shows VEEL spectra of the St. Petersburg, the UC Berkeley and the Cornell materials. For better comparison and to eliminate any variations in potential surface and volume effects (see below) TEM sample areas of the same thickness ($37 \text{ nm} \pm 20\%$) are compared. The UC Berkeley sample which was taken in the vicinity of a GaN / InN interface shows transitions at 1.2 eV and

1.8 eV as does the St. Petersburg sample which was intentionally inhomogeneously deposited (see chapt. 4). The St. Petersburg sample also shows the characteristic 11.2 eV metallic Indium bulk plasmon peak which to the best of our knowledge was seen for the first time in InN and only in one sample (the volume of indium clusters to the host material is large enough to produce a distinct peak). As has been shown by Shubina et al. [Shu06], such metallic clusters can cause Mie scattering and explain the absorption and luminescence behavior of InN. This investigation, however, does NOT confirm this theory; it only proves the EXISTENCE of metallic Indium clusters in the St. Petersburg samples. In chapter 4 it was shown that clusters can also be imaged by high-resolution TEM although to date it cannot not unambiguously shown that those clusters are indeed metallic indium inclusions. It is also, at least theoretically, possible that those clusters are highly strained, possibly contaminated cubic InN particles. Only the new TEM microscope will be able to resolve indium and nitrogen atoms in InN and therewith will enable us to distinguish between cubic indium nanoclusters and cubic InN [TEA]. The Cornell sample which was the thickest among the three does not show a transition at 1.2 eV but instead shows a double peak transition at 1.6 eV / 1.9 eV which corresponds to the appearance of occasional zincblende inclusions in the wurtzite matrix of this material.

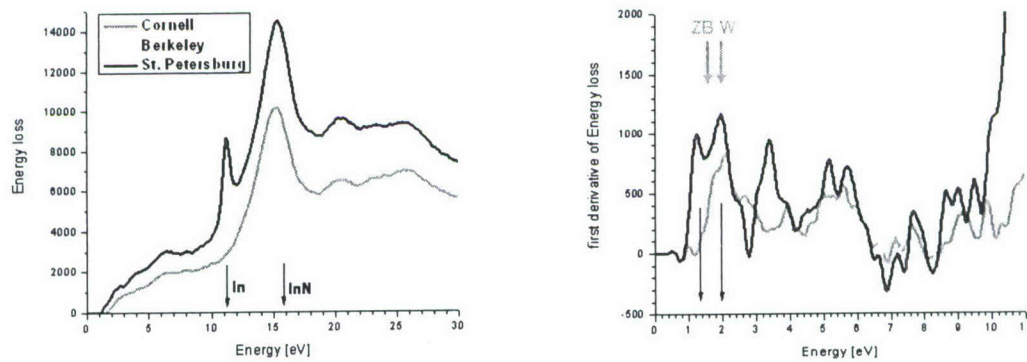


Fig. 5.12: VEELS analysis for three different InN epilayers and their respective first derivatives (right), details in text

5.4 Considerations about band gap measurements of InN by VEELS in STEM

Transmission valence electron energy-loss spectroscopy of InN reveals a band gap of 1.7 eV conflicting the latest experimental and theoretical studies on InN that conjecture a band gap energy well below 1 eV. A detailed analysis is presented giving evidence that the VEELS result neither is impaired by spectral artifacts related to the relativistic interaction of the electrons with the thin films nor by potential surface layers of increased electron concentration. This finding can only be explained by assuming that the thickness of the surface layer of increased electron concentration is significantly larger than presumed, or by proposing that the band gap of InN is indeed ~ 1.7 eV.

The controversy about the band gap of InN has not yet been resolved. A gap energy of 1.9 eV had been accepted [Fol86] until only roughly five years ago experimental results indicated that the band gap of InN could be well below 1 eV, namely around 0.7 eV [Wu02a, Dav02]. Since then, many experimental results and theoretical analyses have been carried out that support the low band gap conjecture. The

formerly accepted high band gap concept has been replaced to a large extent. However, one of the arguments objecting this trend is the gap energy that is measured by valence electron energy-loss spectroscopy (VEELS) in (scanning) transmission electron microscopy (STEM). Depending on the crystal structure, i.e., depending on whether InN has the wurtzite or the zincblende structure, VEELS reveals gap energies of (1.7 ± 0.2) and (1.4 ± 0.2) eV, respectively (see, reference in [Spe06]), supporting the formerly known band gap value.

The application regime of a semiconductor is mainly determined by the configuration of valence and conduction bands. This fact combined with the promising properties of the material itself reasons the efforts in accurately determining the electronic structure and the band gap of InN. The nitrides of the group III elements Al, Ga and In and alloys of these binary compounds are semiconductor materials frequently used in electronic devices particularly for optoelectronic applications. AlN has a band gap of 6.2 eV, whereas the band gap of wurtzite GaN is 3.4 eV. Hence, AlN and GaN cover applications in the ultra-violet and visual regime respectively. InN being subject of intense research for about 10 to 15 years is a more difficult material. With a band gap of ~ 0.7 eV, InN would be suitable for applications in the near infrared regime. Whereas in the case that its band gap is ~ 1.7 eV, InN would be useful, in particular, to expand the optical regime of GaN applications towards longer wavelengths.

InN is a difficult material because its properties drastically depend on the actual characteristic of the material. Even examining the characteristic of a certain InN sample is not trivial. The electronic properties of InN can be impacted by the exact stoichiometry, impurities like oxygen or for instance by quantum size effects [But05, Mon05]. Producing qualitatively equivalent materials by different methods has turned out to be challenging. The controversy about the band gap of InN has not yet been resolved because of contradicting experimental results and because both conjectures could in principle be refused. Namely, apart from identifying the absorption feature around 0.7 eV with the band gap of bulk InN, the absorption below 1 eV could also be explained by a deep level trap caused for instance by impurities. On the other hand, gap energies measured above 1 eV could be explained by being impacted by the Burstein-Moss effect.

One point that seems to be crucial in discussing the electronic properties of InN is the strong variation of the charge carrier concentration in different InN samples. This pronounced variation likely is caused by material defects [Cim06] including the effects mentioned above [But05, Mon05]. Due to the strong electron affinity of InN, a distinct n-type doping is observed, even in nominally undoped material. Furthermore, that the Burstein-Moss effect can affect the measurable gap energy of InN is in general accepted. The severity of the Burstein-Moss effect is controversial though. Wu et al. [Wu04] reported that due to the Burstein-Moss effect the gap energy changes from 0.7 eV to 1.7 eV if the charge carrier concentration changes from $\sim 2 \times 10^{18} \text{ cm}^{-3}$ to $\sim 4 \times 10^{21} \text{ cm}^{-3}$.

Measurements of the electron concentration of InN revealed a distinct surface accumulation of negative charge carriers (see, e.g., [Lu03]). The carrier concentration at the surface can reach up to about $4 \times 10^{20} \text{ cm}^{-3}$ whereas within a layer of 3 to 7 nm it drops to the bulk value below about 10^{18} cm^{-3} [Lu03]. The actual electron concentration depends on the InN material, but the values given are generally valid for “good” InN materials. The accumulation of negative charge carriers at the surface along with a strong

Burstein-Moss effect would lead to an increase of the band gap at the surface. Experimental techniques that probe surface and/or near-surface material would not reproduce the actual bulk properties. It is for this very reason why VEELS in STEM could produce results that are altered by surface effects explaining the high gap energy measured by this technique.

Transmission VEELS is carried out using electron transparent foils that typically have a thickness between 25 and 100 nm. Using a microscope that is equipped with an electron monochromator, an energy resolution of better than 200 meV can be achieved [Ern05]. Although the spectroscopic resolution of VEELS does not quite reach the resolution of optical methods, the advantages of VEELS in STEM are the spatial resolution (~ 1 nm) and the straightforwardness. As the data can be analyzed, no modeling is required (see, e.g., refs. [Ern05, Yua88, Raf98, Laz06]). Yet there are potential artifacts that can alter the energy-loss function measured by VEELS, namely surface, finite sample and retardation effects. However, it has been shown that for a broad class of semiconductors these effects are not significant, provided that the thickness of the sample is in the range of 25 to about 100 nm [Ern07]. For other materials, like, e.g., Si and GaAs, retardation effects can lead to spurious spectral artifacts that complicate the interpretation of VEELS data.

This chapter aims at answering the following questions;

1. Does the increased electron concentration at the surface of the thin foils used in STEM mask the dielectric bulk information?
2. Do artifacts like retardation, finite sample or surface effects mask a potential transition at ~ 0.7 eV in VEELS?

Dielectric theory provides concepts to analyze different spectral contributions in VEELS, such as bulk dielectric losses, surface, finite sample size and retardation effects (see, e.g., [Ern07]). On the basis of these concepts VEEL spectra were calculated and compared with experimental data. Two different dielectric functions (DFs) were used for calculating the spectra. One DF shows a band gap of 0.7 eV, whereas the other DF shows a modeled (pseudo) band gap of 1.7 eV. The DFs, provided by Goldhahn et al. (see, e.g., [Gol06]), are based on data collected by spectroscopic ellipsometry that revealed a band gap of 0.7 eV for a material with an electron concentration of $1.5 \times 10^{18} \text{ cm}^{-3}$. Modeling the impact of the Burstein-Moss effect, the band gap becomes a pseudo gap that essentially depends on the electron concentration. The DF that shows the 1.7 eV band gap corresponds to a fictitious material with an electron concentration of $\sim 10^{20} \text{ cm}^{-3}$.

VEELS data are commonly analyzed assuming that the bulk dielectric response solely contributes to the signal. Under this assumption, the energy-loss function can be analyzed in order to directly extract bulk dielectric data such as transition energies and the DF. However, if the speed of the incident electrons exceeds the speed of light in the material under investigation, retardation effects can occur. Figure 5.13a shows VEEL spectra calculated using the DF that corresponds to an InN material with a band gap of 0.7 eV. The foil thickness is 60 nm. The solid line was obtained by applying the Kröger equation [Krö68] considering bulk dielectric losses, surface, finite sample and retardation effects, whereas the dashed line was calculated considering solely non-retarded bulk dielectric losses. The dashed line is commonly assumed when VEELS data are analyzed. The dotted line shows the difference between these two spectra. Figure 5.13b shows the equivalent spectra for the DF with the 1.7 eV energy gap.



Figure 5.13: Calculated VEEL spectra of InN; in (a) a DF of InN was used that shows a band gap energy of 0.7 eV in (b) a DF was used that shows a band gap energy of 1.7 eV. The full lines were calculated according to the Kröger equation taking bulk dielectric losses, surface and retardation effects into account. The dashed lines show non-retarded bulk dielectric losses only, and the dotted lines show the difference between full and dashed line. DF were provided by Goldhahn et al. [Gol06].

Figure 5.13 reveals that retardation and surface effects substantially contribute to the VEELS signal of InN. Considering retardation effects (solid line), the integrated spectral intensity is increased by a factor of more than 2.5 compared to the non-retarded case (dashed line). A smooth retardation contribution can be found even in front of the band gap signal. The dotted curves in figure 5.13 basically represent the retardation and surface contributions that usually are neglected when analyzing VEELS data. The strong retardation effect complicates the extraction of the DF from experimental VEELS data of InN. Because the DF is derived by applying a Kramers-Kronig transformation that relies on the sum rule, the retardation background would lead to inaccurate absolute dielectric data. However, although the retardation and surface contributions change the relative

intensity of the individual absorption features, their position is not changed. This means that even in the presence of the retardation and surface effects transition energies can be determined reliably. Retardation, surface or finite sample effects do not alter the position of the band gap signal, neither the one at 0.7 eV, nor the one at 1.7 eV. From this analysis it can be concluded that independent from the position of the actual band gap signal, VEELS reflects the correct band gap signal. Although the retardation contribution is significant, there are no spectral artifacts that would mask or even shift the band gap signal.

The band gap energy of InN determined by VEELS is 1.7 eV [Spe05]. Figure 5.14 compares an experimental VEEL spectrum with one that was calculated according to the Kröger equation [Krö68, Ern07] using the DF with a (pseudo) band gap of 1.7 eV. The experimental setup is described in ref. [Ern05], the InN sample is described in ref. [Spe05]. Although the spectral resolution of the experimental spectrum is lower, the calculated spectrum reproduces well the main absorption features of the experimental spectrum. Particularly the band gap signal (E_0) and transitions E_1 , E_3 and E_4 are well reproduced. The inset in figure 5.14 shows that no absorption feature below the presumed band gap signal can be found in the VEELS data. However, one problem associated with the background removal of the tail of the zero-loss peak concerns the retardation contribution. The smooth retardation feature in front of the gap signal that is apparent in the simulation cannot be distinguished from the tail of the zero-loss peak in the experimental spectrum. In fact, the entire retardation contribution throughout the spectral range cannot be considered properly. The individual absorption features show the correct position, but the (relative) intensity is altered by the retardation contribution.

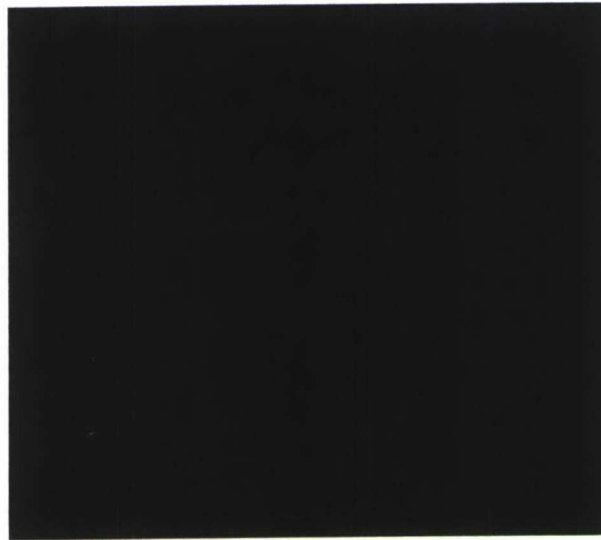


Fig. 5.14: Comparison between an experimental and a calculated VEEL spectrum of InN. The spectrum (0.3-10 eV) was calculated according to the Kröger equation using a DF that shows a first transition energy E_0 of 1.7 eV. The inset shows the experimental spectrum and the power-law background model (dotted line) used to remove the low-energy tail of the zero-loss peak. Transition energies are labeled according to Goldhahn et al. [Gol06]. The experimental low-loss spectrum was spliced (at 10.5 eV) with the corresponding spectrum containing the plasmon peak.

This comparison shows that VEELS of InN is in qualitative agreement with dielectric data derived from spectroscopic ellipsometry provided, however, that dielectric data are taken which show a gap energy E_0 of 1.7 eV. And therein lies a problem; ellipsometry data that show a (pseudo) band gap signal of 1.7 eV implies that the electron concentration is of the order of $\sim 10^{20} \text{ cm}^{-3}$. The InN material used for the study has however a bulk electron concentration of $\sim 10^{18}$ to 10^{19} cm^{-3} only [Spe05]. According to the ellipsometry data which are based on the Moss-Burstein model [Wu02a, Gol06], the InN sample should show a band gap of ~ 0.7 to 0.9 eV.

Can a surface layer of increased electron concentration mask the bulk dielectric band gap signal? The increased electron concentration at the surface of an InN foil can be modeled using a 3 layer model. A top and a bottom surface layer of increased electron concentration (~ 5 nm, $\sim 10^{20} \text{ cm}^{-3}$) and an actual bulk layer of varying thickness d_{bulk} (see inset in figure 5.15). The calculated thickness series of VEEL spectra in figure 5.15 reveals the impact of the surface layer. The DF used to model the surface layers (top and bottom) corresponds to a bulk material with an electron concentration that results in a (pseudo) band gap energy of 1.7 eV, whereas the bulk layer shows a band gap of 0.7 eV. The spectra in figure 5.15 were calculated according to the dispersion-bracket formalism by Bolton and Chen [Bol95], which allows for calculating VEEL spectra taking into account the actual bulk dielectric contribution as well as surface, interface, finite layer thickness and retardation effects. None of the spectra shown in figure 5.15 does mask the band gap signal of the central layer. Even for a bulk layer of 5 nm, the band gap signal at 0.7 eV is clearly visible. This obviously contradicts the experimental results that do not show any intensity modulation below 1 eV (see inset in figure 5.14). In case that there is a bulk layer of lower band gap, it would be observable by VEELS.

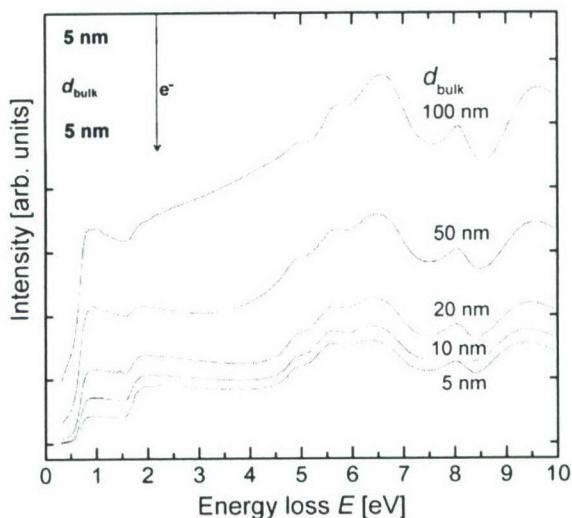


Fig. 5.15: Calculated VEEL spectra of a three layer model consisting of surface layers of high electron concentration (top and bottom, 5 nm), and of a bulk layer of varying thickness d_{bulk} and reduced electron concentration corresponding to the bulk value. The spectra were calculated according to the Bolton-Chen formalism [Bol95] using dielectric data of Goldhahn et al. [Gol06]. For details see text.

This work shows that although retardation effects substantially contribute to the VEELS signal of InN, reliable information about the band transition energies can be derived. Surface, interface, and retardation effects do not mask or shift the band gap signal. Surface layers of increased electron concentration do not mask a low-energy band gap signal either. The 1.7 eV gap energy of an InN material with a bulk electron concentration of nominal $\sim 10^{19} \text{ cm}^{-3}$ derived from VEELS cannot be explained on grounds of artifacts caused by the experimental technique. This result can either be explained by proposing that the surface layer of increased electron concentration is clearly thicker than measured [Lu03], or by assuming that the band gap of InN is indeed $\sim 1.7 \text{ eV}$.

5.5 Conclusion

The above shown experimental results and simulations suggest that InN is indeed a high bandgap material with an unusually strong optically active defect population. It seems to be an ideal model substance which may be applicable as a multi-response material in a variety of optical devices including detectors and solar cells.

6. GaN Growth on Diamond

Gallium-nitride high-electron-mobility transistors fabricated on diamond substrates are highly desired for use in high-power amplifiers for X-Band radar systems and commercial cellular-base stations. Diamond substrates have high thermal conductivity which enables highly efficient removal of heat from the active device regions. At present, at least three different ways of implementing diamond substrates are explored: sp3 Inc. pursued the direct overgrowth on their CVD diamond substrates and 1mm thick diamond layers on silicon substrates within an STTR phase I project, the same company entered into a SBIR phase II project, investigating GaN overgrowth on diamond sandwiched between SOI wafers and Group4Labs explores a novel bonding techniques of lift-off GaN onto CVD diamond. The latter GaN epilayer is initially deposited onto silicon. The Berkeley group was involved in all three projects and assisted those efforts within the AFOSR project with some material characterization. We are here reporting first results.

Motivation:

The performance and reliability of present day microwave power amplifiers in the X-band are limited by high operating temperatures resulting from self-heating [Hu04, Ros05, Rol02]. Efficient thermal management is essential for lowering the heat generation and active area temperature. The use of large metal heat-sinks with active cooling provides low-thermal conductivity backgrounds, but cannot reduce the temperature drop in the immediate neighborhood of small submicron heat sources such as field-effect transistor gates. Heat conductivity around such small geometries is best accomplished by spreading heat to larger areas and volumes. Heat spreading is most efficient when a high thermal conductivity material is brought into the immediate vicinity of the heat source, which means that the distance from the heat source to the heat spreader has to be comparable to the heat-source size. For semiconductor devices this means on the order of a micrometer. This level of proximity is only possible with highly

thermally conductive substrates onto which the semiconductor devices are directly attached or on top of which the device epilayers are grown.

The ideal substrate for gallium nitride (GaN) high-power transistors would be a substrate that is highly thermally conductive, electrically insulating, and has cost comparable to that of silicon. Synthetic diamond wafers manufactured by chemical vapor deposition (CVD) are likely candidates to optimally satisfy these requirements. The greatest advantage of diamond substrates is their thermal conductivity. In insulators, heat is conducted by lattice vibrations. With sound velocity exceeding 17 km/s, diamond has heat conductivity higher than any other man-made substance: Polycrystalline diamond typically has thermal conductivity between 1200 and 1500 W/mK, top values go up to 2000 W/mK (sp³). This thermal conductivity is more than three times better than silicon carbide ($\kappa \sim 400$ W/mK). Silicon and sapphire (also common GaN-epilayer substrates) have thermal conductivities around 150 W/mK and 35 W/mK, respectively. The electrical resistivity of polycrystalline diamond ranges between 10^{13} to 10^{16} Ω cm, which is comparable to that of sapphire (10^{17} Ω cm) and significantly better than that of SiC (typically 10^6 Ω cm).

Figure 6.1 summarizes the two bonding techniques currently investigated when producing GaN on diamond heterostructures. The Group4Labs process is schematically illustrated in section (a): The process starts with GaN HEMT epilayers grown on a silicon substrate, but other materials, such as, sapphire, silicon carbide, or aluminum nitride may be used. The top surface of the GaN epilayers is the surface on which the gates of the HEMT will be realized in the last step of transistor manufacturing. In the first step of the process a sacrificial carrier wafer is attached to the top surface of the gallium nitride layers. During this step the surface of the GaN layers remains protected. The original substrate on which the GaN layers were grown is now removed using either a wet chemical or dry etch process that is selective to GaN. Section (b) describes the bonding process by sp³. The main difference to the Group4Labs process (besides the specifics of the bonding condition) is the fact that the top substrate layer in the sp³ process is SOI based and overgrowth takes place on the silicon template AFTER bonding. Figure 6.2 shows the photo-luminescence of a GaN epilayer directly deposited onto CVD diamond and details of the GaN photo-luminescence taken after the Group4Labs bonding process and – as reference – from the original GaN wafer as grown on silicon. To date no PL data is available for the sp³ process.

The low-temperature (18 K) photoluminescence measurements compare the emissions from a reference sample of GaN epi on silicon and the same gallium nitride epilayer attached to diamond (Fig. 6.3). The pump source was a HeCd 325 nm laser at power 1 mW. Figure 6.3b shows the photoluminescence spectra at room temperature. The following features are visible in 6.3: (a) The intensity of the on-diamond epilayers is smaller than the on-silicon epilayers, (b) the exciton peaks can be resolved for the on-silicon layers but not for the on-diamond layers, (c) the PL spectra of the on-diamond epilayers is shifted towards higher energy by approximately 37 meV, and (d) the yellow and blue luminescence (present GaN) is more pronounced in the on-diamond samples. Observations (a) and (b) may be due to the fact that GaN on silicon is still of higher crystalline quality than GaN on diamond. Also, the increase in YL and BL are commonly described by an increase in defect population. For the YL a local increase in gallium vacancies at the interface between the GaN and the diamond is likely, while the BL may

be attributed to local carbon contamination. In addition to these characteristics a drop in blue luminescence (BL) was observed upon continuous laser exposure for 30 minutes and again after 60 minutes (not shown here). The yellow luminescence does not show any time effects.

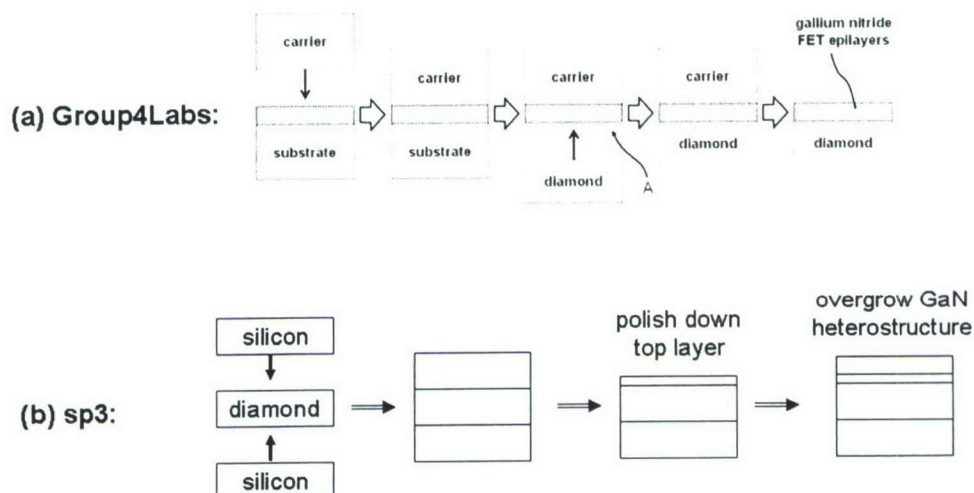


Fig. 6.1: How to produce GaN on Diamond, graphical description of two different techniques

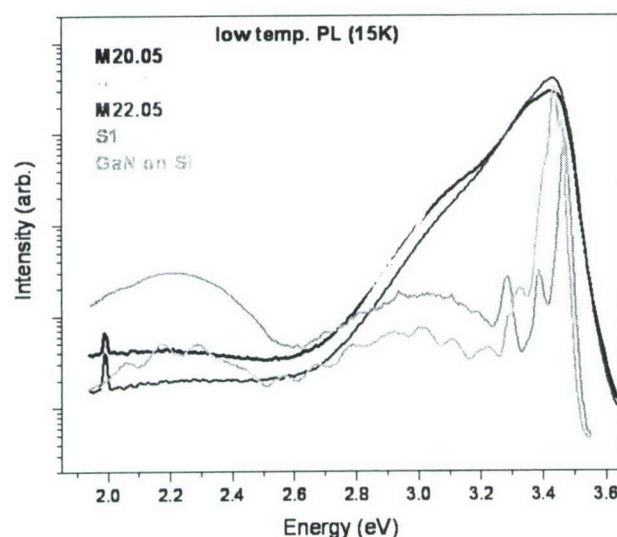


Fig. 6.2: Comparing PL data from GaN epilayers: (red) group4lab GaN on diamond, (pink) reference GaN on silicon substrate, (black, green, blue) various GaN epilayers, directly grown on sp3 CVD diamond templates

The drop in BL intensity is more pronounced for the samples attached to diamond. This optical instability was recorded before [Arm05] and will likely have electrical effects as trapping / charging occurs. We expect persistent photoconductivity to occur for the samples on diamond and – to a lesser degree – for the GaN on silicon sample. GaN epilayers grown on silicon or attached to diamond are under tension at any temperature

below the growth (or attachment) conditions. This is because the GaN thermal expansion coefficient perpendicular to the c-axis ($3.3 \cdot 10^{-6}/\text{K}$) is larger than that of silicon ($2.8 \cdot 10^{-6}/\text{K}$) and diamond ($0.8 \cdot 10^{-6}/\text{K}$). Part of the PL energy shift – feature (c) - can be attributed to the strain induced by the difference in the thermal expansion coefficients between epilayers and substrate. At room temperature this difference is merely 12 meV. However, the relative energy shifts due to the thermal effect can only account for about one forth of the observed PL shift. At present it is unknown what the role of the dielectric adhesion layer is in these shifts. More insight may be achieved when utilizing advanced TEM analysis, for example when local strains can be measured by convergent beam electron diffraction (CBED) techniques. Also, the local population of defects may be accessible through a VEELS analysis [Spe06].

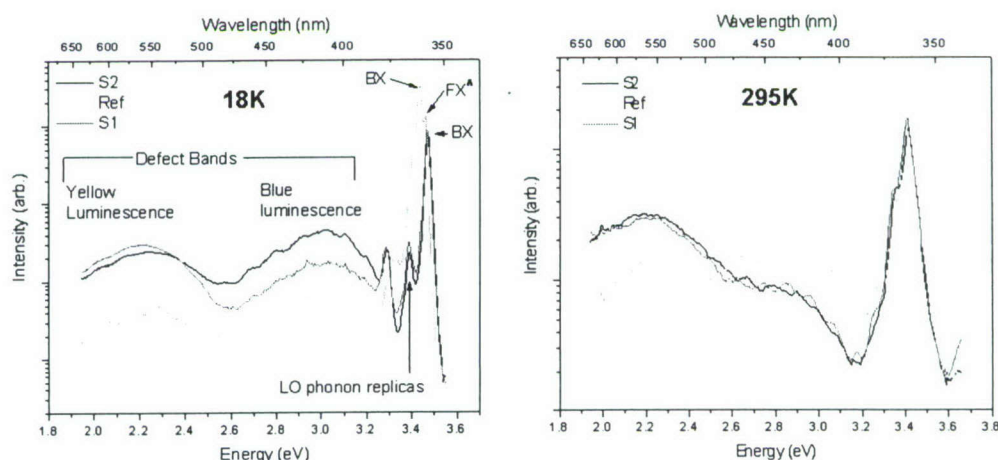
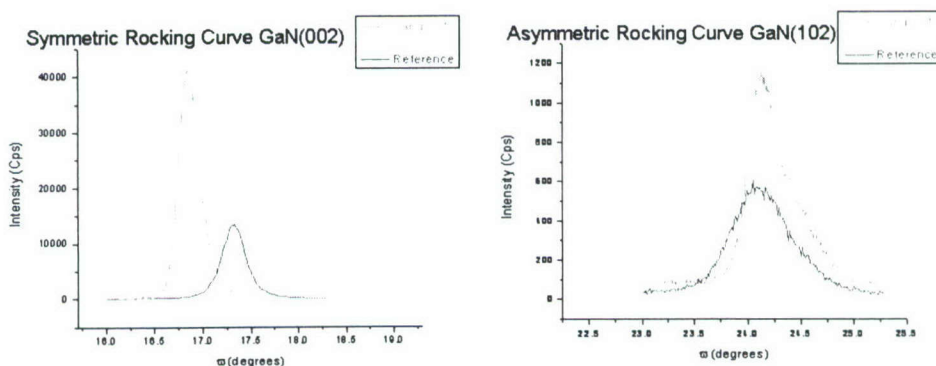


Fig. 6.3: Group4Labs' GaN on diamond epilayers are compared with a GaN reference wafer on silicon, all photo-luminescence data, data left and right are taken at different temperatures



GaN bonded on diamond	Rocking Curve GaN (002)	Rocking Curve GaN (102)
Sample 1	0.2482 deg	0.3853 deg
Ref. (on silicon)	0.2810 deg	0.5727 deg

Fig. 6.4: X-ray diffraction data from GaN on diamond (Group4Labs)

The most remarkable feature in the PL spectra of GaN directly grown on diamond (Fig. 6.2) is the absence of yellow luminescence. The blue luminescence is expectedly high due to large amounts of diffused carbon. As the spectra are taken from the first growth runs the buffer layer growth is not optimized and the layer therefore isn't an efficient diffusion barrier.

Another problem which still has to be addressed is the reproducibility of the materials: As figure 6.4 shows the two GaN samples on diamond have quite different crystalline quality with one sample even having a smaller full width of half maximum than the reference sample. Summarized, the first results of GaN on diamond are quite promising, the functionality of HEMT devices processed from these materials was demonstrated [Fe107] but much work still lies ahead before devices with high reliability can be produced utilizing this new and exciting technology.

7. Summary

This project focused on novel growth and characterization techniques which allow for a progress in future group III – nitride device applications. A methodology for quantitative HRTEM analysis by strain measurement in lattice mismatched alloys was presented in Chapter 2. Three factors for reliable strain measurement were identified:

- (a) The samples must be free of preparation damage as can be realized by using a wet etching technique or low energy (<500 kV) ion milling.
- (b) Damage from the imaging beam must be avoided as can be done in $\text{In}_x\text{Ga}_{1-x}\text{N}$ and other sensitive materials if exposure time is kept below two minutes and beam current density is low (<30 A/cm²).
- (c) Imaging artifacts can be avoided by using high voltage microscopes (acceleration voltage ≥ 800 kV), averaging over series of images or by performing exit wave reconstruction.

With these conditions satisfied, lattice relaxation in wedge shaped TEM samples was accurately measured and modeled. Finally, it was shown how clustering can be distinguished from a purely random distribution of atoms in a crystalline alloy.

The distribution of indium atoms in $\text{In}_x\text{Ga}_{1-x}\text{N}$ alloys was studied in Chapter 3. In $\text{In}_x\text{Ga}_{1-x}\text{N}$ quantum wells, clustering was detected for $x > 0.1$ while noise did not allow an assessment for $x < 0.1$. In thick $\text{In}_x\text{Ga}_{1-x}\text{N}$ layers, a stripe-like composition modulation characteristic for spinodal decomposition was found. Values for the decomposition amplitude in $\text{In}_x\text{Ga}_{1-x}\text{N}$ quantum wells and thick $\text{In}_x\text{Ga}_{1-x}\text{N}$ films were compared to each other and show identical functional dependencies. This provides strong evidence, that cluster formation in $\text{In}_x\text{Ga}_{1-x}\text{N}$ quantum wells can be explained by a thermodynamic process similar to spinodal decomposition in bulk $\text{In}_x\text{Ga}_{1-x}\text{N}$. The center of the miscibility gap was placed around $x = 0.5$ to 0.6 .

InN samples were searched for nanometer-scale inclusions that can be present below the detection limit of X-ray diffraction. Indeed spots of contrast were found and explained by metallic indium inclusions. The size of the clusters correlates with a change in luminescence. The infrared resonances or parallel band transitions of indium clusters may thus strongly influence the optical properties of the InN.

Optical characterization of various InN epilayers clearly showed the SIMULTANEOUS presence of at least three strong optical transitions which commonly is a feature of defects in a material (Chapt. 5). The “low bandgap” or Moss-Burstein theory for InN was demonstrated to be implausible, the InN compound should rather be understood as a “variable bandgap” material system. The observed optical transitions:

- (a) between 0.5 eV and 0.8 eV, the exact transition energy depends on the stoichiometry conditions, substrate temperature and contamination levels during growth
- (b) between 1.1 eV and 1.4 eV, the transition is strongest in nano-structures and was also measured close to interfaces / surfaces
- (c) between 1.7 eV and 2.1 eV which was measured in optical absorption of clean MBE grown epilayers and in sputtered materials as well as in VEELS analysis (the respective transition of the cubic material is neglected here)

are relevant for multiple device applications. It is of special interest to pursue the idea of exploiting the optical response of metallic inclusions in a semiconductor alloy/compound as this offers applications where a combined visible and IR-response is needed.

The above described characterization techniques will enable local device analysis and allow for defect engineering in inhomogeneous materials such as $\text{In}_x\text{Ga}_{1-x}\text{N}$. The remaining uncertainties such as 2D limitations, insufficient local resolution and measurement noise will be largely improved once the new TEAM instrument becomes available for public usage. The development of electron tomography with the ultimate goal to image in 3D a defect in atomic resolution will further specific device characterization and enhance novel material development such as InN-type composites.

In first GaN epitaxy on CVD diamond the decrease of yellow luminescence (YL) is reported. The analysis of this heterostructure may shed light on the leakage current mechanisms in GaN based devices which obviously are correlated to the materials YL. If a (thin) carbon diffusion barrier layer can be developed GaN deposition on CVD diamond may become a feasible alternative for thermally stable GaN based device technology.

8. Personnel

Eicke.R. Weber, P.I.

Petra Specht, associate research engineer
 Til Bartel, visiting scholar, Germany
 Johnny Ho, graduate student
 Swanee Shin, graduate student
 William Hong, graduate student
 Xiaoyu Xu, graduate student
 Qing Yang, graduate student
 Susie Tzeng, graduate student

MBE, TEM/STEM, coordination
 HR-TEM
 MBE of (In,Al,Ga)N, plasma analysis
 electrical/structural material characterization
 optical material characterization (Ph.D. '07)
 TEM (Ph.D. '05)
 Material characterization, TEM (Ph.D. '05)
 Device processing (Ph.D. '05)

Collaborating Researchers:

Dr. Andre Anders, LBNL	Nitrogen plasma analysis
Dr. Christian Kisielowski, LBNL, NCEM	Transmission Electron Microscopy

Dr. Rolf Erni, U. of Antwerp, Belgium	Theory of VEELS
T. Shubina, IOFFE inst. St. Petersburg, Russia	supply of InN
W. Schaff, Cornell U., USA	supply of $\text{In}_x\text{Ga}_{1-x}\text{N}$
Dr. Jerry W. Zimmer, sp3 Inc.	GaN on diamond
Dr. Daniel Francis, Group4Labs	GaN on diamond
Prof. Oscar Dubon, UC Berkeley	Material characterization since 7.06

9. References

- [Ade00] C. Adelmann, J. Simon, G. Feuillet, N. T. Pelekanos, B. Daudin, and G. Fishman, *Self-assembled InGaN quantum dots grown by molecular-beam epitaxy*, Applied Physics Letters **76** (12), 1570 (2000).
- [Ale06] M. Alevli, G. Durkaya, A. Weerasekara, A. Perera, N. Dietz, W. Fenwick, V. Woods, and I. Ferguson, *Characterization of InN layers grown by high pressure chemical vapor deposition*, Applied Physics Letters **89** (11), 112119 (2006).
- [Amb98] O. Ambacher, *Growth and applications of Group III-nitrides*, Journal of Physics D: Applied Physics **31** (20), 2653 (1998).
- [Arm05] R. Armitage, Q. Yang, E.R. Weber, J. Appl. Phys. **97**, 073524 (2005)
- [Ars03] I. Arslan, S. Ogut, P.D. Nellist, N.D. Browning, Micron **34**, 255 (2003)
- [Bak96] H. Bakker, A. Bleeker, and P. Mul, *Design and performance of an ultra-high resolution 300 kV microscope*, Ultramicroscopy **64**, 17 (1996).
- [Bar98] A. Barna, B. Pecz, and M. Menyhard, *Amorphisation and surface morphology development at low-energy ion milling*, Ultramicroscopy **70** (3), 161 (1998).
- [Bar04] T. Bartel, M. Dworzak, M. Strassburg, A. Hoffmann, A. Strittmatter, D. Bimberg, *Recombination dynamics of localized excitons in InGaN quantum dots*, Applied Physics Letters **85** (11), 1946 (2004).
- [Bar06] T. Bartel, J. Jinschek, B. Freitag, P. Specht, and C. Kisielowski, *Quantitative electron microscopy of InN-GaN alloys*, Physica Status Solidi (a) **203** (1), 167 (2006).
- [Bau92] F. Baumann, M. Bode, Y. Kim, and A. Ourmazd, *Quantitative chemical mapping: Spatial resolution*, Ultramicroscopy **47** (1-3), 167 (1992).
- [Beh99] M. Behbehani, E. Piner, S. Liu, N. El-Masry, and S. Bedair, *Phase separation and ordering coexisting in $\text{In}_x\text{Ga}_{1-x}\text{N}$ grown by metal organic chemical vapor deposition*, Applied Physics Letters **75** (15), 2202 (1999).
- [Ben04] G. Benner, E. Esser, M. Matijejevic, A. Orchowski, P. Schlossmacher, A. Thesen, M. Haider, P. Hartel, Microsc. Microanal. **10**, 108 (2004)

- [Bol95] J. P. R. Bolton, and M. Chen,
J. Phys.: Condens. Matter **7**, 3373 (1995)
- [Boo98] C. Boothroyd,
Why don't high-resolution simulations and images match?
Journal of Microscopy **190**, 99 (1998).
- [Bri03] H.A. Brink, M.M.G. Barfels, R.P. Burgner, B.N. Edwards,
Ultramicroscopy **96**, 367 (2003)
- [Bro02] G. Brockt and H. Lakner,
Micron **31**, 435 (2002)
- [But05] K. Butcher and T. Tansley,
InN, latest development and a review of the band-gap controversy,
Superlattices and Microstructures **38** (1), 1 (2005).
- [Cah58] J. Cahn and J. Hilliard,
Free Energy of a Nonuniform System. I. Interfacial Free Energy,
The Journal of Chemical Physics **28** (2), 258 (1958).
- [Chr94] S. Christiansen, M. Albrecht, H. Strunk, and H. Maier,
Strained state of Ge(Si) islands on Si: Finite element calculations and comparison to convergent beam electron-diffraction measurements,
Applied Physics Letters **64** (26), 3617 (1994).
- [Chu01] C.-C. Chuo, C.-M. Lee, and J.-I. Chyi,
Interdiffusion of In and Ga in InGaN/GaN multiple quantum wells,
Applied Physics Letters **78** (3), 314 (2001).
- [Cim06] V. Cimalla, V. Lebedev, F. M. Morales, M. Niebelschütz, G. Ecke, R. Goldhahn, and O. Ambacher,
Mat.-wiss. u. Werkstofftech. **37**, 924 (2006)
- [Coe92] W. Coene, G. Janssen, M. Op de Beeck, and D. Van Dyck,
Phase retrieval through focus variation for ultra-resolution in field-emission transmission electron microscopy,
Physical Review Letters **69** (26), 3743 (1992).
- [Coe96] W. Coene, A. Thust, M. Op de Beeck, and D. Van Dyck,
Maximum-likelihood method for focus-variation image reconstruction in high resolution transmission electron microscopy,
Ultramicroscopy **64**, 109 (1996).
- [Cre66] A. Crewe,
Scanning electron microscopes: is high resolution possible?
Science **154**, 729 (1966).
- [Cre70] A. Crewe, J. Wall, and L. Langmore,
Visibility of single atoms,
Science **168**, 1338 (1970).
- [Dam99] B. Damilano, N. Grandjean, S. Dalmaso, and J. Massies,
Room-temperature blue-green emission from InGaN/GaN quantum dots made by strain-induced islanding growth,
Applied Physics Letters **75** (24), 3751 (1999).

- [Dar97] I. Daruka and A.-L. Barabasi,
Dislocation-Free Island Formation in Heteroepitaxial Growth: A Study at Equilibrium,
Phys. Rev. Lett **79**, 3708 (1997).
- [Dav02a] Y. Davydov, A. Klochikhin, Y. Seisyan, V. Emtsev, L. Ivanov, F. Bechstedt, J. Furthmüller, H. Harima, A. Mudryi, J. Aderhold, T. Semchinova, and J. Graul,
Absorption and Emission of hexagonal InN. Evidence of narrow fundamental Band Gap,
Physica Status Solidi B **229** (3), R1 (2002).
- [Dav02b] Y. Davydov, A. Klochikhin, V. Emtsev, D. Kurdyukov, S. Ivanov, V. Vekshin, F. Bechstedt, J. Furthmüller, J. Aderhold, J. Graul, A. Mudryi, H. Harima, A. Hashimoto, A. Yamamoto, E. Haller,
Band Gap of Hexagonal InN and InGaN Alloys,
Physica Status Solidi (b) **234** (3), 787 (2002).
- [DC97] L. De Caro, A. Giuffrida, E. Carlino, and L. Tapfer,
Effects of the Elastic Stress Relaxation on the HRTEM Image Contrast of Strained Heterostructures,
Acta Crystallographica Section A **53** (2), 168 (1997).
- [Dev90] B. Deveaud, B. Guenais, A. Poudoulec, A. Regreny, and C. d'Anterrosches,
Comment on "Chemical mapping of semiconductor interfaces at near-atomic resolution",
Physical Review Letters **65** (18), 2317 (1990).
- [Ern05] R. Erni, and N. D. Browning,
Ultramicroscopy **104**, 176 (2005)
- [Ern07] R. Erni, and N. D. Browning,
Ultramicroscopy (2007), doi:10.1016/j.ultramic.2007.03.005
- [Fel07] J. Felbinger,
Fabrication and Characterization of GaN on Diamond HEMTs,
WOCSEMMAD, Feb 18-22, 2007, Savannah, GA
- [Fol86] C. P. Foley, and T. L. Tansley,
Phys. Rev. B **33**, 1430 (1986)
- [Gal07] M. Galtrey, R. Oliver, M. Kappers, C. Humphreys, D. Stokes, P. Clifton, A. Cerezo,
Three-dimensional atom probe studies of an $\text{In}_x\text{Ga}_{1-x}\text{N}/\text{GaN}$ multiple quantum well structure: Assessment of possible indium clustering,
Applied Physics Letters **90** (6), 061903 (2007).
- [Gib84] J. Gibson and M. Treacy,
The effect of elastic relaxation on the local structure of lattice-modulated thin films,
Ultramicroscopy **14** (4), 345 (1984).
- [Gib85] J. Gibson, R. Hull, J. Bean, and M. Treacy,
Elastic relaxation in transmission electron microscopy of strained-layer superlattices,
Applied Physics Letters **46** (7), 649 (1985).
- [Gol06] R. Goldhahn, P. Schley, A. T. Winzer, M. Rakel, C. Cobet, N. Esser, H. Lu, and W. J. Schaff,
J. Cryst. Growth **288**, 273 (2006)
- [Gol63] A. Golovashkin, I. Levchenko, G. Motulevich, A. Shubin,
Zh. Eksp. Teor. Fis. **51** (1963).
- [Goo74] P. Goodman and A. Moodie,
Numerical evaluation of N-beam wave functions in electron scattering by the multislice

- method*,
Acta Cryst. A **33**, 740 (1974).
- [Hai95] M. Haider, G. Braunshausen, and E. Schwan,
Correction of the spherical aberration of a 200 kV TEM by means of a hexapole-corrector,
Optik **99**, 167 (1995).
- [Har66] W. Harrison,
Parallel-Band Effects in Interband Optical Absorption,
Physical Review **147** (2), 467 (1966).
- [Har01] V.S. Harutyunyan, A.P. Arivazyan, E.R. Weber, Y. Kim, Y. Park, S.G. Subramanya,
J. of Physics **D34**, A35 (2001)
- [Ho96] I. Ho and G. Stringfellow,
Solid phase immiscibility in GaInN,
Applied Physics Letters **69** (18), 2701 (1996).
- [How04] A. Howie,
Hunting the Stobbs factor,
Ultramicroscopy **98**, 73 (2004).
- [Hu04] C. Hu, W.J. Schaff, L.F. Eastman, S.-J. Park,
IEEE Elec.Dev.Lett. **25**, 61 (2004)
- [Hum07] C. Humphreys,
Does In form In-rich clusters in InGaN quantum wells?
Philosophical Magazine **87** (13), 1971 (2007).
- [Hyd96] J. Hyde, A. Sutton, J. Harris, A. Cerezo, A. Gardiner,
Modeling spinodal decomposition at the atomic scale: beyond the Cahn - Hilliard model,
Modeling and Simulation in Materials Science and Engineering **4** (1), 33 (1996).
- [Hyt94] M. Hytch and W. Stobbs,
Quantitative comparison of high resolution TEM images with image simulations,
Ultramicroscopy **53** (3), 191 (1994).
- [Hyt98] M. Hytch, E. Snoeck, and R. Kilaas,
Quantitative measurement of displacement and strain fields from HREM micrographs,
Ultramicroscopy **74** (3), 131 (1998).
- [Hyt01] M. Hytch and T. Plamann,
Imaging conditions for reliable measurement of displacement and strain in high-resolution electron microscopy,
Ultramicroscopy **87** (4), 199 (2001).
- [Ili06] E. Iliopoulos, A. Georgakilas, A. Dimakis, E. Adikimenakis, K. Tsagaraki, M. Androulidaki, and N. Pelekanos,
InGaN(0001) alloys grown in the entire composition range by plasma assisted molecular beam epitaxy,
Physica Status Solidi (a) **203** (1), 102 (2006).
- [Iva04] S. Ivanov, T. Shubina, V. Jmerik, V. Vekshin, P. Kop'ev, and B. Monemar,
Plasma-assisted MBE growth and characterization of InN on sapphire,
Journal of Crystal Growth **269** (1), 1 (2004).

- [Iwa06] Y. Iwahashi, H. Yaguchi, A. Nishimoto, M. Orihara, Y. Hijikata, and S. Yoshida,
RF-MBE growth of cubic InN films on MgO (001) substrates,
Physica Status Solidi (c) **3** (6) (2006).
- [Jes95] D. Jesson and S. Pennycook,
Incoherent imaging of crystals using thermally scattered electrons,
Proceedings of the Royal Society of London A **449** (1936), 273 (1995).
- [Jin04] J.R. Jinschek, H.A. Calderon, K.J. Batenburg, V. Radmilovic, and C. Kisielowski,
Discrete tomography of Ga and InGa particles from HREM image simulation and exit wave reconstruction,
in *MRS Proc. Symp.*, **839** pp. 4.5.1-4.5.6 (2004).
- [Jin05] J.R. Jinschek, R. Erni, N.F. Gardner, A.Y. Kim, C. Kisielowski,
Local indium segregation and band gap variations in high efficiency green light emitting InGaN/GaN diodes,
solid state comm. **137**, 230 (2005)
- [Jin06] J.R. Jinschek and C. Kisielowski,
Time, energy, and spatially resolved TEM investigations of defects in InGaN,
Physica B: Condensed Matter **376-377**, 536 (2006).
- [Kar98] S.Y. Karpov,
Suppression of phase separation in InGaN due to elastic strain,
MRS Internet J. Nitride Semicond., vol. **3**, p. 16, (1998).
- [Kueb06] C. Kuebel and A. Thust,
TrueImage: A Software Package for Focal-Series Reconstruction in HRTEM, in *Electron Crystallography: Novel Approaches for Structure Determination of Nanosized Materials*,
NATO Science Series II: Mathematics, Physics and Chemistry, pp. 373-392 (2006).
- [Kea02] V. Keast, A. Scott, M. Kappers, C. Foxon, and C. Humphreys,
Electronic structure of GaN and $\text{In}_x\text{Ga}_{1-x}\text{N}$ measured with electron energy-loss spectroscopy,
Physical Review B **66** (12), 125319 (2002).
- [Ken01] R. Kenzler, F. Eurich, P. Maass, B. Rinn, J. Schropp, E. Bohl, and W. Diesterich,
Phase separation in confined geometries: Solving the Cahn-Hilliard equation with generic boundary conditions,
Computer Physics Communications **133** (2-3), 139 (2001).
- [Kil98] R. Kilaas,
Optimal and near-optimal Filters in high-resolution electron microscopy,
Journal of Microscopy **190**, 45 (1998)
- [Kil07] R. Kilaas, MacTempas (2007). [<http://www.totalresolution.com>]
- [Kir84] E. Kirkland,
Ultramicroscopy **15**, 151 (1984).
- [Kir98] E. Kirkland,
Advanced computing in electron microscopy, Plenum, New York (1998).
- [Kis95] C. Kisielowski, P. Schwander, F. Baumann, M. Seibt, Y. Kim, A. Ourmazd,
An approach to quantitative high-resolution transmission electron microscopy of crystalline materials,
Ultramicroscopy **58** (2), 131 (1995).

- [Kis97] C. Kisielowski, Z. Liliental-Weber, S. Nakamura,
Jpn. J. Appl. Phys. **36**, 6932 (1997).
- [Kis98a] C. Kisielowski,
Composition and Strain Fluctuations in InN/GaN/AlN Heterostructures: A Microscopic Glimpse below Surfaces,
in: 2nd International Symposium of blue Laser and Light Emitting Diodes, p. 321,
Ohmsha Ltd. (1998).
- [Kis98b] C. Kisielowski and O. Schmidt,
Microscopy and Microanalysis **4** (2), 614 (1998).
- [Kis01] C. Kisielowski, C. Hetherington, Y. Wang, R. Kilaas, M. O'Keefe, A. Thust,
Imaging columns of the light elements carbon, nitrogen and oxygen with sub Angstrom resolution,
Ultramicroscopy **89** (4), 243 (2001).
- [Kis07a] C. Kisielowski and T. Bartel,
Comment on "Three dimensional atom probe studies of an $\text{In}_x\text{Ga}_{1-x}\text{N}/\text{GaN}$ multiple quantum well structure: Assessment of possible indium clustering" by M.J. Galtrey et al.,
Applied Physics Letters, submitted (2007).
- [Kis07b] C. Kisielowski, T. Bartel, P. Specht, F.-R. Chen, T. Shubina,
From extended defects and interfaces to point defects in three dimensions,
Physica B: Condensed Matter **401**, 639 (2007).
- [Kis08] C. Kisielowski,
to be published, Ultramicroscopy (2008).
- [Kre01] S. Kret, P. Ruterana, A. Rosenauer, D. Gerthsen,
Extracting Quantitative Information from High Resolution Electron Microscopy,
Physica Status Solidi (b) **227** (1), 247 (2001).
- [Kre02] I. L. Krestnikov, N. N. Ledentsov, A. Ho_mann, D. Bimberg, A. V. Sakharov, W. V. Lundin, A. F. Tsatsul'nikov, A. S. Usikov, Z. I. Alferov, Y. G. Musikhin, D. Gerthsen,
Quantum dot origin of luminescence in InGaN-GaN structures,
Phys. Rev. B **66**, 155310 (2002).
- [Krö68] E. Kröger,
Z. Physik **216**, 115 (1968)
- [Laz03] S. Lazar, G.A. Botton, M.-Y. Wu, F.D. Tichelaar, H.W. Zandbergen,
Ultramicroscopy **96**, 535 (2003)
- [Laz06] S. Lazar, G. A. Botton, and H. W. Zandbergen,
Ultramicroscopy **106**, 1091 (2006)
- [Li05a] S. Li,
Growth and Characterization of cubic InGaN and InGaN/GaN quantum wells,
PhD Thesis, Universitaet Paderborn (2005).
- [Li05b] T. Li, E. Hahn, D. Gerthsen, A. Rosenauer, A. Strittmatter, L. Reissmann, D. Bimberg,
Indium redistribution in an InGaN quantum well induced by electron-beam irradiation in a transmission electron microscope,
Applied Physics Letters **86** (24), 241911 (2005).
- [Lu00] H. Lu, W. Scha_, J. Hwang, H. Wu, W. Yeo, A. Pharkya, L. Eastman,
Improvement on epitaxial growth of InN by migration enhanced epitaxy,
Applied Physics Letters **77** (16), 2548 (2000).

- [Lu03] H. Lu, W. J. Schaff, L. F. Eastman, and C. E. Stutz,
Appl. Phys. Lett. **82**, 1736 (2003)
- [LW05] Z. Liliental-Weber, D. Zakharov, K. Yu, J. Ager, W. Walukiewicz, E. Haller, H. Lu, W. Schaff,
Compositional modulation in $\text{In}_x\text{Ga}_{1-x}\text{N}$: TEM and X-ray studies,
Journal of Electron Microscopy **54** (3), 243 (2005).
- [McN93] L. McNeil, M. Grimsditch, R. French,
Vibrational Spectroscopy of Aluminum Nitride,
J. Am. Ceram. Soc. **76** (5), 1132 (1993).
- [Mkh03] K. Mkhoyan and J. Silcox,
Electron-beam-induced damage in wurtzite InN ,
Applied Physics Letters **82** (6), 859 (2003).
- [Mon05] B. Monemar, P.P. Paskov, A. Kasic,
Superlatt. and Microstruct. **38**, 38 (2005)
- [Nak95] S. Nakamura,
J. Vac. Sci. Technol. **A13**, 705 (1995)
- [Nao06] H. Naoi, M. Kurouchi, D. Muto, S. Takado, T. Araki, T. Miyajima, H. Na, Y. Nanishi,
Growth and properties of InN , InGaN , and InN/InGaN quantum wells,
Physica Status Solidi (a) **203** (1), 93 (2006).
- [OdB96a] M. Op de Beeck and D. Van Dyck,
Direct structure reconstruction in HRTEM,
Ultramicroscopy **64** (1-4), 153 (1996).
- [OdB96b] M. Op de Beeck, D. Van Dyck, W. Coene,
Wave function reconstruction in HRTEM: the parabola method,
Ultramicroscopy **64** (1-4), 167 (1996).
- [ODo01] K.P. O'Donnell, J.F.W. Mosselmans, R.W. Martin, S. Pereira, M.E. White,
J. Phys: Condens. Matter **13**, 6977 (2001)
- [O'K78] M. O'Keefe, P. Buseck, S. Lijima,
Computed crystal structure images for high resolution electron microscopy,
Nature **274**, 322 (1978).
- [O'K01] M. O'Keefe, C. Hetherington, Y. Wang, E. Nelson, J. Turner, C. Kisielowski, J. Malm,
R. Mueller, J. Ringnald, M. Pan, and A. Thust,
Sub-Angstrom high resolution transmission electron microscopy at 300 keV,
Ultramicroscopy **89** (4), 215 (2001).
- [Okt99] S. Oktyabrsky, K. Dovidenko, A. Sharma, J. Narayan, V. Joshkin,
Cubic GaN formation under nitrogen-deficient conditions,
Applied Physics Letters **74** (17), 2465 (1999).
- [O'N03] J. O'Neill, I. Ross, A. Cullis, T. Wang, P. Parbrook,
Electron-beam-induced segregation in InGaN/GaN multiple-quantum wells (erratum),
Applied Physics Letters **83** (10), 1965 (2003).
- [Osa75] K. Osamura, S. Naka, Y. Murakami,
J. Appl. Phys. **46**, 3432 (1975)
- [Osh01] Y. Oshima, T. Nangou, H. Hirayama, K. Takayanagi,
Face centered cubic indium nano-particles studied by UHV-transmission electron

- microscopy*,
Surface Science **476** (1-2), 107 (2001).
- [Our89a] A. Ourmazd, D. Taylor, M. Bode, Y. Kim,
Quantifying the Information Content of Lattice Images,
Science **246** (4937), 1571 (1989).
- [Our89b] A. Ourmazd, D. Taylor, J. Cunningham, C. Tu,
Chemical Mapping of Semiconductor Interfaces at Near-Atomic Resolution,
Physical Review Letters **62** (8), 933 (1989).
- [Our90] A. Ourmazd, F. Baumann, M. Bode, Y. Kim,
Quantitative chemical lattice imaging: theory and practice,
Ultramicroscopy **34** (4), 237 (1990).
- [Per98] P. Perlin, C. Kisielowski, V. Iota, B. Weinstein, L. Mattos, N. Shapiro, J. Kruger,
E.R. Weber, J. Yang,
*InGaN/GaN quantum wells studied by high pressure, variable temperature, and
excitation power spectroscopy*,
Applied Physics Letters **73** (19), 2778 (1998).
- [Per07] A. Perronet, Mefisto Finite Element Analysis program package (2007).
[http://www.ann.jussieu.fr/perronet/me_stoa.gene.html]
- [Pic78] I. Pichugin and M. Tiachala,
Izv. Akad. Nauk SSSR, Neorg. Mater. **14** (1978).
- [Pol96] A. Polian, M. Grimsditch, I. Grzegory,
Elastic constants of gallium nitride,
Journal of Applied Physics **79** (6), 3343 (1996).
- [Raf98] B. Rafferty and L.M. Brown,
Phys. Rev. B **58**, 10326 (1998)
- [Rao04] M. Rao, D. Kim, and S. Mahajan,
Compositional dependence of phase separation in InGaN layers,
Applied Physics Letters **85** (11), 1961 (2004).
- [Rol02] H. Roll, O. Breitschadel, J. Off, B. Khun, F. Scholz, H. Schweizer,
Sec. Jointed Symposium on *Opto- and Microelectronic Devices and Circuits*, p. 236
(2002)
- [Ros98] A. Rosenauer, U. Fischer, D. Gerthsen, A. Forster,
Composition evaluation by lattice fringe analysis,
Ultramicroscopy **72** (3-4), 121 (1998).
- [Ros05] M. Rosker,
CS MANTECH 2005, paper 1.2
- [Ros06] A. Rosenauer, D. Gerthsen, V. Potin,
Strain state analysis of InGaN/GaN - sources of error and optimized imaging conditions,
Physica Status Solidi (b) **203** (1), 176 (2006).
- [Rut98] P. Ruterana, G. Nouet, W. Van der Stricht, I. Moerman, L. Considine,
*Chemical ordering in wurtzite $\text{In}_x\text{Ga}_{1-x}\text{N}$ layers grown on (0001) sapphire by
metalorganic vapor phase epitaxy*,
Applied Physics Letters **72** (14), 1742 (1998).
- [Rut02] P. Ruterana, S. Kret, A. Vivet, G. Maciejewski, P. Dluzewski,
Composition fluctuation in InGaN quantum wells made from molecular beam or

- metalorganic vapor phase epitaxial layers*,
Journal of Applied Physics **91** (11), 8979 (2002).
- [Rya02] P. Ryan, C. Mc Guinness, J.E. Downes, K.E. Smith,
Phys. Rev. B **65**, 205201 (2002)
- [Seg04] R. Seguin, S. Rodt, A. Strittmatter, L. Reissmann, T. Bartel, A. Hoffmann, D. Bimberg,
E. Hahn, D. Gerthsen,
Multi-excitonic complexes in single InGaN quantum dots,
Applied Physics Letters **84** (20), 4023 (2004).
- [Sel83] P. Self, M. O'Keefe, P. Buseck, and A. Spargo,
Practical computation of amplitudes and phases in electron diffraction,
Ultramicroscopy **11**, 35 (1983).
- [She76] A. Sheleg and S. V.A.,
Vesti Akad. Nauk BSSR, Ser. Fiz. Mater. Nauk **3**, 126 (1976).
- [Shr05] S. Shrestha, H. Timmers, K. Butcher, M. Wintrebert-Fouquet, P. Chen,
Nitrogen depletion of indium nitride films during Elastic Recoil Detection analysis,
Nuclear Instruments and Methods in Physics Research Section B: Beam Interactions with
Materials and Atoms **234** (3), 291 (2005).
- [Shu97] M. Shur and M. Khan,
MRS. Bull. **22** (2) (1997).
- [Shu04a] T. Shubina, S. Ivanov, V. Jmerik, P. Kop'ev, A. Vasson, J. Leymarie, A. Kavokin, H.
Amano, B. Gil, O. Briot, B. Monemar,
Shubina et al. Reply,
Physical Review Letters **93** (26), 269702 (2004).
- [Shu04b] T. Shubina, S. Ivanov, V. Jmerik, D. Solnyshkov, V. Vekshin, P. Kop'ev, A. Vasson, J.
Leymarie, A. Kavokin, H. Amano, K. Shimono, A. Kasic, B. Monemar,
Mie Resonances, Infrared Emission, and the Band Gap of InN ,
Physical Review Letters **92** (11), 117407 (2004).
- [Shu06] T. Shubina, D. Plotnikov, A. Vasson, J. Leymarie, M. Larsson, P. Holtz, B. Monemar, H.
Lu, W. Schaff, and P. Kop'ev,
Surface-plasmon resonances in indium nitride with metal-enriched nano-particles,
Journal of Crystal Growth **288** (2), 230 (2006).
- [Shu07] A. Shubina, Private communication (2007).
- [Sme03] T. Smeeton, M. Kappers, J. Barnard, M. Vickers, C. Humphreys,
*Electron beam-induced strain within InGaN quantum wells: False indium "cluster"
detection in the transmission electron microscope*,
Applied Physics Letters **83** (26), 5419 (2003).
- [Sme06] T. Smeeton, C. Humphreys, J. Barnard, M. Kappers,
*The impact of electron beam damage on the detection of indium-rich localisation centres
in InGaN quantum wells using transmission electron microscopy*,
Journal of Materials Science **41** (9), 2729 (2006).
- [Spe99] P. Specht, R.C. Lutz, R. Zhao, E.R. Weber, W.K. Liu, K. Bacher, F.J. Towner, T.R.
Stewart, M. Luysberg,
J. Vac. Sci. Technol. **B17**, 1200 (1999)
- [Spe02] P. Specht, R. Zhao, J. Gebauer, E.R. Weber,
A Standard Low Temperature GaAs Growth - Prerequisite for Defect Engineering,

- Proc. of the 4th Symposium on Non-Stoichiometric III-V Compounds, Asilomar, USA, Oct. 2002, eds.: P. Specht et al., Physik Mikrostrukturierter Halbleiter vol. **27**, (2002), 31
- [Spe04] P. Specht, R. Armitage, J. Ho, E. Gunawan, Q. Yang, X. Xu, C. Kieselowski, E.R. Weber,
J. Crystal Growth **269**, 111 (2004)
- [Spe05] P. Specht, J. Ho, X. Xu, R. Armitage, E. Weber, R. Erni, C. Kieselowski,
Band transitions in wurtzite GaN and InN determined by valence electron energy loss spectroscopy,
Solid State Communications **135** (5), 340 (2005).
- [Spe06] P. Specht, X. Xu, R. Armitage, E. R. Weber, R. Erni, C. Kieselowski,
Physica B **376-377**, 522 (2006)
- [Sta98] C. Stamp and C. Van de Walle,
Energetics and electronic structure of stacking faults in AlN, GaN, and InN,
Physical Review B **57** (24), R15052 (1998),
- [TEA] [<http://ncem.lbl.gov/TEAM-project/>]
- [Tel03] L. Teles, L. Ferreira, J. Leite, L. Scolfaro, A. Kharchenko, O. Husberg, D. As, D. Schikora, K. Lischka,
Strain-induced ordering in $\text{In}_x\text{Ga}_{1-x}\text{N}$ alloys,
Applied Physics Letters **82** (24), 4274 (2003).
- [Ter99] M. Terauchi, M. Tanaka, K. Tsuno, M. Ishida,
J. Microsc. **194**, 203 (1999)
- [Tie99] P.C. Tiemeijer,
Inst. Phys. Conf. Ser. **161**, 191 (1999)
- [Til00] K. Tillmann, M. Lentzen, R. Rosenfeld,
Impact of column bending in high-resolution transmission electron microscopy on the strain evaluation of GaAs/InAs/GaAs heterostructures,
Ultramicroscopy **83** (1-2), 111 (2000).
- [Tre86] M. Treacy and J. Gibson,
The effects of elastic relaxation on transmission electron microscopy studies of thinned composition-modulated materials,
Journal of Vacuum Science and Technology B: Microelectronics and Nanometer Structures **4** (6), 1458 (1986).
- [Uen94] M. Ueno, M. Yoshida, A. Onodera, O. Shimomura, K. Takemura,
Stability of the wurtzite-type structure under high pressure: GaN and InN,
Physical Review B **49** (1), 14 (1994).
- [Vil91] P. Villars and L. Calvert,
Pearson's Handbook of Crystallographic Data for Intermetallic Phases,
ASM International, 2nd edition (1991).
- [Vur03] I. Vurgaftman, J.R. Meyer,
J. Appl. Phys. **94**, 3675 (2003)
- [Wes01] A. Westmeyer and S. Mahajan,
Periodic composition modulations in InGaN epitaxial layers,
Applied Physics Letters **79** (17), 2710 (2001).
- [Woo06] V. Woods and N. Dietz,
InN growth by high-pressures chemical vapor deposition: Real-time optical growth

- characterization*,
Materials Science and Engineering: B **127** (2-3), 239 (2006).
- [Wri97a] A. Wright,
Basal-plane stacking faults and polymorphism in AlN, GaN, and InN,
J. Appl. Phys. **82** (10), 5259 (1997).
- [Wri97b] A. Wright,
Elastic properties of zinc-blende and wurtzite AlN, GaN, and InN,
Journal of Applied Physics **82** (6), 2833 (1997).
- [Wu02a] J. Wu, W. Walukiewicz, K. Yu, J. Ager III, E. Haller, H. Lu, W. Scha_, Y. Saito, Y. Nanishi,
Unusual properties of the fundamental band gap of InN,
Applied Physics Letters **80** (21), 3967 (2002).
- [Wu02b] J. Wu, W. Walukiewicz, K. M. Yu, J. W. A. III, E. E. Haller, H. Lu, W. J. Schaff, Y. Saito, Y. Nanishi,
Unusual properties of the fundamental band gap of InN,
Applied Physics Letters **80**, 3967 (2002).
- [Wu04] J. Wu, W. Walukiewicz, S.X. Li, R. Armitage, J.C. Ho, E.R. Weber, E.E. Haller, H. Lu, W.J. Schaff, R. Barcz, R. Jakiela,
Appl. Phys. Lett. **84**, 2805 (2004)
- [Xu05] X. Xu, P. Specht, R. Armitage, J. Ho, E. Weber, C. Kisielowski,
Characterization of oxide precipitates in epitaxial InN by transmission electron microscopy,
Applied Physics Letters **87** (9), 092102 (2005).
- [Yeh92] C.-Y. Yeh, Z. Lu, S. Froyen, A. Zunger,
Zinc-blende and wurtzite polytypism in semiconductors,
Physical Review B **46** (16), 10086 (1992).
- [Yua88] J. Yuan, L. M. Brown, and W. Y. Liang,
J. Phys. C. **21**, 517 (1988)
- [Zhe94] J. Zheng, J. Walker, M. Salmeron, and E. Weber,
Interface Segregation and Clustering in Strained-Layer InGaAs/GaAs Heterostructures Studied by Cross-Sectional Scanning Tunneling Microscopy,
Physical Review Letters **73** (2), 368 (1994).

10. Publications

1. *The Influence of Structural Properties on Conductivity and Luminescence of MBE grown InN*,
P. Specht, R. Armitage, J.C. Ho, E. Gunawan, Q. Yang, X. Xu, C. Kisielowski, E.R. Weber,
J. of Crystal Growth **269**, 111 (2004)
2. *Anisotropy of the Elastic Properties of Wurtzite InN Epitaxial Films*,
V.S. Harutyunyan, P. Specht, J. Ho, E.R. Weber,
Defect and Diffusion Forum **226-228**, 79 (2004)
3. *Analysis of the Carbon-related “blue” Luminescence in GaN*,
R. Armitage, Q. Yang, E.R. Weber,
J. Appl. Phys. **97**, 73524 (2005)

4. *Epitaxial Condition and Polarity in GaN grown on a HfN-buffered Si(111) Wafer*,
X. Xu, R. Armitage, S. Shinkai, K. Sasaki, C. Kisielowski, E.R. Weber,
Appl. Phys. Lett. **86**, 182104 (2005)
5. *Characterization of Oxide Precipitates in Epitaxial InN by Transmission Electron Microscopy*,
X. Xu, P. Specht, R. Armitage, J.C. Ho, E.R. Weber, C. Kisielowski,
Appl. Phys. Lett. **87**, 092102 (2005)
6. *Band Transitions in Wurtzite GaN and InN Determined by Valence Electron Energy Loss Spectroscopy*,
P. Specht, J. Ho, X. Xu, R. Armitage, E.R. Weber, R. Erni, C. Kisielowski,
Solid State Comm. **135**, 340 (2005)
7. *Distortion and Segregation in a Dislocation Core Region at Atomic Resolution*,
X. Xu, S.P. Beckman, P. Specht, E.R. Weber, D.C. Chrzan, C. Kisielowski,
Phys. Rev. Lett. **95**, 145501 (2005)
8. *Effects of Stoichiometry on Electrical, Optical and structural Properties of Indium-Nitride*,
J.C. Ho, P. Specht, Q. Yang, X. Xu, D. Hao, E.R. Weber,
J. of Appl. Phys. **98**, 093712 (2005)
9. *Quantitative electron microscopy of InN – GaN alloys*,
T. Bartel, J.R. Jinschek, B. Freitag, P. Specht, C. Kisielowski,
phys. stat. sol. (a) **203**, 167 (2006) - editor's choice, titlepage
10. *Zincblende and wurtzite phases in InN epilayers and their respective band transitions*,
P. Specht, J.C. Ho, X. Xu, R. Armitage, E.R. Weber, R. Erni, C. Kisielowski,
J. of Crystal Growth **288**, 225 (2006)
11. *Local band and defect transitions in InGaN observed by valence electron energy loss spectroscopy*,
P. Specht, X. Xu, R. Armitage, E.R. Weber, R. Erni, C. Kisielowski,
Physica B **376-377**, 552 (2006)
12. *Atomic Scale Analysis of Planar Defects in Polycrystalline Diamond*,
R. Erni, B. Freitag, P. Hartel, H. Müller, P. Tiemeijer, M. van der Stam, M. Stekelenburg,
D. Hubert, P. Specht, V. Garibay-Febles,
Microsc. Microanal. **12**, 492 (2006)
13. "Spinodal Decomposition in Thick InGaN Layers studied by Strain Field Analysis",
T. Bartel, C. Kisielowski, P. Specht,
Microsc. Microanal. **12**, 1014 (2006)
14. *Low Temperature InN: The Effect of Spatial Resolution on Band Transition Determination*,
P. Specht,
Conference presentation, 3rd International Workshop on Nitride Semiconductors,
Ilhabela, Brazil (2006)
15. *Decomposition in InGaN*,
T.P. Bartel, P. Specht, C. Kisielowski,
Conference presentation, 3rd International Workshop on Nitride Semiconductors,
Ilhabela, Brazil (2006)

16. *Spinodal Decomposition in Thick $\text{In}_x\text{Ga}_{1-x}\text{N}$ Layers studied by Strain Field Analysis*,
T.P. Bartel, P. Specht, C. Kisielowski,
Conference presentation, Microscopy and Microanalysis, Chicago, USA (2006)
17. *Retardation, Surface and Interface effects in VEELS*,
R. Erni, N.D. Browning, P. Specht, C. Kisielowski,
Microsc. Microanal. **13**, 1250 (2007)
18. *Phase Separation in $\text{In}_x\text{Ga}_{1-x}\text{N}$* ,
T.P. Bartel, P. Specht, J.C. Ho, C. Kisielowski,
Phil. Mag. **87**, 1983 (2007)
19. *Are the materials properties of Indiumnitride dominated by Defects?*,
P. Specht, W. Hong, E.R. Weber,
MRS Symp.Proc. **994**, F02-01 (2007)
20. *High Resolution Transmission Electron Microscopy of InN*,
T.P. Bartel, C. Kisielowski, P. Specht, T.V. Shubina, V.N. Jmerik, S.V. Ivanov,
Appl. Phys. Lett. **91**, 101908 (2007)
21. *From extended defects and interfaces to point defects in three dimensions*,
C. Kisielowski, T.P. Bartel, P. Specht, F.-R. Chen, T.V. Shubina,
Physica B: Condensed Matter **401**, 639 (2007)
22. *Inclusions in InN imaged by HR-TEM*,
T.P. Bartel, P. Specht, C. Kisielowski,
International Conference on Nitride Semiconductors, Las Vegas, USA (2007)
23. *Applications, Limits and Prospects of Valence Electron Energy Loss Spectroscopy in Transmission Electron Microscopy*,
R. Erni, L. Zhang, N.D. Browning, P. Specht, C. Kisielowski,
FEMMS2007, Sept. 23-28, 2007, Rohnert Park, Sonoma, CA, USA
24. *Considerations about bandgap measurements of InN by VEELS in STEM*,
R. Erni, P. Specht, C. Kisielowski,
submitted to Solid State Comm. (2007)